

# TABLE OF CONTENTS

<u>Section</u>	<u>Page</u>	
SUMMARY . . . . .	1	1/A13
INTRODUCTION. . . . .	3	1/B1
POTENTIAL FLOW THEORY . . . . .	5	1/B3
Laplace Equation . . . . .	5	1/B3
Singular Solutions . . . . .	8	1/B6
Boundary Conditions. . . . .	13	1/B11
Wakes. . . . .	22	1/C6
RESEARCH ON GREEN'S IDENTITY FORMULATION. . . . .	26	1/C10
Comparison of Surface Paneling Methods . . . . .	27	1/C11
Internal Potential Boundary Condition Formulation. . . . .	33	1/D3
Comparison of Green's Identity Formulations. . . . .	38	1/D8
Accuracy of Concave Corner Solutions . . . . .	49	1/E5
Inverse (Design) Capability. . . . .	55	1/E11
Selected Formulation . . . . .	60	1/F2
NUMERICAL SOLUTION FORMULATION. . . . .	61	1/F3
Geometry Panel Modeling. . . . .	64	1/F6
Panel Singularity Distribution . . . . .	70	1/F12
Influence Function Formulas . . . . .	70	1/F12
Doublet Distribution Surface Fit Approaches . . . . .	74	1/G2
Boundary Conditions. . . . .	86	1/G14
Calculation of Flow Properties . . . . .	90	2/A5
CALCULATED RESULTS. . . . .	92	2/A7
CONCLUSIONS AND RECOMMENDATIONS . . . . .	110	2/B11
REFERENCES. . . . .	112	2/B13

AUG 25 1978

NAS 1.26:3020

NASA Contractor Report 3020

ORIGINAL  
COMPLETED

**Modification of the Douglas  
Neumann Program To Improve  
the Efficiency of Predicting  
Component Interference and  
High Lift Characteristics**

D. R. Bristow and G. G. Grose

CONTRACT NAS1-14756  
AUGUST 1978

**NASA**

127

830-H-14 245/1.2/13  
**NASA Contractor Report 3020**

# **Modification of the Douglas Neumann Program To Improve the Efficiency of Predicting Component Interference and High Lift Characteristics**

**D. R. Bristow and G. G. Grose**  
*McDonnell Douglas Corporation*  
*St. Louis, Missouri*

**Prepared for**  
**Langley Research Center**  
**under Contract NAS1-14756**



National Aeronautics  
and Space Administration

**Scientific and Technical  
Information Office**

**1978**

BLANK PAGE



# LIST OF ILLUSTRATIONS AND TABLES

<u>Figure</u>	<u>Title</u>	<u>Page</u>
1	Illustration of a Bounded Fluid . . . . .	6
2	Point Doublet at $(x_o, y_o, z_o)$ . . . . .	9
3	Body of Revolution Represented by an Equivalent Axial Singularity Distribution. . . . .	10
4	Body for Which no Equivalent Axial Singularity Distribution Exists . . . . .	11
5	Points in a Fluid and on a Boundary . . . . .	12
6	Equivalency Between Vortex Loops and Doublet Surfaces. . . . .	13
7	Direct and Indirect Measurements. . . . .	15
8	Two Sides of a Flow Boundary Surface. . . . .	17
9	Body Immersed in an Unbounded Flow Field. . . . .	18
10	Surface Velocity Corresponding to Green's Identity. . . . .	20
11	Equivalent Singularity Representations for a Circular Cylinder . . . . .	21
12	Circulation Around a Wing Section . . . . .	23
13	Simple Wake Model . . . . .	25
14	Singularity Distributions for Supercritical Airfoil at $4^\circ$ $\alpha$ . . . . .	30
15	Circular Cylinder Inverse Solution. . . . .	31
16	Two-Element Airfoil Inviscid Solution . . . . .	32
17	Two-Dimensional Panel Modeling. . . . .	35
18	Coordinate System for a Panel of Length $s$ . . . . .	36
19	Prediction Accuracy for a Circular Cylinder . . . . .	40
20	Karman - Trefftz Airfoil. . . . .	41
21	Karman - Trefftz Airfoil. . . . .	42
22	Supercritical Airfoil . . . . .	44
23	Noisy Flat Plate at $-90^\circ$ Incidence. . . . .	45
24	Thin Symmetrical Airfoil Geometry . . . . .	46
25	Thin Symmetrical Airfoil at Zero Incidence. . . . .	47
26	Thin Symmetrical Airfoil Vorticity at 50% Chord . . . . .	48
27	Simple Geometry with a Concave Corner . . . . .	50

# LIST OF ILLUSTRATIONS AND TABLES (Cont)

<u>Figure</u>	<u>Title</u>	<u>Page</u>
28	Calculated Velocity Distribution for Symmetric Flow. . . . .	51
29	Velocity Distribution Near a Concave Corner (Symmetric Flow). . . . .	52
30	Calculated Velocity Distribution for Anti-Symmetric Flow. . . . .	53
31	Velocity Distribution Near a Concave Corner (Anti-Symmetric Flow) . . . . .	54
32	Circular Cylinder Inverse Solution (MCAIR Method) .	58
33	Two-Element Airfoil Inverse Solution (MCAIR Method) . . . . .	59
34	A Section of a Body Surface . . . . .	65
35	Corner Point Indexing Convention for a Section. . .	66
36	Panel Indexing Convention for a Section . . . . .	66
37	Adjustment of the Input Points to Form a Plane Trapezoidal Panel . . . . .	67
38	Panel Coordinate System ( $\xi, \eta$ ) . . . . .	69
39	Broken Line Segment Approximation to Function $f(x)$ . .	75
40	Two Curve Fits to a Doublet Distribution. . . . .	76
41	Vortex Distribution . . . . .	77
42	Normal Velocity Distribution. . . . .	78
43	Schematic of Panel Control Point on a Section . . .	79
44	Indexing Convention for $\mu$ in Vicinity of Panel ( $i_p, j_p$ ) . . . . .	80
45	Panel Edge Locations for Doublet Matching . . . . .	83
46	Three Quadratic Curve Fits to a Doublet Distribution. . . . .	84
47	Vortex Distribution . . . . .	85
48	Normal Velocity Distribution. . . . .	86
49	Schematic of Wake Control Points. . . . .	88
50	Potential and Normal Velocity in Vicinity of Adjacent Panel Edges. . . . .	89
51	Supercritical Wing. . . . .	93
52	Williams Two-Element Wing Geometry. . . . .	94

# LIST OF ILLUSTRATIONS AND TABLES (Concluded)

<u>Figure</u>	<u>Title</u>	<u>Page</u>
53	Williams Two-Element Wing Pressure Distribution . .	95
54	Rectangular Wing Pressure Distribution, Root. . . .	97
55	Rectangular Wing Pressure Distribution, Midspan . .	98
56	Rectangular Wing Pressure Distribution, Tip . . . .	98
57	Sphere Paneling . . . . .	99
58	Pressure Distribution for a Sphere. . . . .	99
59	RM L51F07 Body Alone. . . . .	100
60	Duct Paneling . . . . .	101
61	Duct Internal Pressure Distribution, Exit Kutta Condition Applied . . . . .	102
62	Duct Internal Pressure Distribution, Zero Circulation . . . . .	103
63	Wing-Body Geometry. . . . .	104
64	Fuselage Pressure Distribution in Presence of Wing. . . . .	106
65	Wing-Body Chordwise Pressure Distribution- Exposed Root. . . . .	108
66	Wing-Body Chordwise Pressure Distribution- Midspan . . . . .	108
67	Wing-Body Chordwise Pressure Distribution- Tip . . . . .	109

## LIST OF TABLES

<u>Table</u>	<u>Title</u>	<u>Page</u>
I	2-D Surface Singularity Methods Tested. . . . .	28
II	Control Point Index Table . . . . .	80

# SYMBOLS

$A$	arbitrary point in a region
$A^+$	final point of contour of integration
$A^-$	initial point of contour of integration
$A_{ij}$	rate of change of surface velocity on panel $i$ with respect to surface angle change of panel $j$
$AR$	wing aspect ratio
$a_i, b_i$	constants of linear broken line segment $i$
$[a_{ij}]$	transformation matrix from body to panel coordinate system, see equation (32)
$B$	arbitrary point in a region; point on boundary surface
$B_{c_l}$	see equation (46)
$B_{l_k}$	see equations (44) and (47)
$B_{p_{lk}}$	see equation (46)
$C_L$	lift coefficient
$C_{l_l}$	section lift coefficient
$C_p$	pressure coefficient, equation (6)
$c$	reference length for airfoil section coefficients; chord
$\frac{D}{Dt}$	material derivative
$dS$	differential surface area
$dl$	differential distance along a contour of integration
$ds$	differential distance along surface
$E$	error function of doublet fit, see equation (43)
$\vec{e}_x, \vec{e}_y, \vec{e}_z$	unit vectors in body coordinate system

# SYMBOLS (Continued)

$\vec{e}_\xi, \vec{e}_\eta, \vec{e}_\zeta$	unit vectors in panel coordinate system
$H_{mn}$	influence function given by Hess, reference 2
$i$	panel number index on airfoil section; index of panel corner defining airfoil section geometry
$(i, j)$	index of panel corner in a section
$(i_p, j_p)$	index of panel number in a section
$J_{mn}$	influence function given by Hess, reference 2
$k$	index of corners of a panel ( $k = 1, 2, 3, 4$ ); index of neighboring control points used in determination of doublet distribution on a panel ( $1 \leq k \leq 9$ )
$L^{(mn)}$	influence function given by Hess, reference 2
$m$	strength of a point source
$m_{mn}$	influence function given by Hess, reference 2
$(N, M)$	total number of points $(i, j)$ defining panels in a section
$n$	total number of panels on airfoil section; distance along axis normal to the boundary surface
$\vec{n}$	doublet direction unit vector; unit vector normal to boundary surface
$P$	field point
$p$	pressure
$\vec{p}_F$	see equation (27)
$\vec{p}_k$	see equation (26)
$\vec{p}_k^*$	see equation (29)
$\vec{p}_S$	see equation (27)
$Q$	point on flow boundary

# SYMBOLS (Continued)

$R$	fluid region between boundaries
$R_1, R_2$	radii from panel edges to field point, see figure 18
$r$	radius from singularity to field point
$S$	surface distance from corner
$s$	distance along surface; separation distance of doublet point; length of a two-dimensional panel
$\vec{s}$	distance vector along a streamline path
$T_k^{(mn)}$	influence function given by Hess, reference 2
$t$	time; airfoil maximum thickness
$V$	total velocity magnitude
$\vec{V}$	velocity vector
$\vec{V}_\infty$	uniform freestream velocity vector
$V_{\infty 1}, V_{\infty 2}, V_{\infty 3}$	unit freestream velocity vectors, equation (49)
$V_N$	normal velocity component, equation (11)
$V_{N_\infty}$	normal component of $\vec{V}_\infty$
$V_T$	tangential velocity component
$V_{T_\infty}$	tangential component of $\vec{V}_\infty$
$V_x^*, V_y^*, V_z^*$	influence functions given by Hess, reference 2
$V_y^*$	
$V_z^*$	
$\Delta V_{Ti}$	change in surface tangential velocity component
$W_k$	weighting values, see equation (43)
$(x, y, z)$	coordinates of a field point, body reference axes coordinates
$(x_o, y_o, z_o)$	coordinates of a singular point; coordinates of panel centroid

# SYMBOLS (Continued)

$\alpha$	angle of attack
$\alpha_x, \alpha_y, \alpha_z$	free stream velocity components in x,y,z directions
$\alpha_1, \alpha_2$	angles from panel edges to field point, see figure 18
$\beta$	see equation (22)
$\beta_1 \dots \beta_6$	constants of doublet distribution, equal to $\mu_{00} \dots \mu_{02}$ , see equation (45)
$\Gamma$	strength of vortex loop
$\gamma$	vortex density
$\vec{\gamma}$	vortex density vector
$\epsilon$	relative error in a measurement or prediction
$\sqrt{\epsilon^2}$	root-mean-square error of calculated vortex density
$\eta$	fraction semispan
$\theta$	angle from plane of symmetry
$\theta_j$	surface angle of panel j on an airfoil
$\Lambda$	wing sweep angle
$\lambda$	wing taper ratio
$\mu$	doublet strength per unit area, doublet density
$\mu_{00} \dots \mu_{02}$	coefficients of quadratic doublet distribution on a panel, see equation (33)
$\xi, \eta, \zeta$	panel coordinate system
$\xi_0, \eta_0, \zeta_0$	coordinates of a field point in panel coordinate system
$\rho$	fluid density
$\sigma$	source strength per unit area, source density
$\sigma_j$	constant source density on a panel
$\phi$	total potential function

# SYMBOLS (Concluded)

$\phi_D$	doublet potential function
$\phi_S$	source potential function
$\phi$	perturbation potential function
$\phi_{mn}$	potential induced by doublet distribution $\mu = \xi^m \eta^n$
$\phi_{mn}^*$	influence functions, see equation (38)
$\phi_S$	potential induced by uniform source density of unit strength on a panel
$\phi_S^*$	influence function, see equation (36)

## OPERATORS

$\nabla$	gradient operator
$\nabla^2$	Laplacian operator

## SUBSCRIPTS

A,R	any two points in a field
c	control point on a panel
D	point doublet
E	point on boundary surface in real external flow field
I	point on boundary surface in imaginary internal flow field
N	component of vector normal to boundary surface
Q	point on flow boundary
S	point source
T	component of vector tangential to boundary surface
$\infty$	free stream conditions



## SUMMARY

Modifications were made to the three-dimensional Douglas Neumann surface singularity method developed by Hess in order to improve the accuracy and efficiency of calculating the low speed potential flow on arbitrary lifting configurations. The original source paneling is replaced by a combination of source and doublet panels based on the classical Green's identity. The amount of calculation per panel is not increased, as the source distribution is given directly by the body geometry. Solution to a set of equations for approximately one doublet strength parameter per panel then gives the doublet distribution to satisfy boundary conditions of flow tangency on the body. A doublet sheet represents the wake of vorticity from the trailing edge of lifting surfaces.

A numerical study of the characteristics of Green's identity was made for two-dimensional flow. The source panel method used in the original Douglas Neumann program is less accurate on thin, highly loaded lifting surfaces as the result of local source singularities of large magnitude. Results show significantly better accuracy in such cases for the milder source-doublet combination of Green's identity. A wake-tangency Kutta condition improves the accuracy of the calculated lift. This permits a reduced number of panels (20 to 40 on an airfoil section) for a given accuracy, and a substantial saving of computing cost on configurations such as high lift devices or supercritical airfoils. Other advantages of the Green's identity method are improved accuracy for the flow in concave corners and more reliable and efficient inverse solutions for design of multi-element sections with given pressure distributions.

A comparison of different numerical methods for the Green's identity formulation resulted in selection of the approach used in the 3-D program modification. Flat, trapezoidal panels with piecewise constant source density cover the body surface and panels with piecewise quadratic doublet density cover the body and the wake. Boundary conditions of zero perturbation potential are satisfied at an internal control point on each body panel and

at points on the edge of paneled sections. Special attention was given to reducing the discontinuity of doublet strength between adjacent panels. The internal doublet sheets used in the original program to provide lift carry-over through "non-lifting" bodies such as fuselages are not required in the modified program. The doublet distribution covers the outer surface of all body components, and the only distinction made between lifting and non-lifting components is in the joining of a wake to sharp trailing edges.

The program is written for the CDC CYBER 175 at Langley Research Center. Calculated results are presented showing the accuracy and stability of the modified program for isolated bodies, wings, wing-body combinations, and internal flow.

## INTRODUCTION

The surface panel method philosophy for solving arbitrary incompressible potential flow problems involves the mating of classical potential theory with contemporary numerical techniques. Classical theory is used to reduce an arbitrary flow problem to a surface integral equation relating boundary conditions to an unknown singularity distribution (Reference 1). The contemporary numerical techniques are then used to calculate an approximate solution to the integral equation. This involves representing flow boundaries by surface panels on which potential flow singularities are distributed.

All properly formulated surface panel methods are exact in the sense that the difference between the approximate numerical solution and the exact solution to the integral equation can be made arbitrarily small at the expense of increasing the number of computations. This does not imply that all panel methods are equally successful. Indeed, vast differences exist with respect to prediction accuracy versus computational effort, reliability, simplicity, and applicability to an inverse solution mode for design problems.

The Douglas Neumann surface source singularity computer program (reference 2) has been used extensively at industry, university, and government facilities around the world for predicting subsonic inviscid flow. For most geometries, the program predictions are accurate, efficient, and reliable. However, for wings with thin trailing edge regions and high loading, the program predictions can be inaccurate or numerically unstable. The instability results from local source singularities of extremely large magnitude.

This report describes the modification to the Douglas Neumann program to eliminate the difficulties associated with thin, highly loaded geometries. The basic concept involves replacing the source singularity formulation by the mild combined source-doublet distribution of the classical Green's identity.

The body of this report covers the theoretical fundamentals, the results of a study into numerical solution approaches for two-dimensional flow, the three-dimensional solution formulation, and representative numerical solutions for three-dimensional configurations. The section entitled Potential Flow Theory concentrates on the concepts of importance in establishing a reliable solution formulation. Included in the section Research on Green's Identity Formulation are the effects in two-dimensional flow of (1) the type of surface singularity distribution employed, (2) higher order panel curvature corrections, and (3) the method of applying boundary conditions. Of special concern were prediction accuracy, numerical stability, efficiency, and applicability to inverse design problems. Using the two-dimensional study as a guide, the modification formulation for the arbitrary lifting body Douglas Neumann program was developed and is presented in the section Numerical Solution Formulation. The example solutions in the section entitled Calculated Results include isolated bodies, wings, wing-body combinations, and internal flow.

## POTENTIAL FLOW THEORY

The solution to incompressible potential flow problems is based on the concept that arbitrary potential flow fields can be considered to be induced by suitable surface density distributions of singularities such as sources and doublets on the boundary contours. The utility of this concept is that simple flow fields induced by isolated singularities can be superimposed mathematically to generate fields having arbitrarily complex boundary geometries or boundary conditions.

This section provides background on the classical fundamentals of the theory, particularly the aspects pertinent to the formulation of a reliable and efficient numerical solution method. It will be explained that there is no limit to the number of different surface source-doublet distributions that will induce any given flow field and that there is no theoretical basis to favor one distribution over another. However, such is not the case when the theory is coupled with contemporary numerical techniques to establish a solution method. The type of singularity distribution selected can play an important role in solution efficiency and numerical stability. An understanding of the theoretical fundamentals is necessary before it is possible to determine how best to model the theory in a numerical formulation. In that regard, the rationale for selecting the combined source-doublet distribution of Green's identity will be presented below. Several two dimensional examples that quantitatively demonstrate the advantages will be presented in the following section.

### Laplace Equation

For the case of an incompressible, inviscid, and irrotational fluid, the Navier-Stokes equations can be reduced to the classical Laplace equation (reference 1). Consider the fluid in the region R of figure 1. The illustrated fluid boundaries can be solid such as an airplane wing, permeable such as the surface of a jet stream, or imaginary. Because the fluid is incompressible, continuity dictates that the divergence of velocity must be zero.

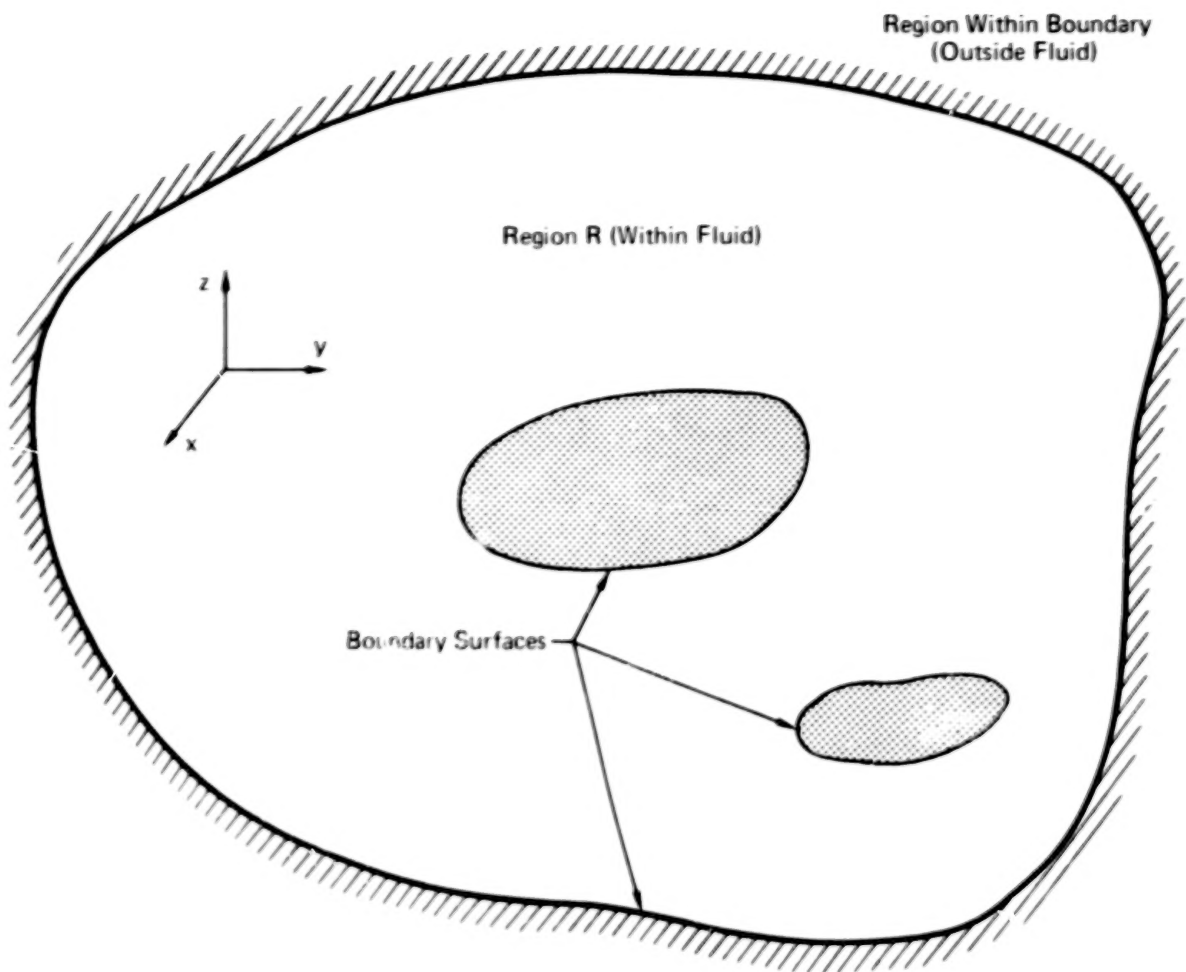


Figure 1. Illustration of a Bounded Fluid

$$\vec{\nabla} \cdot \vec{V} = 0 \quad (1)$$

The momentum equation is

$$\frac{D\vec{V}}{Dt} = - \frac{\vec{\nabla} p}{\rho} \quad (2)$$

where  $\frac{D}{Dt}$  is a material derivative, i.e., it refers to the time rate of change of a fixed set of fluid particles. By taking the curl of equation (2), it is possible to establish Kelvin's law that an initially irrotational, inviscid fluid will so remain. The mathematical consequence of zero vorticity ( $\vec{\nabla} \times \vec{V} = 0$ ) is that there exists a function  $\phi(x, y, z)$  which has a gradient equal to the velocity at each field point in the region R.

$$\vec{V} = \nabla \phi \quad (3)$$

Here it is assumed that the flow is initially irrotational, such as a free stream approaching a fixed airplane. The substitution of equation (3) into equation (1) generates the governing Laplace differential equation for incompressible potential flow.

$$\vec{\nabla} \cdot (\vec{\nabla} \phi) = \nabla^2 \phi = 0 \quad (4)$$

Equation (4) applies whether or not the flow is time dependent. In the special case of steady state, Bernoulli's equation is readily established by integrating equation (2) along a streamline path  $\vec{s}$  between any two points A and B.

$$\rho \int_A^B \frac{D\vec{V}}{Dt} \cdot d\vec{s} = - \int_A^B \vec{\nabla} p \cdot d\vec{s}$$

For steady flow, the differential  $d\vec{s}$  can be replaced by  $\vec{V}dt$ .

$$\rho \int_A^B \frac{DV}{Dt} \cdot \vec{V}dt = - (p_B - p_A)$$

$$\rho \left( \frac{V_B^2}{2} - \frac{V_A^2}{2} \right) = - (p_B - p_A)$$

$$p_A + \frac{1}{2} \rho V_A^2 = p_B + \frac{1}{2} \rho V_B^2 \quad (5)$$

If the region R is unbounded and point A is allowed to move indefinitely upstream, the conventional Bernoulli equation relating pressure and velocity is established.

$$C_p = \frac{p - p_\infty}{\frac{1}{2} \rho V_\infty^2} = 1 - \left( \frac{V}{V_\infty} \right)^2 \quad (6)$$



In the determination of the velocity field for irrotational flow, the application of equation (4) is equivalent to the simultaneous application of equations (1) and (2). The obvious advantage to equation (4) is that there exists only one unknown scalar function. For the usual case of steady flow, the solution to the velocity field is essentially the complete solution, since equations (5) or (6) provide the pressure directly from the local velocity. Forces and moments can then be generated by pressure integration. The essence of the solution method involves determining the potential function  $\phi$ .

#### Singular Solutions

A simple function which satisfies the Laplace equation is the potential due to a point source of strength  $m$  positioned at  $(x_0, y_0, z_0)$ .

$$\phi_S \equiv \frac{-m}{4\pi r} \quad (7)$$

where

$$r \equiv [(x-x_0)^2 + (y-y_0)^2 + (z-z_0)^2]^{\frac{1}{2}}$$

With the exception of the point  $(x_0, y_0, z_0)$ , the Laplacian ( $\nabla^2$ ) of equation (7) is zero. Since equation (4) need apply only to points in the flowfield, equation (7) satisfies the governing flow equation as long as  $(x_0, y_0, z_0)$  is on or within the non-fluid side of a flow boundary. Equation (7) is designated a particular solution. The term "source singularity" refers to the fact that the field induced by a source satisfies the Laplace equation everywhere except at the singular point  $(x_0, y_0, z_0)$ .

Because the Laplace equation is linear, the sum of any number of particular solutions is also a solution. Equivalently, any distribution of sources on or within flow boundaries is a solution to Laplace's equation.



Other particular solutions can be generated by differentiating equation (7) with respect to  $(x_0, y_0, z_0)$ . For example, the doublet function  $\phi_D$ , defined below, satisfies the Laplace equation except at the singular point  $(x_0, y_0, z_0)$ .

$$\phi_D \equiv \vec{n} \cdot \left( \frac{\partial \phi_S}{\partial x_0}, \frac{\partial \phi_S}{\partial y_0}, \frac{\partial \phi_S}{\partial z_0} \right) \quad (8)$$

The direction of unit vector  $\vec{n}$  is arbitrary. Physically, equation (8) describes the limiting situation of an equal strength source and sink on an axis parallel to  $\vec{n}$  (figure 2). The separation distance is equal to  $\Delta s$  and the source strength is  $\frac{m}{\Delta s}$ .

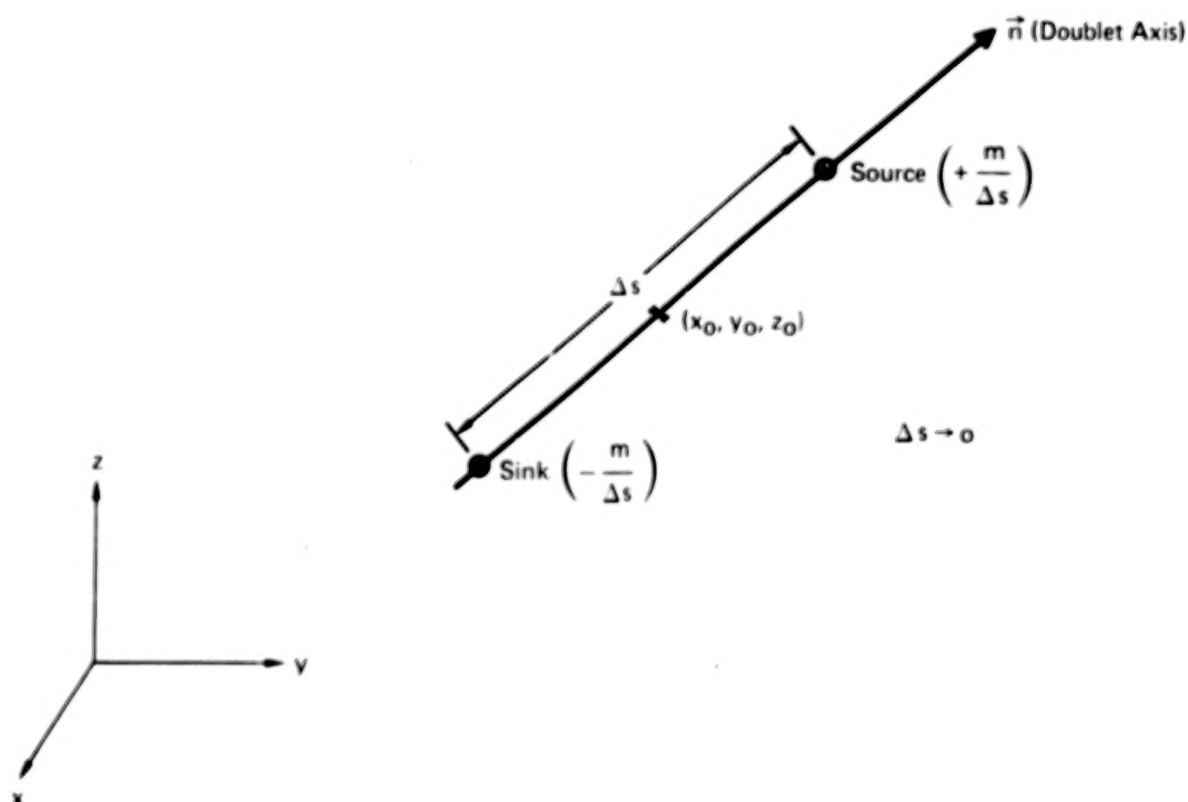


Figure 2. Point Doublet at  $(x_0, y_0, z_0)$

Any distribution of sources and doublets on or within flow boundaries automatically satisfies the governing Laplace equation. It is possible to demonstrate that any bounded potential flow field can be considered to be induced by a continuous distribution of sources and doublets (reference 1). Indeed, there is no limit to the number of different distributions that will induce any one given flow field. Once such a distribution is found, the solution is essentially complete because the flow potential and velocity at any point can be calculated directly as the integral sum of the individual differential contributions induced by the source and doublet distributions.

This study is restricted to the investigation of source and doublet singularity distributions on flow boundaries, not within. An example of the latter is the representation of the flow induced by a solid body of revolution immersed in a uniform stream. For some body shapes, it is theoretically possible to represent the effect of the body by an axial distribution of source singularities (figure 3). However, in the formulation of a numerical solution method, a distribution of singularities on the body surface provides a far more attractive model. It is desirable to have the singularities as close as possible to the flow which they induce. Otherwise, the distinction between the influences of neighboring regions of the singularity distribution is clouded, and numerical instabilities can result. This effect becomes more pronounced as body thickness increases.

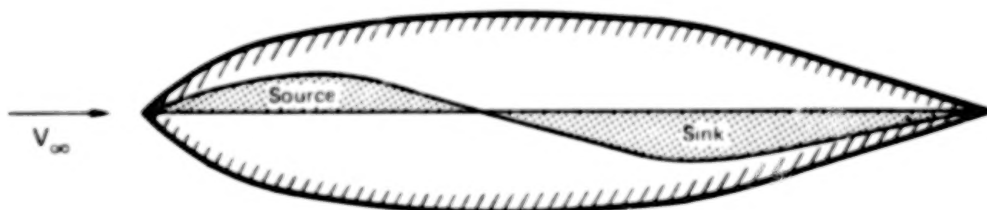
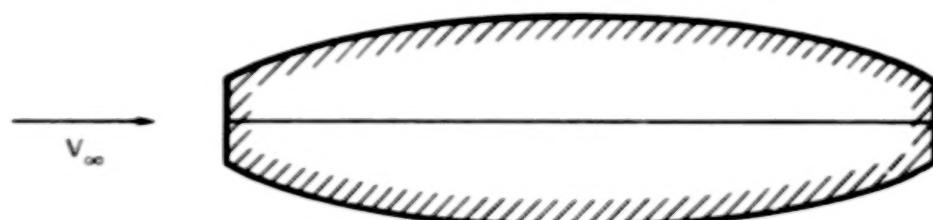


Figure 3. Body of Revolution Represented by an Equivalent Axial Singularity Distribution

Possibly a more compelling reason for avoiding internal singularities regards the existence of solutions. For bodies with flat disk noses or tails such as in figure 4, there is theoretically no axial distribution of sources that can induce the flow. On the other hand, there always exists a solution surface distribution of singularities on the flow boundaries.



**Figure 4. Body for Which No Equivalent Axial Singularity Distribution Exists**

In accordance with equations (7) and (8), it is possible to express the induced potential  $\phi$  at any field point P as the integral sum of continuous source and doublet distributions on boundary surfaces (see figure 5).

$$\phi = \oint \left\{ -\frac{\sigma}{4\pi r} + \frac{\mu}{4\pi} \frac{\partial}{\partial n} \left( \frac{1}{r} \right) \right\} dS \quad (9)$$

In equation (9), the following definitions are used:

- (1)  $\sigma$  and  $\mu$  are respectively the source and doublet strength per unit area on the boundary at arbitrary point Q,
- (2)  $dS$  is a differential surface area element at point Q,
- (3)  $r$  is the distance between boundary point Q and field point P, and
- (4)  $n$  is distance measured along an axis normal to the boundary surface at Q, positive into the flow.

Notice that the doublet axis direction in equation (9) is normal to the flow boundary.

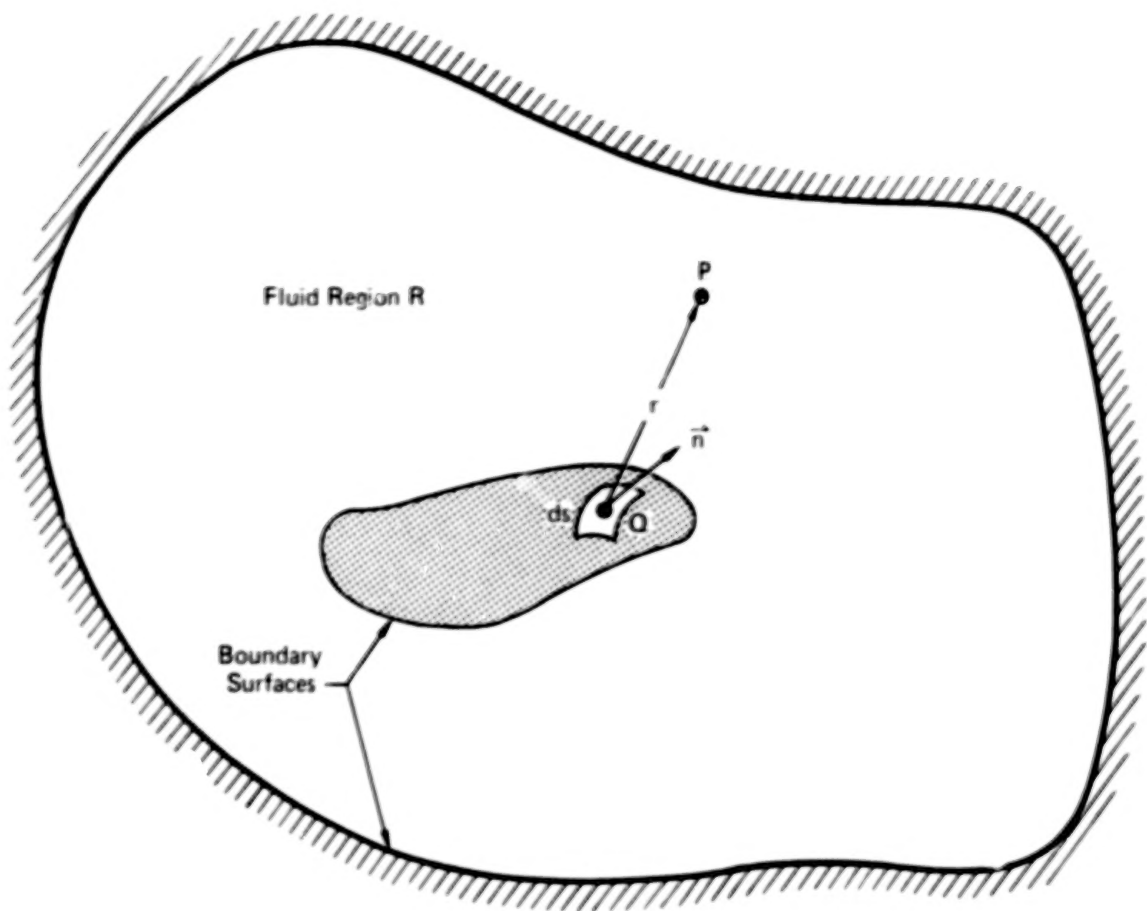


Figure 5. Points in a Fluid and on a Boundary

There is an important equivalence between surface doublet distributions and vorticity. As is proved in reference 2, a surface doublet distribution of density  $\mu$  can be replaced by an equivalent surface vortex distribution where the vortex density vector  $\vec{\gamma}$  at each surface point satisfies the following equation:

$$\vec{\gamma} = \vec{n} \times \nabla \mu \quad (10)$$

where  $\vec{n}$  is to be interpreted as the unit normal vector. Equation (10) follows from the fact that a vortex loop of strength  $\Gamma$  induces the same velocity at every field point as a uniform doublet sheet of density  $\Gamma$ , provided that the edges of the sheet lie on the loop (figure 6). The theoretical equivalency between vorticity and doublet distributions does not imply

equivalent simplicity in a numerical formulation. In this study, attention will be focused on doublets rather than vorticity, because distributions of scalars such as  $\mu$  are generally much simpler to handle than vector distributions such as vorticity.

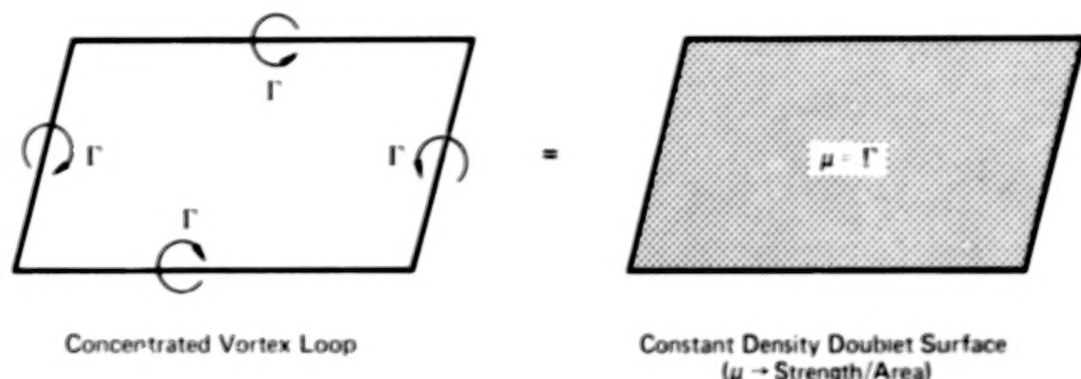


**Figure 6. Equivalency Between Vortex Loops and Doublet Surfaces**

For any bounded potential flow field, there exists a surface source distribution  $\sigma$  and doublet distribution  $\mu$  that will induce the field. Integral equation (9) describes the resultant potential at any field point  $P$ , and in accordance with equation (3), the gradient of equation (9) will give the flow velocity at point  $P$ . As discussed above, equation (9) satisfies the Laplace equation regardless of distributions  $\sigma$  and  $\mu$ . It remains to determine the appropriate distributions, and this is accomplished by satisfaction of boundary conditions.

#### Boundary Conditions

Within certain constraints on geometric slope continuity (reference 1), a bounded, simply connected velocity field is uniquely determined by the distribution on flow boundaries of either the normal component of total flow velocity  $\vec{v} \cdot \vec{n}$  or the total potential  $\phi$ . These boundary value problems are respectively designated Neumann and Dirichlet problems in the classical literature. In this study, primary consideration will be given to Neumann problems, because most practical cases involve prescribed normal velocity boundary conditions. In particular,

the flow tangency associated with solid bodies is expressed mathematically as  $\vec{\nabla}\phi \cdot \vec{n} = 0$ . All formulations in this study are sufficiently general to allow direct extension to arbitrary Neumann, Dirichlet, or mixed Neumann-Dirichlet boundary conditions.

The relationship between prescribed Neumann boundary conditions and the unknown source-doublet distribution is generated by taking the gradient of equation (9) and then allowing field point P to approach the boundary surface at arbitrary boundary point B. The normal velocity component at B is designated  $V_N$ .

$$\begin{aligned} \vec{\nabla}\phi &= \left( \frac{\partial}{\partial x}, \frac{\partial}{\partial y}, \frac{\partial}{\partial z} \right) \phi \\ &= \oint \left\{ -\frac{\sigma}{4\pi} \left( \frac{\partial}{\partial x}, \frac{\partial}{\partial y}, \frac{\partial}{\partial z} \right) \left[ \frac{1}{r} \right] \right. \\ &\quad \left. + \frac{\mu}{4\pi} \left( \frac{\partial}{\partial x}, \frac{\partial}{\partial y}, \frac{\partial}{\partial z} \right) \left[ \frac{\partial}{\partial n} \left( \frac{1}{r} \right) \right] \right\} dS \end{aligned} \quad (11)$$

$$V_N = \lim_{P \rightarrow B} \vec{\nabla}\phi \cdot \vec{n}_B$$

where  $\vec{n}_B$  is the unit normal vector at boundary point B.

The limiting procedure avoids contacting the singularities; this is necessary since the Laplace equation is satisfied arbitrarily close to a source or doublet location, but not at the location precisely.

There exists a solution distribution  $\sigma$  and  $\mu$  for any arbitrary normal velocity distribution  $V_N$ , provided that  $\oint V_N dS = 0$ . The integral constraint expresses the fact that the net fluid mass surrounded by the boundaries cannot change with time for incompressible flow. At each boundary point B there are two unknowns,  $\sigma$  and  $\mu$ , while there is one boundary condition, the prescribed value  $V_N$ . As one might expect, for any set of

boundary conditions, there is no limit to the number of different solution combinations of source-doublet distributions. In other words, there is no limit to the number of different surface singularity distributions that can theoretically induce the exact same field. The discussion to follow is intended to establish the particular source-doublet combination most suitable for application to a numerical solution formulation.

One possible candidate is a source-only distribution, with  $\mu$  set to zero a priori. The disadvantage is that source-only solution methods can generate strong numerical instabilities and unreliable predictions. The explanation is that for thin bodies at incidence, the solution source distribution tends to increase in magnitude linearly with respect to the inverse of thickness, while the net flow velocity changes only slightly. Prediction errors tend to be proportional to the singularity strengths. For a thin body, the average magnitude of source density can be several times that of the induced velocity, with a subsequent magnification of prediction error. An analogous situation could occur in measuring the distance  $\overline{AB}$  in figure 7. The distance could be determined indirectly by subtracting the measured distance  $\overline{BC}$  from measured  $\overline{AC}$ . In the absence of measuring errors,  $\overline{AB}$  is exactly  $\overline{AC} - \overline{BC}$ . However, if the relative error in taking a measurement is  $\epsilon$ , the indirect measurement would generate the following error  $\Delta\overline{AB}$ :

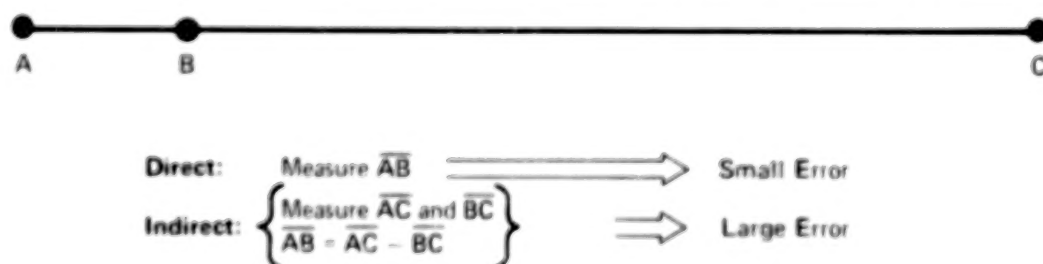


Figure 7. Direct and Indirect Measurements



$$\frac{\overline{AB}}{\overline{AB}} \approx 2\epsilon \frac{\overline{AC}}{\overline{AB}}$$

If  $\overline{AC}$  is sufficiently large, the error in measuring  $\overline{AB}$  would be greater than 100%. Obviously, one would be far better off measuring the distance  $\overline{AB}$  directly. In the same spirit, one would prefer to use singularity distributions of approximately the same magnitude as the induced flow velocities.

This can be accomplished by applying Green's third identity (ref.3, p.219). If the source distribution is established a priori by setting  $\sigma$  equal to  $V_N$  at each boundary point, and then if equation (11) is satisfied, it can be proved that  $\mu = \phi$  at each boundary point. By making these substitutions for  $\sigma$  and  $\mu$  in equation (9), Green's identity is established.

$$\phi = \oint \left\{ \frac{-V_N}{4\pi r} + \frac{\phi}{4\pi} \frac{\partial}{\partial n} \left( \frac{1}{r} \right) \right\} dS \quad (12)$$

The utility of Green's identity is that the singularities are no stronger than the flow field which they induce; indeed, there is a local equality regardless of geometry or boundary conditions. This contrasts sharply with source only solutions for thin geometries subjected to high lift. For the flow around conventional slotted flap high lift devices, the source densities can be orders of magnitude greater than the induced flow velocities.

The demonstration that setting  $\sigma = V_N$  results in  $\mu = \phi$  is straightforward if consideration is given to the imaginary flow field inside the real flow boundaries (figure 8). Subscripts E and I are used to designate the real external and imaginary internal fields, respectively. The following discontinuities apply to any sheet of sources and doublets.

$$\left. \begin{aligned} V_{NE} - V_{NI} &= \sigma \\ \phi_E - \phi_I &= \mu \end{aligned} \right\} \quad (13)$$



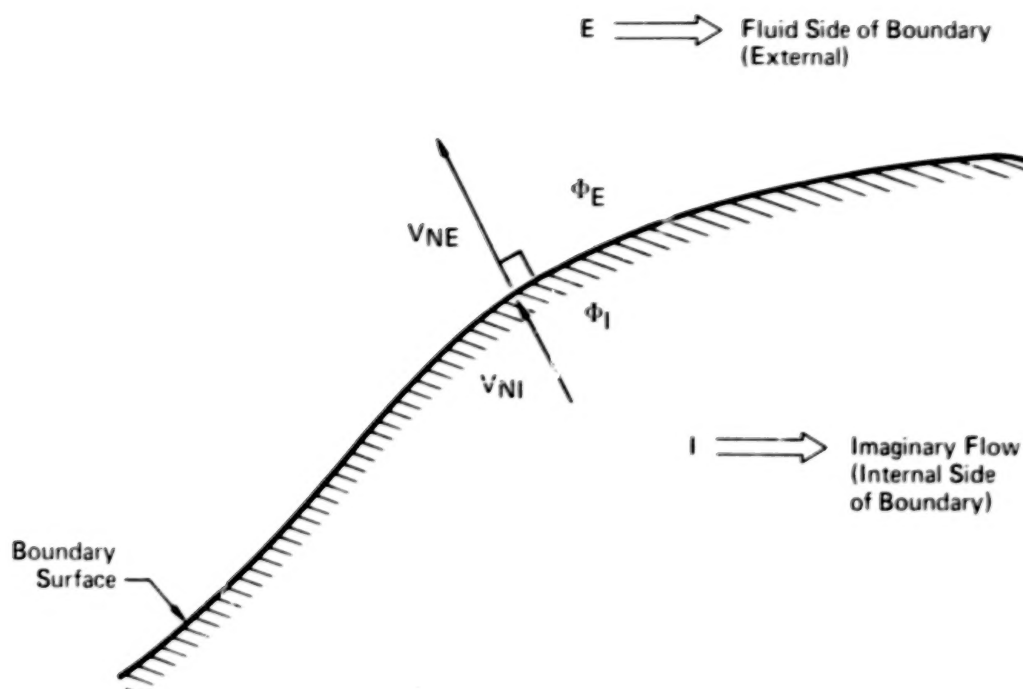


Figure 8. Two Sides of a Flow Boundary Surface

Both  $V_{NE}$  and  $V_{NI}$  are considered positive toward the real flow (direction  $\vec{n}$ ). Since  $\sigma = V_{NE}$ , it follows from equation (13) that  $V_{NI} = 0$ . The imaginary flow must be stagnant because the normal velocity component at all boundary points is zero and because such Neumann boundary conditions generate a unique solution. Therefore,  $\phi_I$  is a constant, which can be selected as zero. Finally, equation (13) indicates that  $\phi_E = \mu$ , completing the demonstration.

In most problems of interest the flow is unbounded. In that case, the surrounding boundary is allowed to increase indefinitely and its effect is replaced by adding a free stream of uniform velocity  $\vec{V}_\infty$ . However, Green's identity, as expressed by equation (12), still applies. Indeed, if solid bodies are immersed in the free stream, equation (12) indicates that  $\sigma = 0$  on the solid body surfaces and a doublet only representation results. As will be demonstrated later, convergence difficulties arise when doublet methods are applied to design problems.

By applying Green's identity to the perturbation potential instead of to the total potential  $\phi$ , a particularly useful combined source-doublet representation is defined (Reference 1). The representation will be shown to provide reliable solutions for both analysis and design problems. The perturbation potential  $\phi$  is defined as follows (see figure 9):

$$\phi \equiv \vec{V}_\infty \cdot (x, y, z) + \phi \quad (14)$$

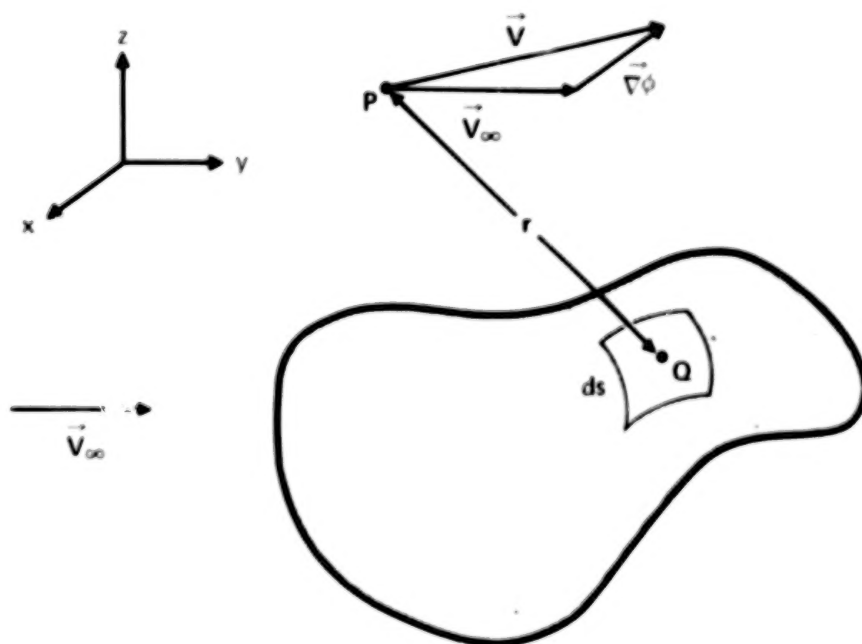


Figure 9. Body Immersed in an Unbounded Flowfield

To apply Green's identity to the perturbation potential,  $\sigma$  is replaced by  $\vec{\nabla}\phi \cdot \vec{n}$  (rather than  $\vec{\nabla}\phi \cdot \vec{n}$ ) and  $\mu$  is replaced by  $\phi$  (rather than  $\phi$ ).

$$\begin{aligned}\phi &= \oint \left\{ -\frac{\sigma}{4\pi r} + \frac{\mu}{4\pi} \frac{\partial}{\partial n} \left( \frac{1}{r} \right) \right\} dS \\ &= \oint \left\{ \frac{-\vec{\nabla}\phi \cdot \vec{n}}{4\pi r} + \frac{\phi}{4\pi} \frac{\partial}{\partial n} \left( \frac{1}{r} \right) \right\} dS\end{aligned}\quad (15)$$

where  $\vec{\nabla}\phi \cdot \vec{n} = V_N - \vec{V}_\infty \cdot \vec{n}$ ;  $\vec{V}_\infty \cdot \vec{n}$  is a simple function of local geometry. Because  $\phi$  approaches zero at infinity, there is no need to include a surrounding boundary, which considerably simplifies the formulation of a numerical solution method. In equation (15) the singularity densities  $\sigma$  and  $\mu$  are equal to the perturbation normal velocity and perturbation potential, respectively. If the perturbation flow vanishes, so do the singularities which induce the flow. Hereinafter, the term "Green's identity" refers to equation (15).

The singularities of Green's identity are mild, and there are no more unknowns than for a source only formulation. For Neumann problems the source density distribution is known a priori

$$\sigma = \vec{\nabla}\phi \cdot \vec{n} = V_N - \vec{V}_\infty \cdot \vec{n}\quad (16)$$

and the doublets are to be determined. For Dirichlet problems, the opposite occurs; the doublet distribution is known from the prescribed potential distribution on the boundaries, and the source distribution is to be determined. The approach of applying Green's identity to a numerical solution method is believed to have been first employed by Morino, et al (reference 4).

The equivalency between a doublet distribution and vorticity as expressed by equation (10) results in a useful equality for Green's identity. Since  $\mu = \phi$  on boundary surfaces and since  $\vec{V} = \vec{V}_\infty + \vec{V}_\phi$ , it follows that the tangential component of perturbation velocity on the surface will be equal in magnitude and normal in direction to the vorticity density vector  $\vec{\gamma}$ . Figure

10 illustrates the situation for the special case of two-dimensional flow. The total flow velocity vector  $\vec{V}$  is seen to consist of components  $V_T$  and  $V_N$  where

$$\left. \begin{aligned} V_T &= V_{T_\infty} + \gamma \\ V_N &= V_{N_\infty} + \sigma \end{aligned} \right\} \quad (17)$$

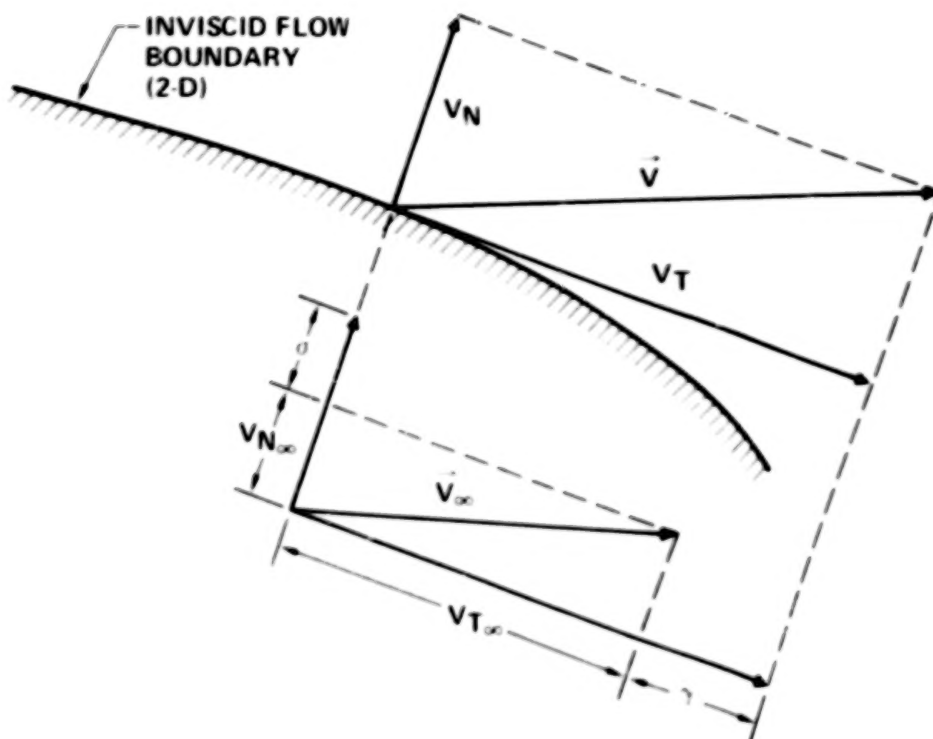


Figure 10. Surface Velocity Corresponding to Green's Identity

An illustration of the nature of three different singularity distributions which induce exactly the same flow field is presented in figure 11. The problem is to calculate the flow about a solid two-dimensional circular cylinder immersed in a uniform stream  $\vec{V}_\infty$ . The analytical singularity distributions are presented for a source only solution, doublet only solution (Green's identity applied to total potential  $\phi$ ), and the combined source-doublet distribution corresponding to Green's identity (applied to perturbation potential  $\phi'$ ). For clarity, the equivalent vortex density  $\gamma$  is presented instead of doublet density.

It is noteworthy that the combined source-vortex solution is the average of the source only and vortex only solutions. Green's identity typically provides a source distribution more mild than the source only solution and a vortex distribution more mild than the vortex only solution.

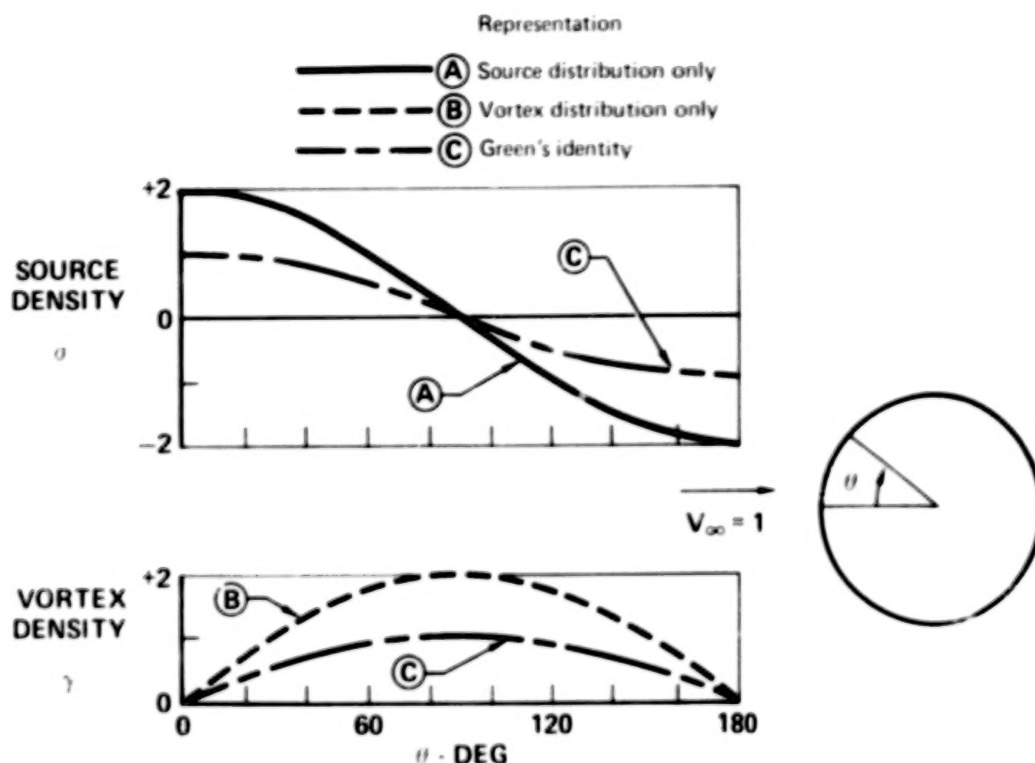


Figure 11. Equivalent Singularity Representations for a Circular Cylinder

Green's identity also offers the prospect for using internal indirect boundary conditions (reference 4). In solving Neumann problems, the first step is to set  $\sigma = V_N - \vec{V}_{\infty} \cdot \vec{n}$ , where  $\vec{V}_{\infty} \cdot \vec{n}$  is a function of geometry only. The second step for direct boundary condition satisfaction is to solve for  $\mu$  by satisfying equation (11) at each boundary point. However, it can be shown to be theoretically equivalent to establish zero perturbation potential on the imaginary or internal side of all flow boundaries. The proof follows immediately from equation (13).

The advantages of Green's identity in the application to a numerical solution method are summarized below.

- (1) Mild combined source-doublet distributions suppress numerical instabilities, which can otherwise be prevalent for thin high lift geometries.
- (2) Singularity distributions vanish as the perturbation field vanishes, thereby eliminating possible residual error.
- (3) Direct relationships between velocity and singularity strengths on boundary surfaces exist which simplify calculations.
- (4) Possibility exists of applying indirect internal boundary conditions to simplify calculations.

One additional advantage is in the application to design or inverse problems, for which the geometry most nearly corresponding to a prescribed velocity distribution is to be determined. Even though doublet only analysis problem solutions are relatively mild, they tend to be unsuitable for inverse problem application in leading edge regions. Supporting two-dimensional examples and the explanation will be furnished in the next section.

#### Wakes

It is possible to prove that the net force on all bodies immersed in a steady, incompressible, potential flow field is zero (reference 1). In other words, an airplane would have no lift in a fully potential fluid. On the other hand, it is commonplace to solve aerodynamic problems by representing lifting airplanes as solid bodies immersed in a potential fluid. The representation is made reasonable by the introduction of an additional flow boundary, the semi-infinite trailing wake.

The need for a wake can be illustrated by considering flow circulation. Consider a section of an airplane wing (figure 12). The circulation  $\Gamma$  is defined as

$$\Gamma = \oint_{A^+}^{A^-} \vec{V} \cdot d\vec{l} \quad (18)$$

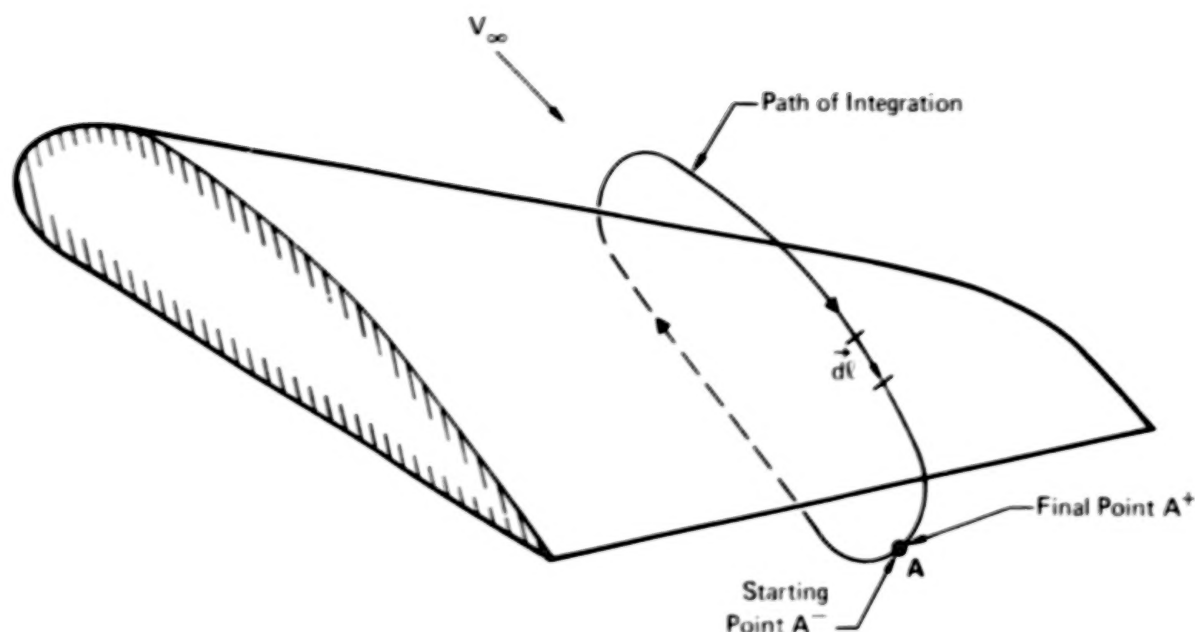


Figure 12. Circulation Around a Wing Section

where the path of integration is a closed contour in the fluid surrounding the wing. If the fluid were to satisfy Laplace's equation everywhere, then equation (3) could be substituted into equation (18).

$$\Gamma = \oint \vec{\nabla} \phi \cdot d\vec{l} = \phi_{A^+} - \phi_{A^-}$$

The circulation would be zero because  $\phi$  would have to be continuous at A to satisfy Laplace's equation. Of course, a lifting wing possesses circulation, and therefore the fluid cannot realistically be described by Laplace's equation alone. The missing ingredient is the effect of viscosity at sharp edges.

Potential fluids theoretically generate infinite velocity gradients at sharp convex corners such as at wing trailing edges. Regardless of free stream Reynolds number, the action of viscosity will be felt if velocity gradients are sufficiently strong. Therefore, even what is conventionally designated an inviscid fluid will demonstrate the effects of friction at a sharp trailing edge. The fluid will search for a finite velocity



at the sharp edge, corresponding to what is referred to as the Kutta condition. The fluid in this localized trailing edge viscous region will be carried downstream to form a region which cannot be described by Laplace's equation. This viscous region is, of course, the wake.

As free stream Reynolds number increases, the thickness of the wake region diminishes and is often assumed to be zero. Nonetheless, the fluid properties are discontinuous across the wake and the wake itself cannot be neglected. Usually the wake is modelled as a stream surface having zero pressure loading imposed by the surrounding flow. These two free stream surface conditions are sufficient to determine the two sets of unknowns, wake geometry and wake singularity distribution.

A frequently used assumption for wake geometry that is approximately correct for sufficiently high Reynolds numbers and small flow perturbations is that the wake is a flat surface emanating from the trailing edge and parallel to the free stream. The condition of zero loading is represented by the small disturbance approximation of zero vortex strength along lines normal to the free stream (Figure 13). Equivalently, the streamwise gradient of wake doublet density is assigned the value zero.

The two-dimensional flow analogue to a wake is a streamline along which velocity is continuous but potential is discontinuous. The strength of the discontinuity is equal to the circulation and is dictated by the Kutta condition of finite trailing edge velocity. In its simplest form, the Kutta condition is to be considered an approximation to the viscous part of the flow problem.

In this study, the wakes are represented by a doublet sheet having zero thickness and zero streamwise doublet gradient. The wake geometry, though not necessarily flat, is specified. In the case of multi-component wings such as slats and slotted flaps, each component is assigned a separate wake.



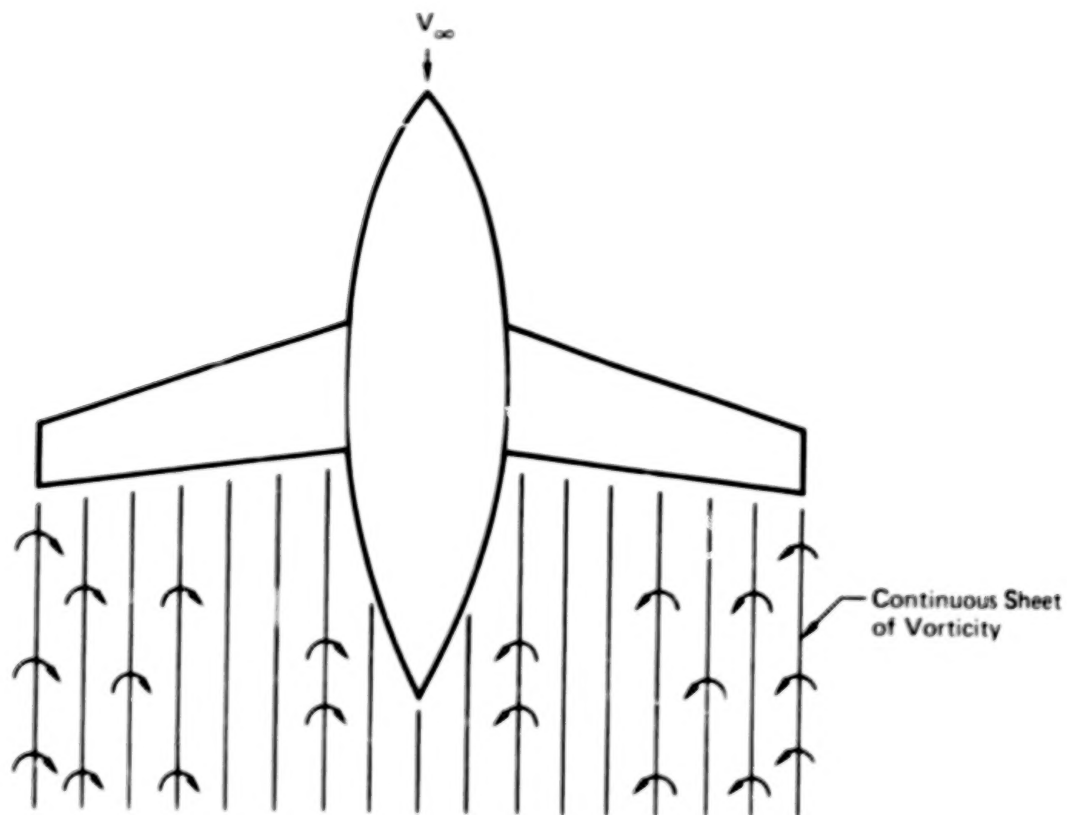


**Figure 13. Simple Wake Model**

## RESEARCH ON GREEN'S IDENTITY FORMULATION

A study was made in a two-dimensional surface paneling formulation to give a better understanding of the Green's identity method, as a basis for selecting the numerical methods to be used in applying the Green's identity formulation in the 3-D program. A large number of formulations could be compared using available programs, and essentially "exact" calculations could be made by transformation methods (references 5, 6) to compare the accuracy of the different methods.

The classical potential theory of the previous section reduces an arbitrary flow problem to a surface integral equation relating boundary conditions to an unknown singularity distribution. Numerical techniques are then used to calculate an approximate solution to the integral equation. Paneling methods do this by dividing the surface into a number of panels with a source or doublet singularity density distribution of unknown magnitude on each panel. The singularity densities are then calculated by solving a set of equations satisfying boundary conditions at control points on each panel plus additional Kutta conditions for the circulation to give smooth flow at Kutta points on the trailing edge of lifting surfaces.

Many conceivable approaches are available for formulating surface paneling methods (references 2, 4, 7-18). At the level of potential theory, an unlimited number of combinations of source and doublet singularity distributions can induce a given external flow field. Our main interest in this study is in the particular source-doublet combination defined by Green's identity, as well as the source only method used in the original 3-D Douglas Neumann program. Additional choices can be made of the numerical techniques to be used. The results of a study into the merits of the various approaches are presented in this section.

## Comparison of Surface Paneling Methods

The principal distinguishing features of surface paneling methods are (1) choice of representative singularity distribution, (2) numerical scheme for distributing the singularities, (3) type of boundary conditions employed, and (4) conversion of solution singularity densities to velocity. A study was made to determine which selections in the above four categories provide the most desirable characteristics in terms of prediction accuracy, computational efficiency, and numerical stability for both analysis and design.

Special attention was given to problems for which the Green's identity formulation showed promise of significant improvement compared to the original Douglas Neumann source method. The Douglas Neumann method uses flat, constant density source panels, plus a constant vorticity (or linear doublet) distribution around an airfoil or wing to give the circulation which satisfies a Kutta condition of equal pressure on the upper and lower surface panels next to the trailing edge. Reference 8 discusses some problems with this method resulting from large source densities on thin, highly loaded surfaces. The accuracy can also be poor when the panel number around a section is reduced to the range of 20 to 40, typical of 3-D applications, due to inaccurate circulation and panel curvature effects. As discussed later in this section, the Douglas Neumann method erroneously predicts unbounded velocities as a sharp, concave corner is approached. These characteristics present difficulties in applying the method to problems of current interest, such as supercritical airfoils and strongly cambered high lift devices such as slats and vanes. Accordingly, the study included analysis and test cases related to (1) accuracy vs panel number and panel distribution, (2) thin surfaces, with a small value of the ratio of distance between panels to panel length, (3) method of applying the Kutta condition, and (4) flow in concave corners.

Table I indicates the combinations of formulation approaches which were tested on two-dimensional sample problems during the study. The designations "low order" and "high order" refer to the numerical scheme for modeling the surface singularity distributions. In every case, the low order scheme incorporates a piecewise constant strength source distribution, a continuous piecewise linear vortex strength distribution, and flat surface panels. The high order scheme includes corrections for local source gradient and panel curvature in accordance with reference 8. Boundary conditions are normally applied directly at one control point per panel. For both the doublet and Green's identity approaches, theoretical relationships exist between local singularity strength and local velocity which can be used to provide either an equivalent internal potential boundary condition in lieu of prescribed normal velocities or a convenient means for calculation of velocity from singularity strength.

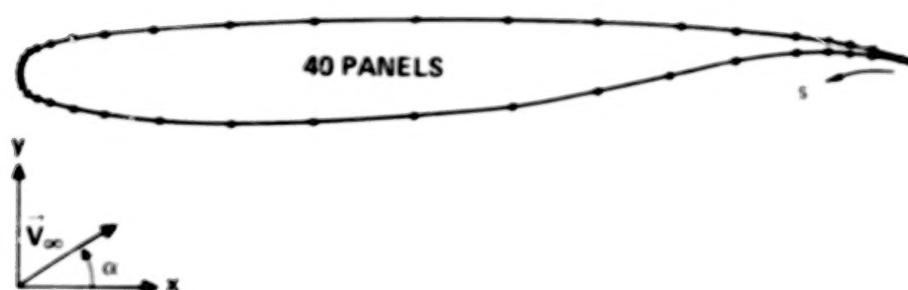
TABLE I. 2-D SURFACE SINGULARITY METHODS TESTED

Singularity	Surface Paneling		Boundary Conditions		Velocity Calculation		
	Low Order	High Order	Normal Velocity	Internal Potential	Influence Coefficient Summation	Local Singularity Strength	Inverse Solution Mode
1. Source	X	X	X		X		
2. Doublet	X		X		X	X	X
3. Combined Source-Doublet							
a. Least Squares (Reference 17)	X		X		X		X
b. Symmetric Singularities (Reference 18)	X		X		X		X
(1)	X		X		X	X	
c. Green's Identity (2)		X	X		X	X	
(Ref 19-21) (3)	X			X		X	X

Existing computer programs were available to MCAIR for all the combinations listed in Table I, except for the application of internal potential boundary conditions to a Green's identity formulation (which was developed as part of this contract effort), and the inverse (or design) capability for the Green's identity formulation with internal potential boundary conditions (which was recently developed in a separate MCAIR supported effort.) Documentation of the earlier programs is available in references 17-20, as noted in Table I, and the two new Green's identity programs are discussed later in this section (also see Reference 21).

Detailed discussion and supporting examples comparing most of the formulation approaches indicated by Table I have been provided in references 17, 19, and 20 and will not be duplicated here. However, the more significant characteristics are repeated below.

1. Source methods are numerically unstable for thin highly loaded geometries, which results from using unnecessarily strong singularity densities to induce a flow field. (See figure 14).
2. Doublet methods fail near leading edges in design problem iterative solutions. This is the consequence of the theoretical equivalence between doublet gradient and local velocity. In low speed regions, the combination of low flow velocity and low singularity strength numerically decouples the effect of local geometry from velocity, and the result is numerical instability. (See figure 15).
3. The combined source-doublet combination obtained by the least squares approach of reference 17 is numerically stable for both analysis and design. However, the least squares procedure results in a significant increase in computational expense by increasing the number of unknowns.
4. The symmetrical singularity approach of reference 18 is unstable for design.



# SUPERCritical AIRFOIL GEOMETRY

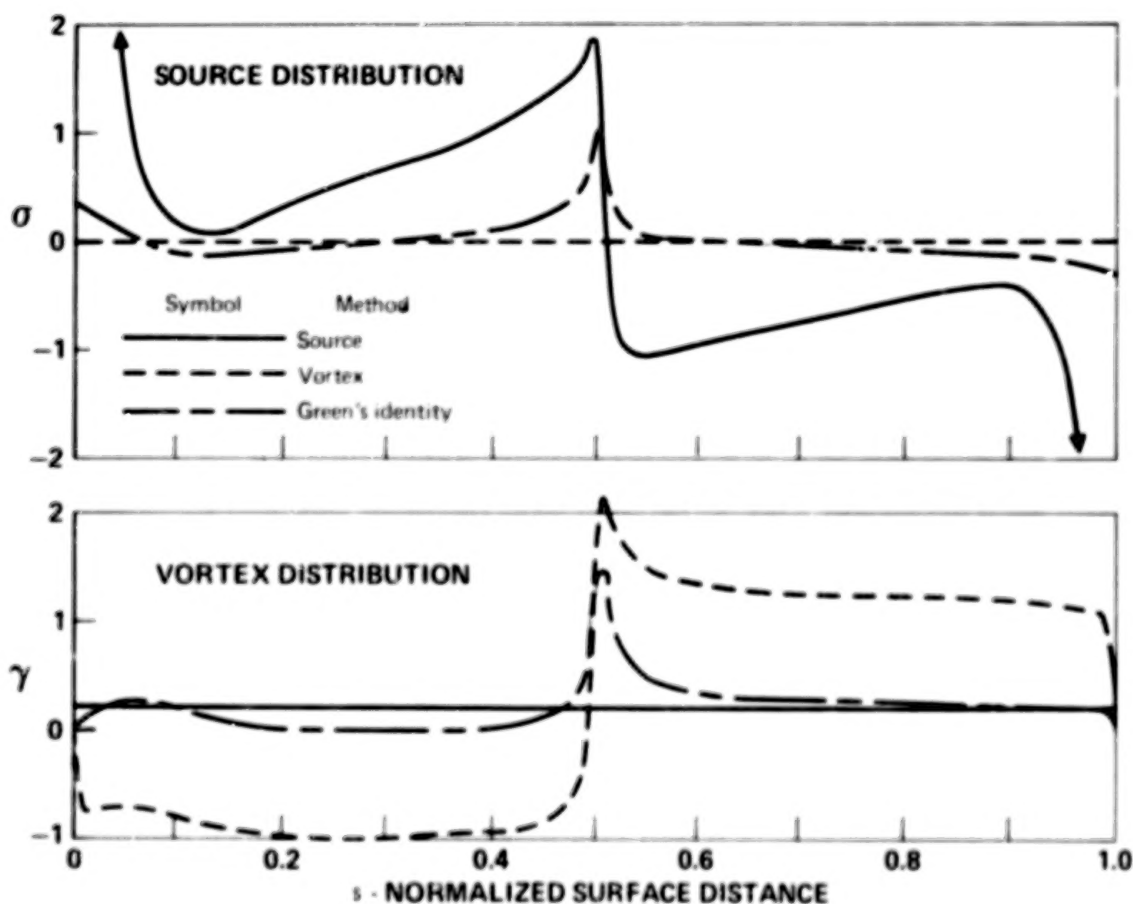
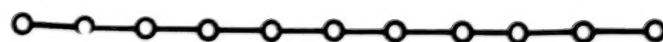
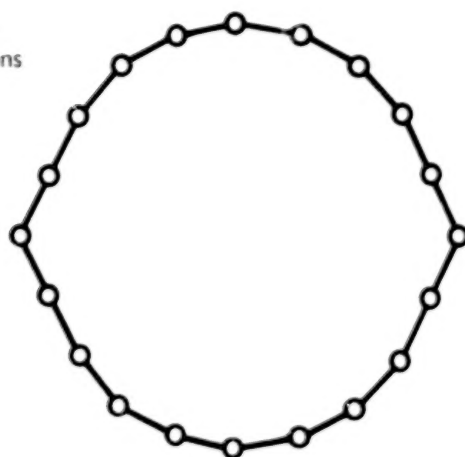


Figure 14. Singularity Distributions for Supercritical Airfoil at  $4^\circ \alpha$

Starting Geometry



After  
2 Iterations



After  
7 Iterations  
(Not  
Converged)

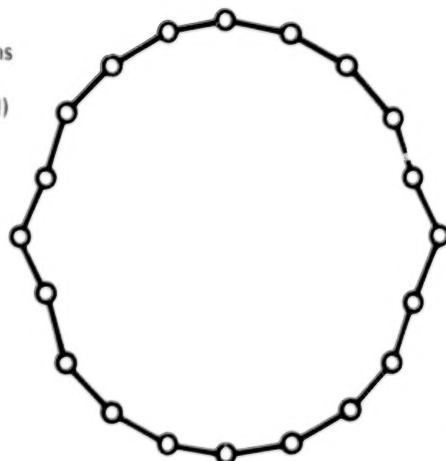


**Figure 15. Circular Cylinder Inverse Solution**  
(Vortex Only Method)

5. The mild combined source-doublet distribution corresponding to Green's identity generates numerically stable results with none of the additional expense associated with least squares.
6. The high order numerical scheme applied to flow tangency boundary conditions provides increased accuracy compared to low order at only a slight increase in computational expense and with no increase in numerical instability. (See figure 16).
7. If flow tangency boundary conditions are applied to the high order Green's identity method, the velocity calculated by summing the individual contributions of each panel is significantly more accurate than applying the relationship between local velocity and local singularity density.

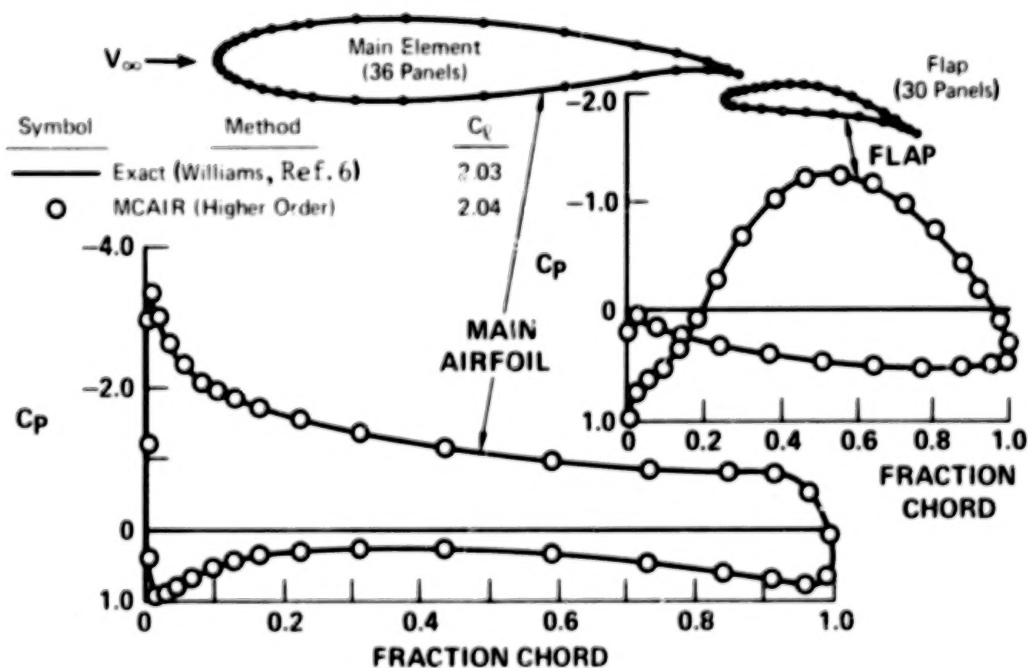


Figure 16. Two-Element Airfoil Inviscid Solution



8. The mild singularity distribution near the trailing edge from Green's identity permits improved accuracy of circulation, by a Kutta condition of wake tangency (zero normal velocity) at a point on the trailing edge bisector a few percent of the trailing edge panel length downstream of the trailing edge.

#### Internal Potential Boundary Condition Formulation

Inasmuch as no computer program which could handle internal potential boundary conditions was available to MCAIR at the start of this contract study, the above enumerated characteristics of surface singularity methods do not include consideration of potential boundary conditions. Therefore, an appropriate computer program was formulated and tested during this reporting period. The remainder of this section is dedicated to a brief explanation of the program formulation, the presentation of illustrative examples, and the resulting conclusions.

As implied by equation (17) and illustrated in figure 10, Green's identity implies that if the source density  $\sigma$  everywhere on a geometry satisfies the relationship

$$\sigma = V_N - V_{N_\infty} \quad (19)$$

then it follows that the vortex density  $\gamma$  will satisfy the following equation

$$\gamma = V_T - V_{T_\infty} \quad (20)$$

Here subscripts N and T refer to the surface normal and tangential directions respectively, V is velocity, and  $\infty$  refers to free stream conditions. It is simple to demonstrate that if equations (19) and (20) are satisfied, the flow field inside the body is uniform with velocity  $V = V_\infty$  (reference 19). Equivalently, the disturbance potential  $\phi$  inside the body will be a constant, and this fact can be utilized to generate equivalent internal potential boundary conditions. The procedure, first applied by Morino, et al, (reference 4) is as follows:

1. Calculate the source density  $\sigma$  on each panel from equation (19).  $V_N$  is known a priori from prescribed Neumann boundary conditions and  $V_{N_\infty}$  is a function of local surface slope only.
2. Calculate the local vortex density on each panel by solving a system of linear equations corresponding to a constant internal perturbation potential at each panel control point.
3. Calculate the velocity at any field point directly from the solution source-vortex distribution.

For airfoils having sufficiently small camber and thickness, it can be demonstrated that the above solution procedure is equivalent to small disturbance, linearized boundary condition flow theory. The demonstration is based on the fact that along any internal path connecting any two control points the average perturbation velocity component parallel to the path is zero. This is a direct consequence of having the same perturbation potential at all internal control points. Along a path connecting upper and lower surface control points at a given chordwise station, the average perturbation velocity component normal to the chord will be zero. The source contribution to this zero average is approximately equal to the free stream velocity component normal to the local camber, a fact which is easily verified by considering the difference between the upper and lower surface source densities (Equation 19). The source induced normal velocity must be offset by the vortex contribution in order to attain the magnitude of zero. Therefore the average of the upper and lower surface vorticity is uniquely determined by the camber and incidence in the same manner as for linearized flow theory. Thickness effects can be understood by considering the average perturbation velocity along a chordwise path between two internal control points on either the upper or lower surface. Because the average of the upper and lower surface sources is approximately equal to the thickness slope (Equation 19), the source contribution to the internal chordwise velocity is the same as the thickness-induced tangential velocity

of linearized flow theory. The vortex-induced internal velocity along the chord line will offset the source contribution, with the result that the difference between upper and lower surface vorticity is twice the thickness-induced velocity of linearized flow theory. The consequence of the similarity between the application of internal potential boundary conditions and small disturbance linearized flow theory is that for sufficiently thin, planar geometries, both approaches will generate similar numerical behavior. In that regard, the uniform strength source-doublet quadrilateral panel method of Morino (Ref 4) actually reduces to a conventional vortex lattice method as thickness approaches zero.

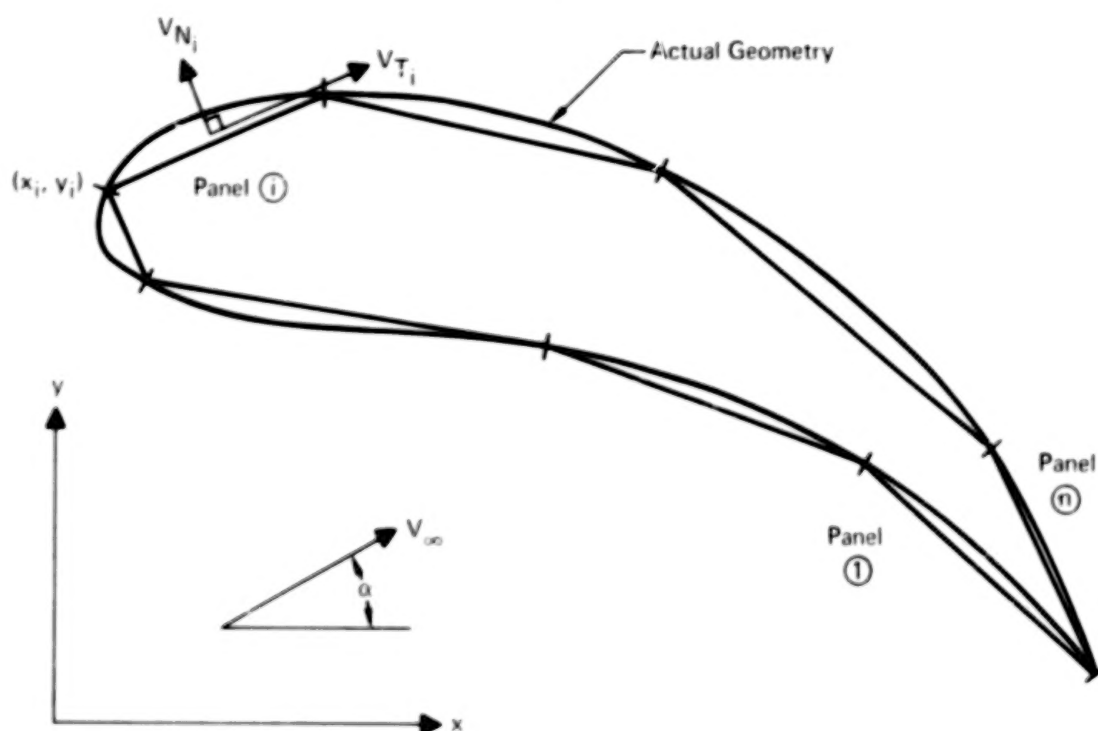


Figure 17. Two-Dimensional Panel Modeling  
(Flat Panels)

In the present formulation, a low order modeling was used (piecewise uniform source, continuous piecewise linear vorticity, flat panels). See figure 17. At the center or control point of each panel  $i$ , the internal perturbation potential is designated  $\phi_i$ . Uniform internal perturbation potential at each control point is obtained by satisfying the following system of equations:

$$\Delta\phi_i \equiv \phi_{i+1} - \phi_i = 0 \quad (1 \leq i \leq n-1) \quad (21)$$

where  $n$  is the number of panels used to model the airfoil element. An additional equation is introduced to fix the circulation. At the discretion of the user, the circulation can either be prescribed explicitly or generated implicitly by a Kutta condition. The unknowns are the vortex densities at the  $n$  panel endpoints. The source densities are known a priori from equation (19).

After solving the system of linear equations for the unknown vortex densities, the surface velocity can be computed either by summing the effects of the individual panel singularity distributions or by resorting to equations (19) and (20), which provide a direct relationship between local velocity and local singularity density.

In order to solve equation (21), it is first necessary to establish the linear relationship between potential and the source-vortex distributions on a panel. Consider a panel of length  $s$  in Figure 18. The following equation provides the potential at an arbitrary point  $(\xi_0, \eta_0)$  induced separately by a constant source density, constant vortex density, and linear vortex density on the panel.

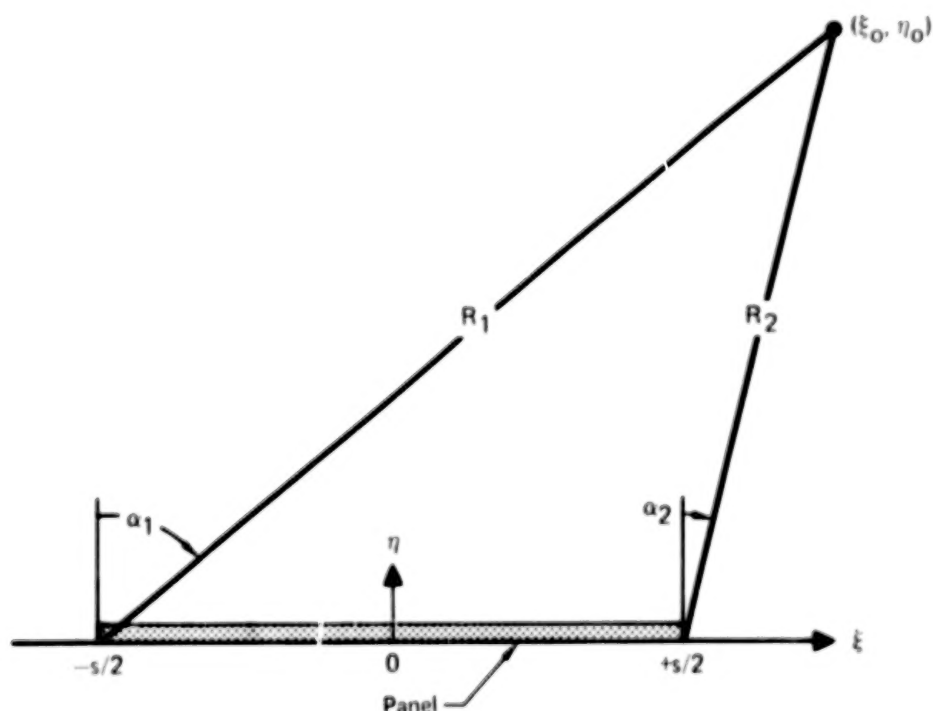


Figure 18. Coordinate System for a Panel of Length  $s$

$$\sigma = 1 \quad \left(-\frac{1}{2}s \leq \xi \leq +\frac{1}{2}s\right)$$

$$4\pi\phi = -2s + 2\eta_o (\alpha_1 - \alpha_2) - \xi_o \ln \left(\frac{R_2}{R_1}\right)^2 + \frac{1}{2}s \ln (R_1 R_2)^2$$

$$\gamma = 1 \quad \left(-\frac{1}{2}s \leq \xi \leq +\frac{1}{2}s\right)$$

$$4\pi\phi = -(2\beta + \pi)s + 2\xi_o (\alpha_1 - \alpha_2) + s(\alpha_1 + \alpha_2) + \eta_o \ln \left(\frac{R_2}{R_1}\right)^2$$

$$\gamma = \xi/s \quad \left(-\frac{1}{2}s \leq \xi \leq +\frac{1}{2}s\right)$$

$$4\pi\phi = \eta_o + \left(\xi_o^2 - \eta_o^2 - \frac{1}{4}s^2\right) \left(\frac{\alpha_1 - \alpha_2}{s}\right) + \left(\frac{\xi_o \eta_o}{s}\right) \ln \left(\frac{R_2}{R_1}\right)^2$$

$$\text{where: } \alpha_1 \equiv \tan^{-1} \left(\frac{\xi_o + \frac{1}{2}s}{\eta_o}\right)$$

$$\alpha_2 \equiv \tan^{-1} \left(\frac{\xi_o - \frac{1}{2}s}{\eta_o}\right)$$

$$R_1^2 \equiv \left(\xi_o + \frac{1}{2}s\right)^2 + \eta_o^2$$

$$R_2^2 \equiv \left(\xi_o - \frac{1}{2}s\right)^2 + \eta_o^2$$

$$\beta \equiv \begin{cases} 0 & (\eta_o \geq 0) \\ \pi & (\eta_o < 0) \end{cases}$$

(22)

It is noteworthy that the vortex induced potential is discontinuous at  $\eta_o = 0$  for  $\xi_o > 0$ . In establishing  $\Delta\phi_i$  for equation (21), it is necessary to eliminate the effect of the discontinuity. This can be accomplished by interpreting  $\Delta\phi_i$  as the line integral of velocity along any internal path between control points  $i$  and  $i+1$ . For convenience, the selected path follows the surface of panels  $i$  and  $i+1$ . If this path crosses  $\eta_o = 0$  for  $\xi_o > 0$ , then a value equal in magnitude to the potential discontinuity is subtracted to eliminate the effect of the discontinuity.

Special treatment is applied if there are any slope discontinuities on the airfoil surface, such as a sharp trailing edge. At each panel endpoint that is designated a sharp corner, a discontinuity is allowed in the vortex density. This corresponds to the fact that theoretically the perturbation velocity is discontinuous at a corner. The magnitude of the vortex density hop at the panel endpoint is an additional unknown which is determined through the introduction of an internal control point a few percent of panel length from the corner. The imposition of uniform internal perturbation potential is applied to each sharp corner control point, as well as to the panel center points.

Computing time is nearly independent of the type of boundary condition applied. For either the direct flow tangency or indirect internal potential methods, essentially the same terms are required for influence coefficient calculation and the same number of linear equations must be solved.

#### Comparison of Green's Identity Formulations

The present low order Green's identity panel method using potential boundary conditions has been compared with both the low and high order Green's identity formulations of references 19 and 20, in which the conventional prescribed normal velocity boundary condition is applied at each panel control point. It is noted that in every test case for which velocity or pressure is illustrated in the results to be presented below, equation (20) was applied for the potential boundary condition method and the individual effects of the panels were summed for the other two methods. This corresponds to what has proved to generate the best prediction accuracy in each case. In selected cases, results are also presented for the low order Douglas Neumann source method which uses piecewise constant source density, uniform surface vorticity, and flat panels. This source method is analogous to the existing three-dimensional Douglas Neumann Program of reference 2. In every example for which there is lift, the same net integrated vorticity was used for all the methods in order to avoid the clouding effects of different Kutta conditions.



The test case solid-body geometries cover a wide range of shapes and thicknesses. Included are a circular cylinder, Karman-Trefftz airfoil, supercritical airfoil, nearly flat plate with noisy coordinate definition, and a thin symmetrical airfoil at zero incidence. The symbols used in the figures for all cases are defined as follows:

- Low order Green's identity with potential boundary conditions
- △ Low order Green's identity with normal velocity boundary conditions
- High order Green's identity with normal velocity boundary conditions
- ◇ Low order Douglas Neumann

For the example involving a circular cylinder, the objective was to determine prediction accuracy versus panel density. Two panel models were established, one using twenty and the other using forty equally spaced panels. By comparing the calculated surface vortex density  $\gamma$  against the exact analytical value corresponding to Green's identity, it was possible to establish the root-mean-square error in vorticity around the cylinder. The results are as anticipated for the case involving prescribed normal velocity boundary conditions, i.e., flow tangency (figure 19). Consistent with the explanation of reference 20, the low order prediction error is proportional to the inverse of panel density and the high order error is proportional to the square of the inverse of panel density. What was unforeseen (as shown in figure 19) is that the prediction error for the low order solution with internal potential boundary conditions exhibits higher order characteristics; that is, the error varies proportionately to the square of the inverse of the number of panels.

Similar trends are apparent for a thin, highly loaded Karman-Trefftz airfoil (figures 20 and 21). The virtually exact conformal mapping technique of Catherall-Sells (reference 5) was used to provide a standard of comparison. Both in the 25 panel representation of figure 20 and in the stagnation region of a 50 panel representation (figure 21), the calculated velocity

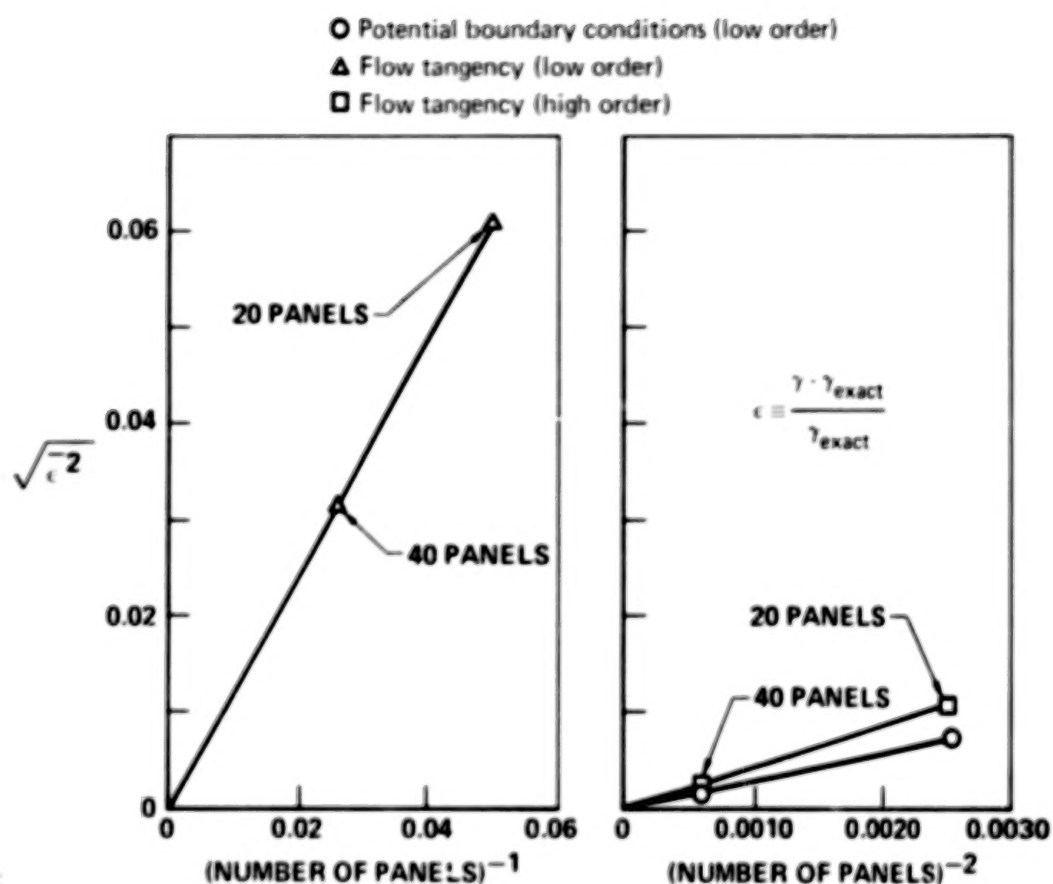


Figure 19. Prediction Accuracy for a Circular Cylinder

and pressure distributions for the low order potential boundary condition solution are very accurate and nearly identical to the high order flow tangency solution. On the other hand, the accuracy of the low order flow tangency solution is considerably worse.



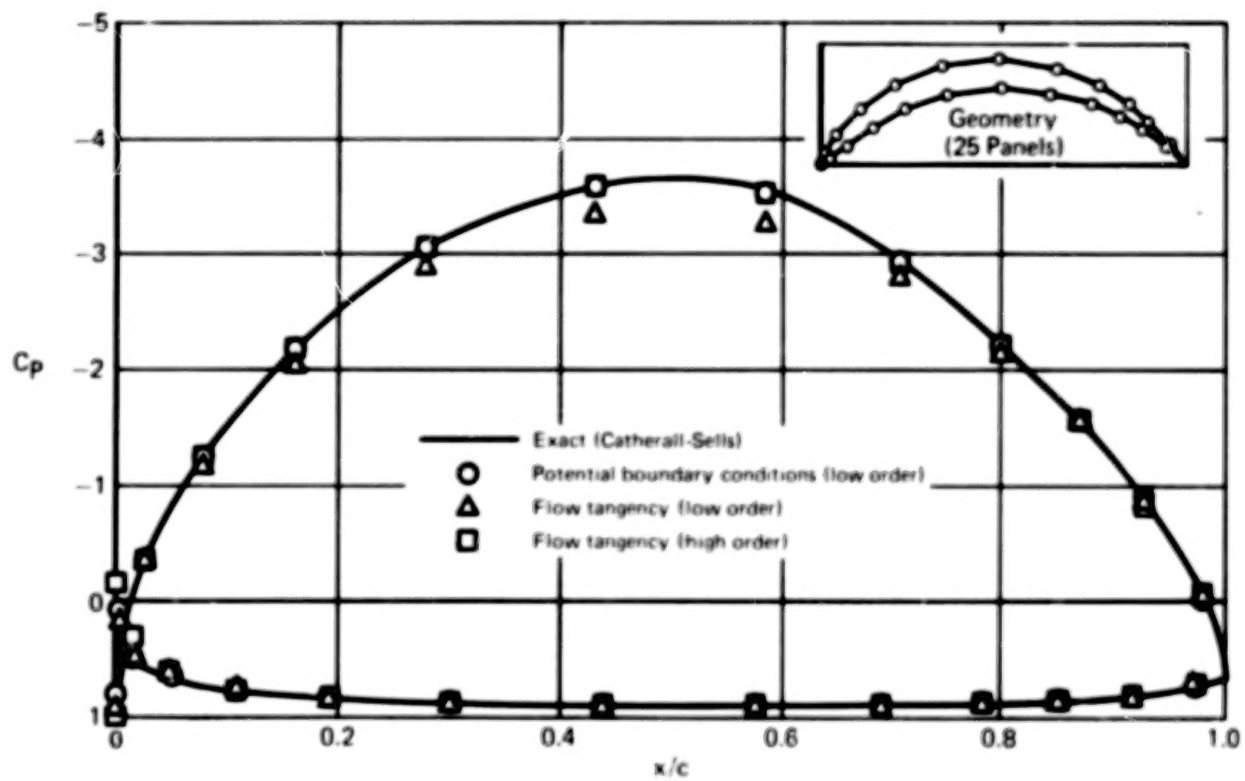


Figure 20. Karman - Trefftz Airfoil  
 $0^\circ \alpha$ ,  $3.24 C_q$ , 25 Panels

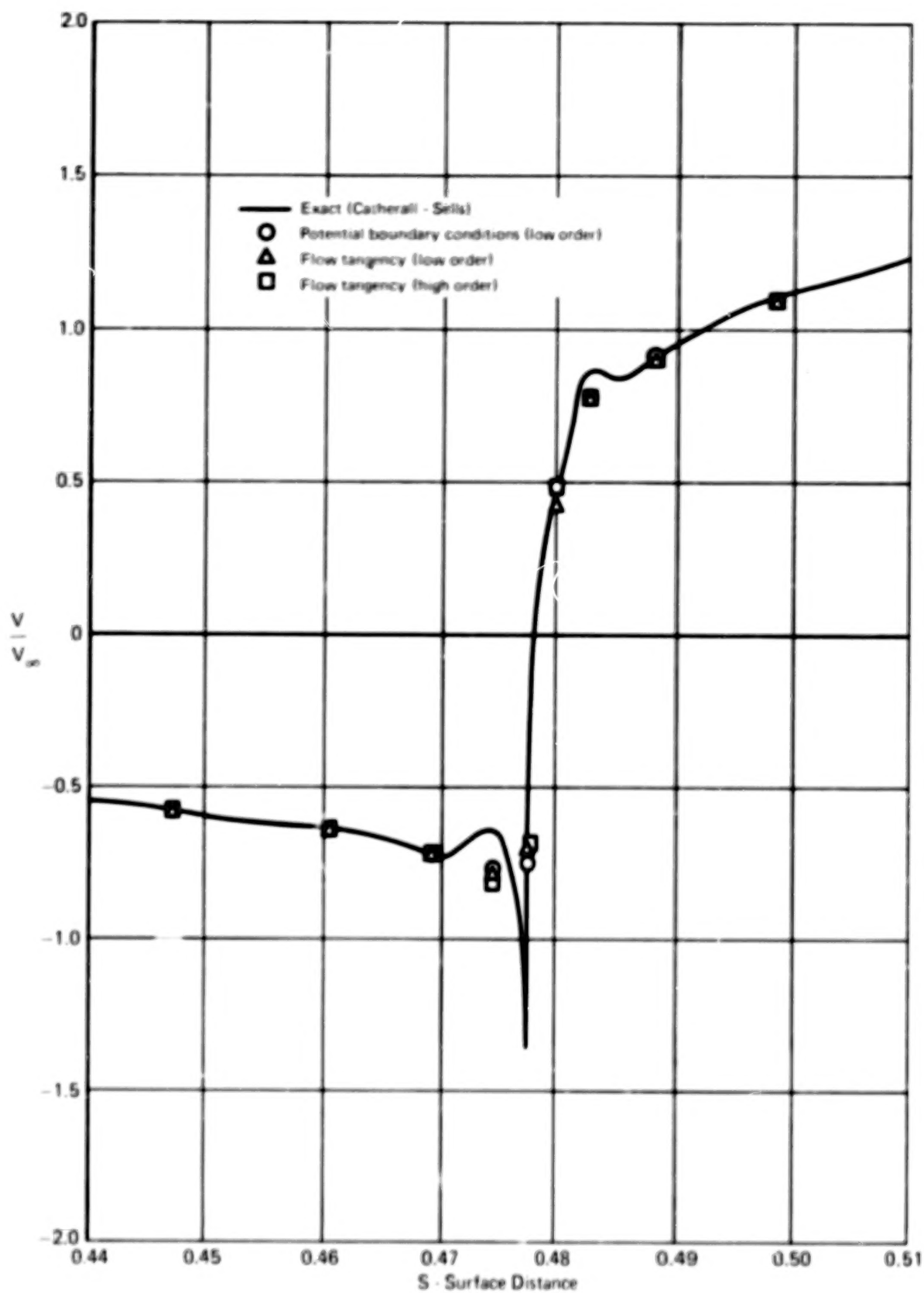


Figure 21. Karman - Trefftz Airfoil  
 $0^\circ \alpha$ ,  $3.24 C_L$ , 50 Panels

For the supercritical airfoil of Figure 22, the low order potential boundary condition method again provides excellent results. The Douglas Neumann constant source solution is also presented in the figure to illustrate the well-known thin airfoil instability associated with source solutions. To account for the lift of the supercritical airfoil, the usual approach of adding a uniform vortex density around the airfoil was implemented in the Douglas Neumann method. It is noteworthy that for this example much of the error associated with the source solution could have been eliminated by replacing the uniform vortex distribution by a distribution parabolic in terms of surface distance (Reference 22). For certain geometries, the parabolic distribution allows weaker source strengths and therefore improves the prediction accuracy.

In order to determine sensitivity to coordinate noise, the upper surface velocity distribution was calculated for the non-lifting nearly flat plate of Figure 23. Ideally, the smooth upper surface should be insulated from the jagged lower surface and the calculated results should agree closely with the solution for a nonlifting flat plate at  $-90^\circ$  incidence. Such is the case for all three Green's identity solutions, which are nearly identical. Again, the source solution reflects the thin airfoil instability.

The final example explores the limiting behavior of a symmetrical airfoil at zero incidence as thickness ratio approaches zero (figure 24). The perturbation velocity for the low order potential boundary condition method and for the high order flow tangency method share approximately the same average prediction error, which is much less than the error from the low order flow tangency solution (figure 25). As a function of panel density, the vortex density at 50% chord for all three methods approaches the analytical linearized theory value as panel density increases (figure 26). However, only the vorticity from potential boundary conditions exhibits good accuracy.

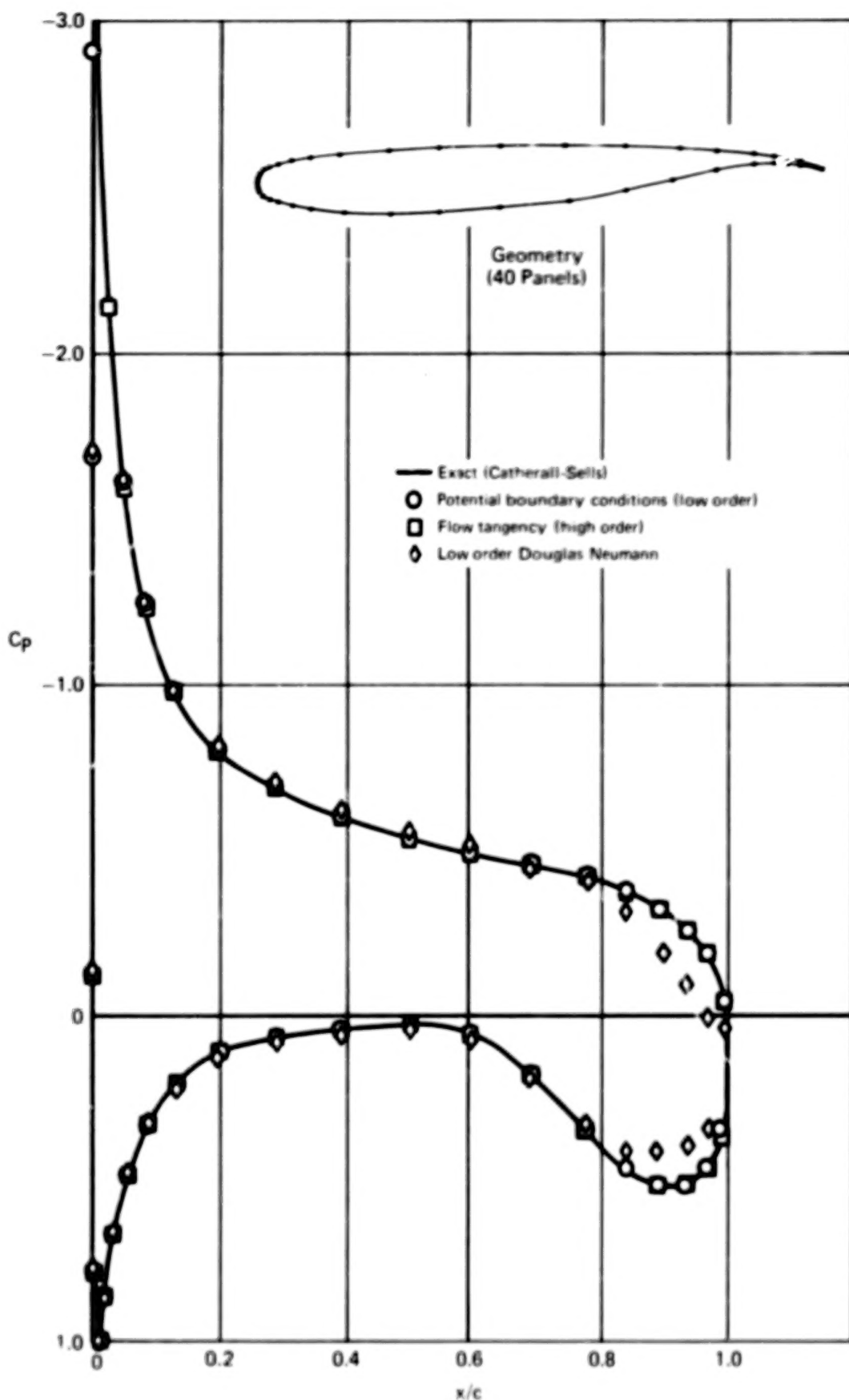


Figure 22. Supercritical Airfoil  
( $4^\circ \alpha$ ,  $0.905 C_L$ )

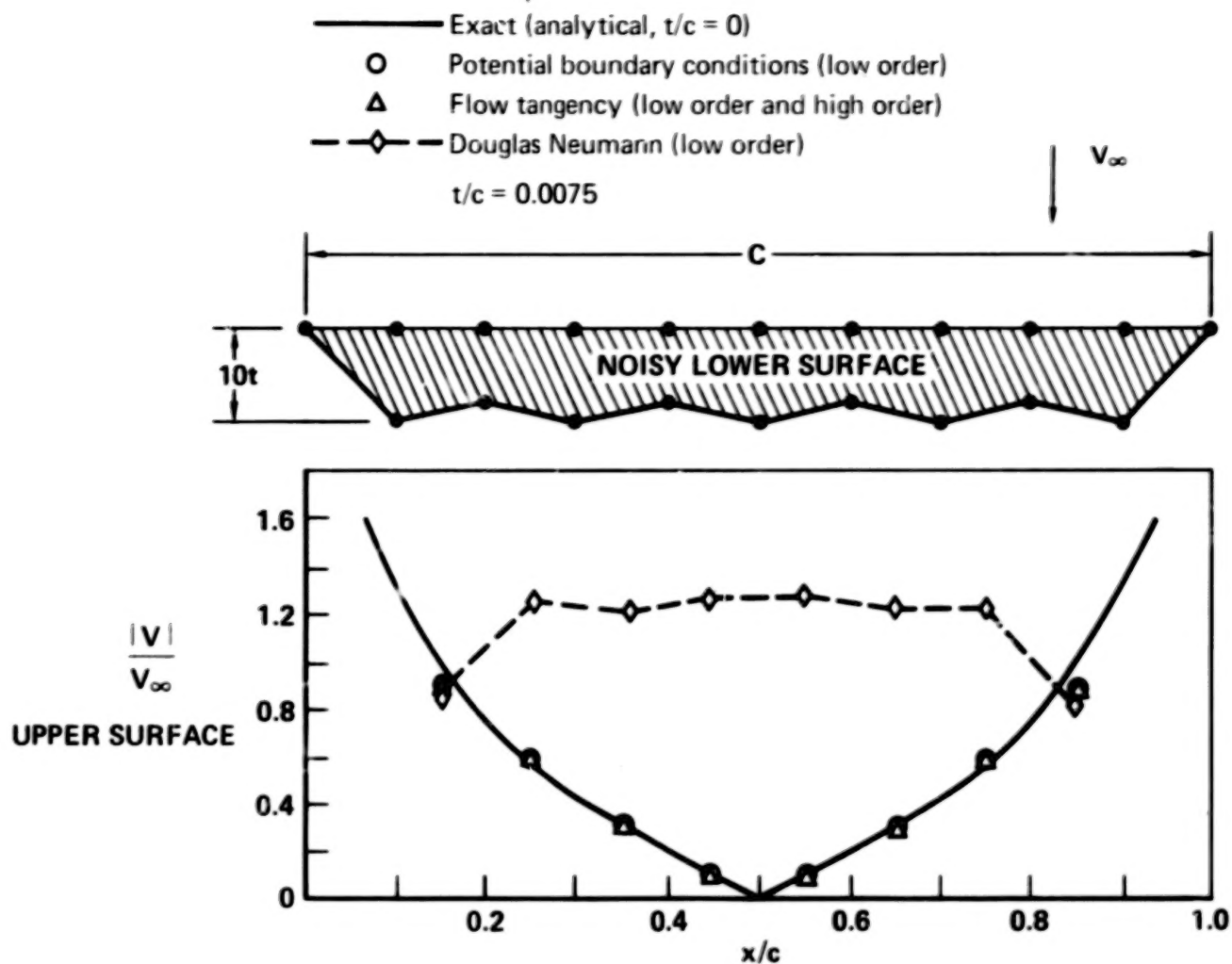


Figure 23. Noisy Flat Plate at  $-90^\circ$  Incidence  
( $C_L = 0$ )

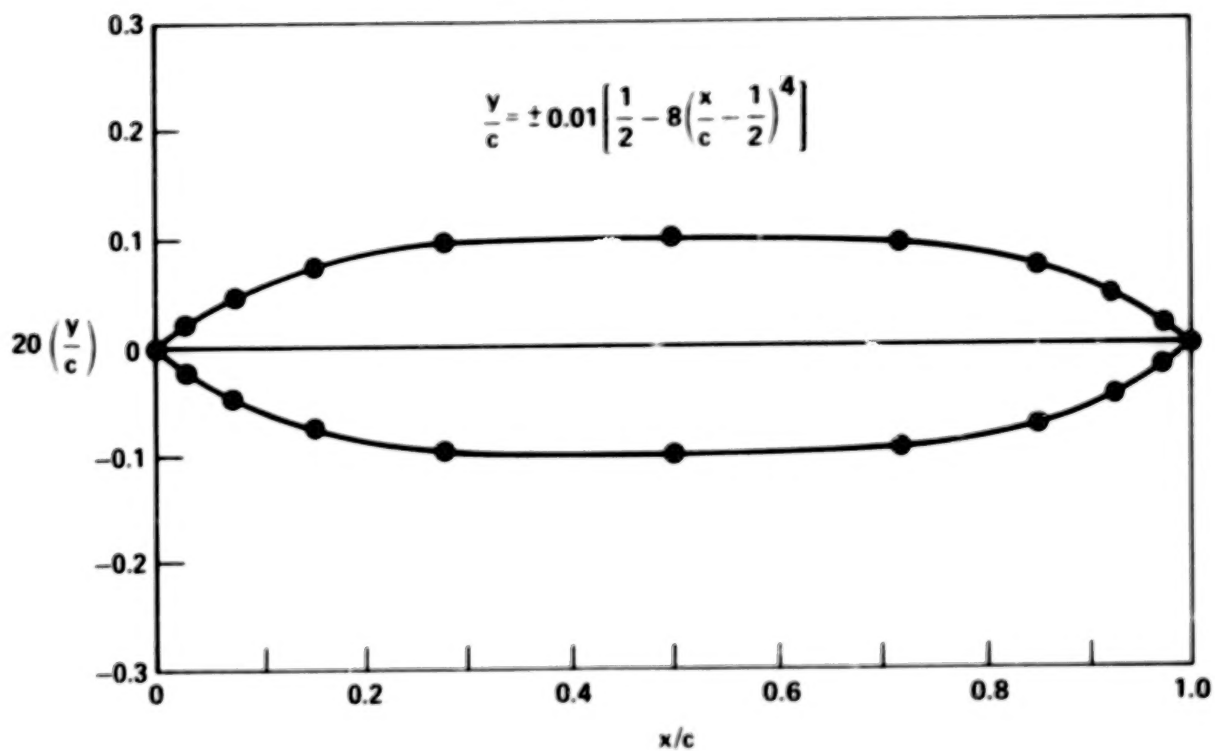


Figure 24. Thin Symmetrical Airfoil Geometry  
(20 Panels)

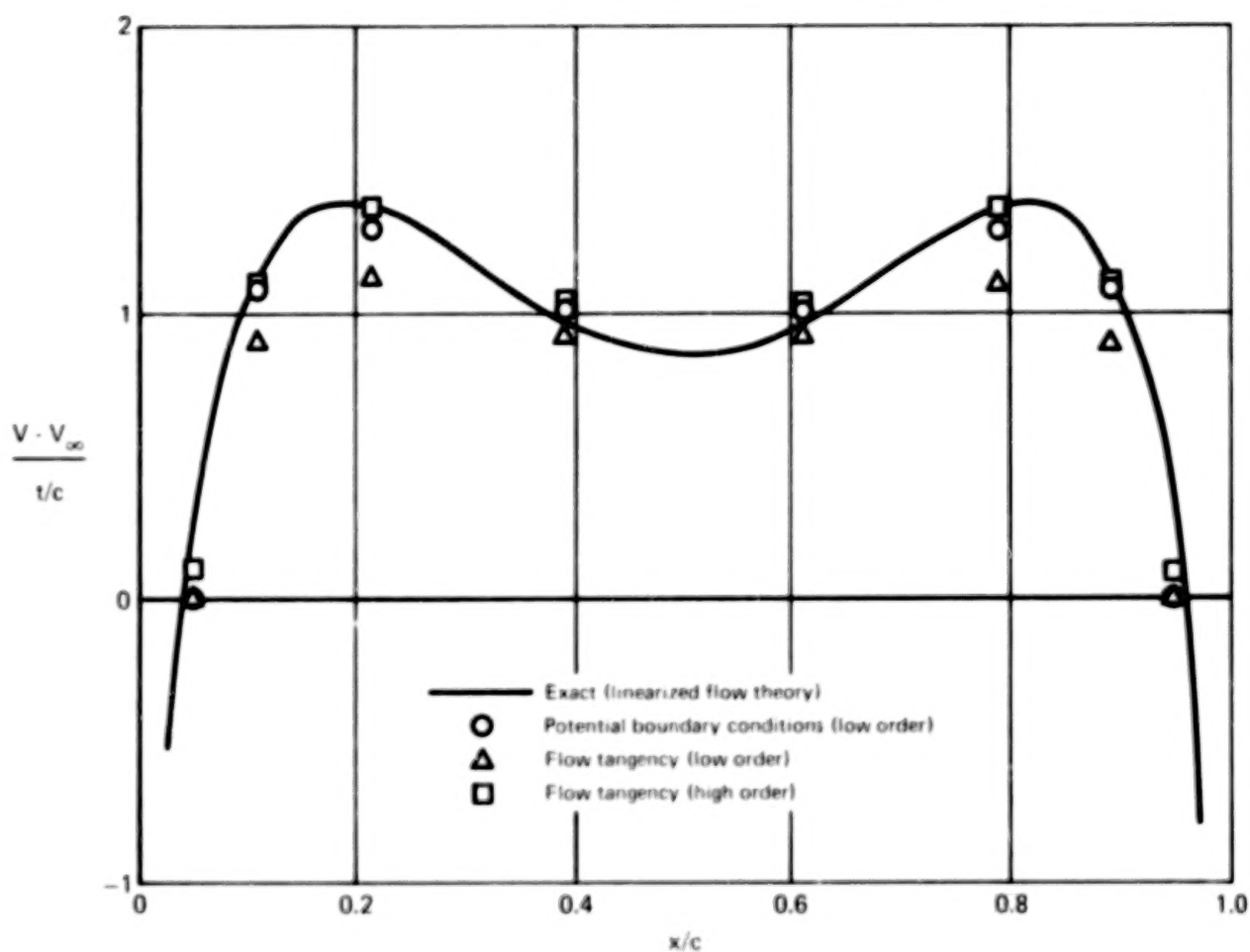


Figure 25. Thin Symmetrical Airfoil at Zero Incidence

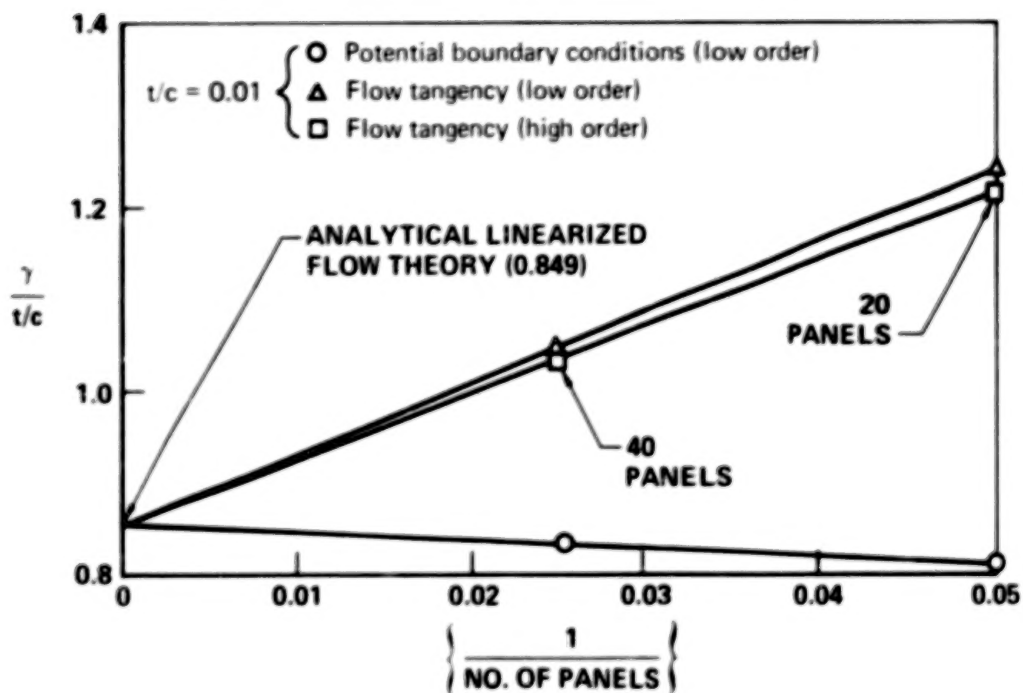


Figure 26. Thin Symmetrical Airfoil Vorticity at 50% Chord



From the above examples, one reaches the heretofore unexpected conclusion that, even in a low order formulation, the application of internal potential boundary conditions provides prediction accuracy that is in most practical cases equivalent to a higher order formulation. This applies only to the velocity calculated by equation (20); velocity calculated by summing the product of velocity influence coefficients and singularity density is significantly less accurate. The preliminary explanation is that the increment in potential between adjacent control points is nearly independent of both source gradient and surface curvature effects for a wide range of geometric shapes. Therefore, the prospect exists for obtaining higher order prediction accuracy without the additional complexity of calculating higher order corrections to the influence coefficients.

#### Accuracy of Concave Corner Solutions

On typical aircraft configurations, the intersection of the wing and fuselage generates a sharp concave corner in the cross-flow plane. The existing Douglas Neumann surface source method predicts a velocity distribution that increases without bounds as the corner is approached, rather than the finite velocity limit corresponding to the correct inviscid flow tangency solution. This characteristic of the Douglas Neumann method is discussed by Hess in reference 23 for the special case of two-dimensional flow.

In order to ascertain whether implementation of Green's identity offers the prospect of improving prediction accuracy near sharp concave corners, an investigation was conducted for the simple two-dimensional geometry of figure 27. This geometry was initially used by Hess in his study of source method prediction characteristics. He compared the numerical and exact analytical solutions near the concave corner at  $S = 0$ . The present study repeats his procedure with the inclusion of predictions by the higher order Green's identity panel method using flow tangency boundary conditions.

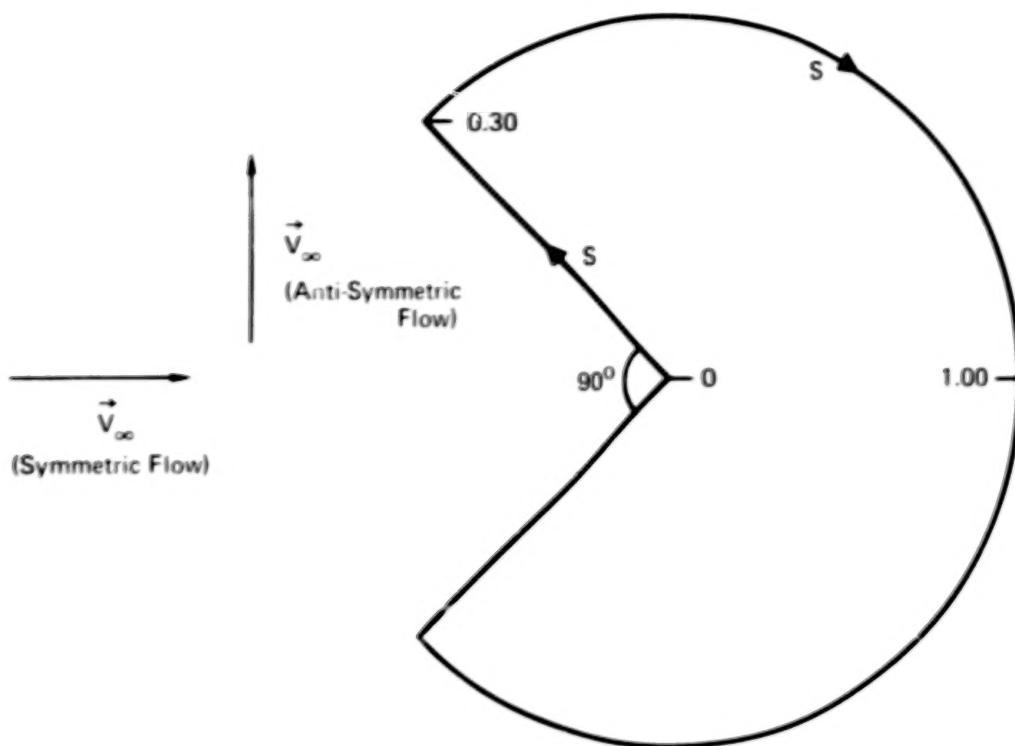


Figure 27. Simple Geometry with a Concave Corner

Hess provided the solutions from his low order Douglas Neumann source method. The geometry of figure 27 modeled by Hess incorporates 56 equal length panels between  $S = 0$  and 0.30 and 66 equal length panels between  $S = 0.30$  and 1.00. Identical paneling was used on the lower half of the geometry. For the Green's identity panel method, we used essentially the same panel distribution, but only one-half the panel density in order to avoid increasing the dimension limits of the program.

Both the symmetric ( $0^\circ \alpha$ ) and anti-symmetric ( $90^\circ \alpha$ ) solutions were investigated. At any intermediate angle of attack, the solution is simply a linear combination of these two solutions. In the vicinity of a concave corner, Hess states that the exact velocity varies as  $V \sim S^3$  for symmetric flow and  $V \sim S$  for anti-symmetric flow.

The calculated velocity distribution for symmetric flow is presented in figure 28 as a function of surface distance  $S$ . The Douglas Neumann and Green's identity solutions are virtually identical except near the concave corner, where the former blows

up. On the other hand, the Green's identity solution is seen to approach stagnation at the corner, as does the exact analytical solution. The detailed behavior of the Green's identity solution very near the corner is evident in figure 29, where velocity has been plotted versus surface distance on a log-log scale. Notice that the numerical solution agrees well with the exact solution ( $V \sim S^3$ ) except within two panel lengths of the corner, where the velocity error is approximately  $0.001 V_\infty$ . This error is insignificant and would not be noticeable if a logarithmic scale were not used.

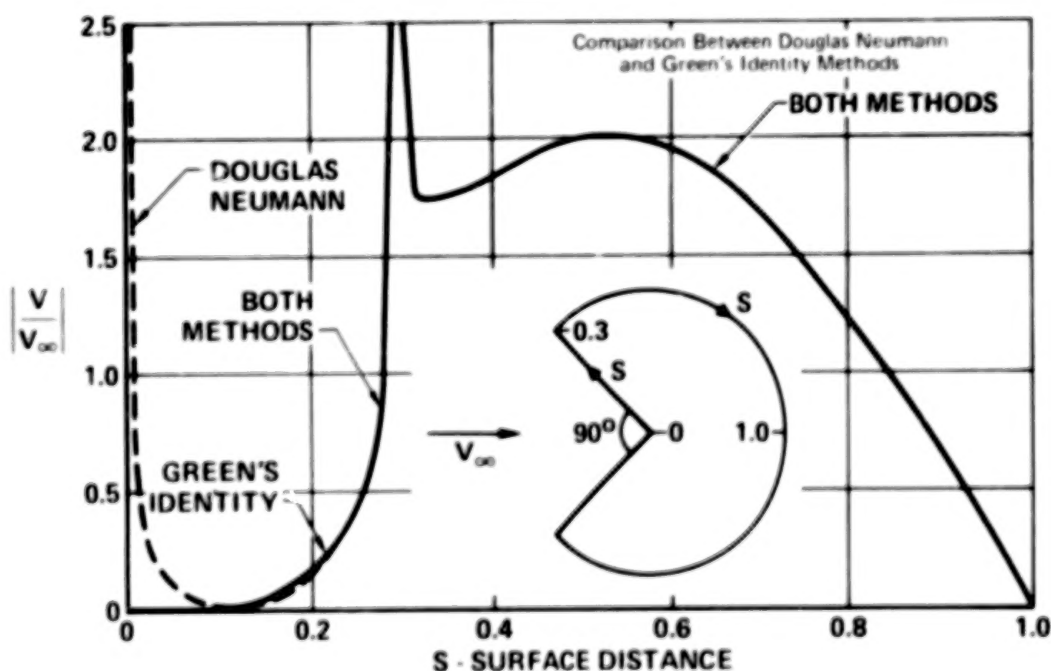
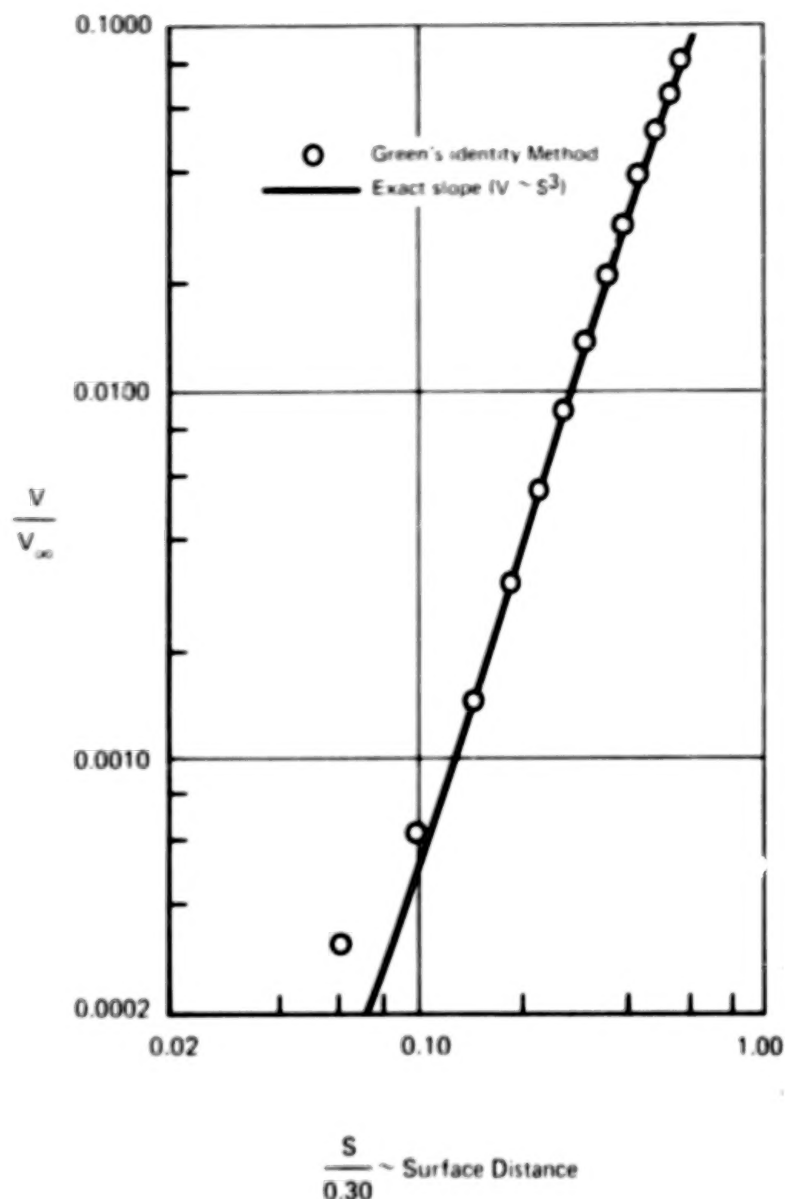
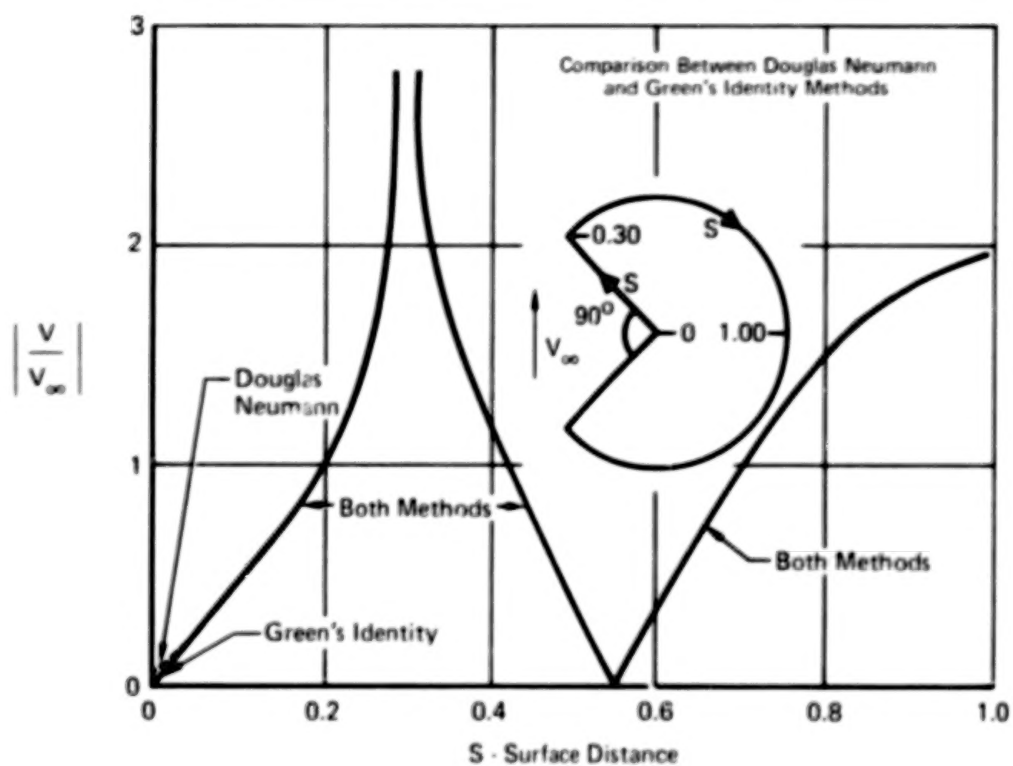


Figure 28. Calculated Velocity Distribution for Symmetric Flow



**Figure 29. Velocity Distribution Near A Concave Corner**  
(Symmetric Flow)

Similar graphs for anti-symmetric flow are presented in figures 30 and 31. Here the discrepancy between the two methods is much smaller, although the Green's identity approach still provides a significantly better velocity distribution near the concave corner.



**Figure 30. Calculated Velocity Distribution for Anti-Symmetric Flow**

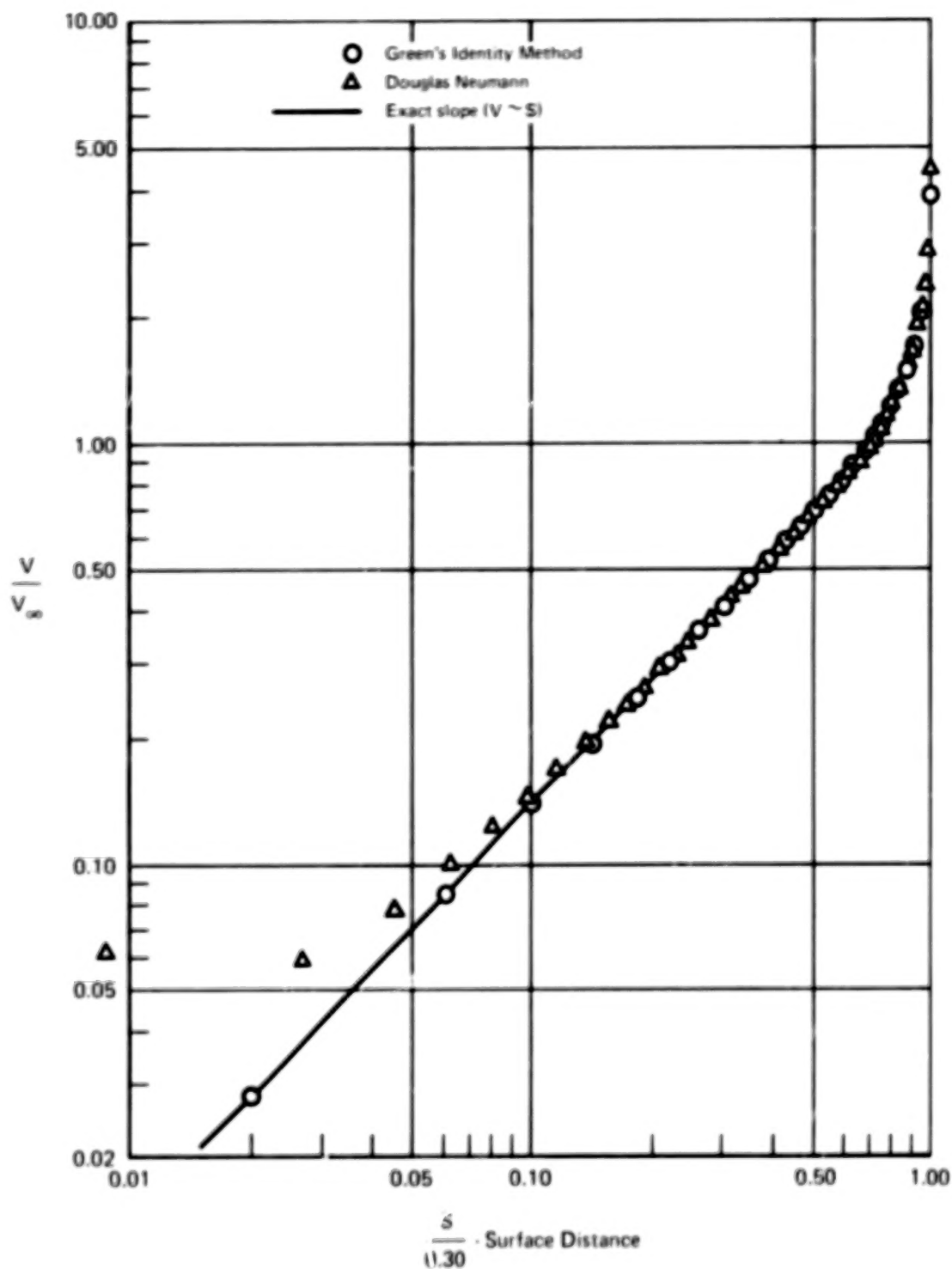


**Figure 31. Velocity Distribution Near a Concave Corner  
(Anti-Symmetric Flow)**

The concave corner example was repeated for the low order internal potential approach, and the results are similar to the solution for the higher order flow tangency Green's identity formulation.

It is concluded that for two-dimensional flow, Green's identity provides an improved flow model in the vicinity of a concave corner when compared to the Douglas Neumann solution. It is expected that this benefit will carry over to the wing-fuselage intersection region in the modeling of an aircraft.

#### Inverse (Design) Capability

The approach of reference 17 was used to formulate the complete partial derivative distribution of surface velocity with respect to surface geometry, for the low order, internal potential boundary condition formulation of Green's identity. Then, by prescribing an arbitrary change in surface velocity distribution, the program determines the corresponding first order change in geometry by solving a system of linear equations. By iteration, the program designs the multielement airfoil geometry having a specified velocity distribution on one or more elements. For each element to be designed in a multi-element airfoil system (up to five elements), the following steps are involved:

- (1) The user prescribes a design pressure or velocity distribution around the surfaces of one or more of the various airfoil elements. The geometry of the remaining elements will be fixed.
- (2) The user prescribes a starting geometry to initialize the calculations and the location of one point on each element to be fixed in space, such as the trailing edge.
- (3) The program solves the direct problem for the starting geometry in order to determine the change in velocity distribution required to achieve the prescribed values.
- (4) The program calculates the rate of change of surface velocity with respect to an arbitrary change in surface angle distribution. The element perimeter remains

fixed. If the tangential component of velocity at the control point of the  $i^{\text{th}}$  panel is designated  $V_{Ti}$ , and if the surface angle of the  $j^{\text{th}}$  panel is designated  $\theta_j$ , then the array  $A_{ij}$  is calculated where

$$A_{ij} = \frac{\partial V_{Ti}}{\partial \theta_j} \quad (23)$$

- (5) The change of surface angle distribution is calculated in accordance with the prescribed velocities and the following first order expression.

$$\Delta V_{Ti} \approx \sum_j (A_{ij} \Delta \theta_j) \quad (24)$$

- (6) The geometry is corrected by the program, and steps (3) - (5) are repeated as a series of iteration cycles.

The most difficult and important step in formulating the inverse capability is to generate the matrix  $A_{ij}$ . It is noted that all terms were incorporated in deriving the partial derivative, including singularity strength changes and the displacement of panels  $j+1$ ,  $j+2$ , etc. corresponding to the surface angle change  $\Delta \theta_j$ . The corresponding singularity strength changes are obtained by a first order expansion to the boundary condition equation.

A typical inverse solution requires five iteration cycles, where each cycle requires approximately four times the computing time of a direct problem solution. On the CBC CYBER 173, a typical two-element airfoil inverse problem with seventy panels uses 20 seconds computing time per cycle. This compares with 150 seconds per cycle for the earlier least squares method (reference 17).

Two examples are discussed herein to illustrate inverse problem solution convergence characteristics.

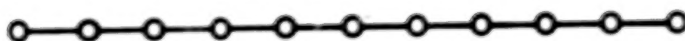


The objective of the first example is to design a circular cylinder by using a nearly flat plate for the starting geometry (Figure 32). The exact analytical surface velocity distribution was prescribed, and the converged solution geometry of figure 32 was obtained after four iteration cycles. The panel endpoints are within a maximum distance of  $0.002 \times$  radius of lying on a circle. The complete partial derivatives of velocity with respect to surface angle change are necessary but not sufficient for obtaining convergence about the periphery of this example. The use of mild combined source-vortex singularities is also a factor. To illustrate, the example was repeated, but this time only vortex singularities were used to induce the flow field, in accordance with the analysis method of Woodward-Dvorak (reference 11). The geometry never converged (figure 15) but oscillated  $\pm 30^\circ$  in the leading edge region from one iteration cycle to the next.

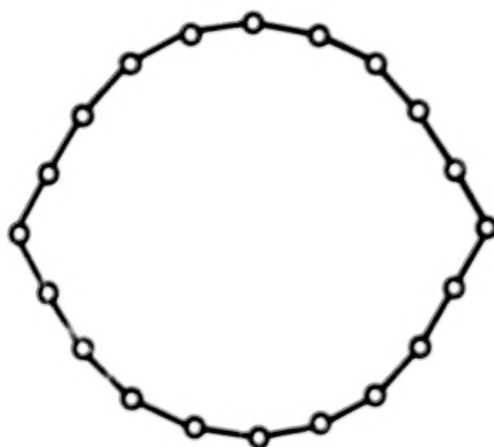
The second example demonstrates the inverse solution for the two-element Williams airfoil presented earlier in figure 16. The simple starting geometry shown in figure 33 was used to initialize the calculations, and the exact surface velocity distribution of Williams was prescribed on both elements. The geometry converged and agreed with the target geometry to within a tolerance of one-tenth of one degree surface angle on all panels in five iterations.

This approach to the design problem is suitable for extension to 3-D. The 2-D inverse method based on the Green's identity formulation has demonstrated low cost combined with consistent accuracy and stability. The low calculation cost will be even more important in a 3-D method. The effort of developing a 3-D method is reduced since the modified 3-D analysis program uses the same low-order singularities and internal potential boundary conditions as the 2-D inverse method. The modified 3-D program can be used directly for the analysis steps. The inverse capability would play an obvious role in future high-lift device design, and would also be valuable in analyzing flow fields with strong viscous-inviscid interactions.

Starting Geometry



After 2  
Iterations



After 4  
Iterations  
(Converged)

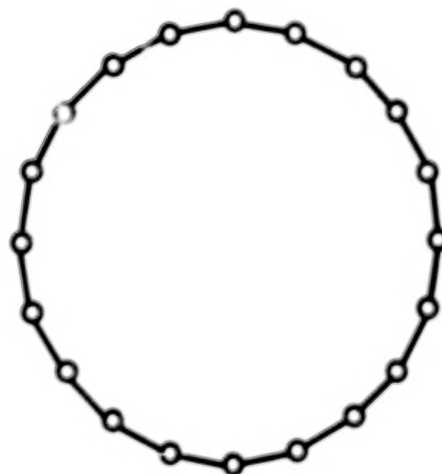


**Figure 32. Circular Cylinder Inverse Solution  
(MCAIR Method)**

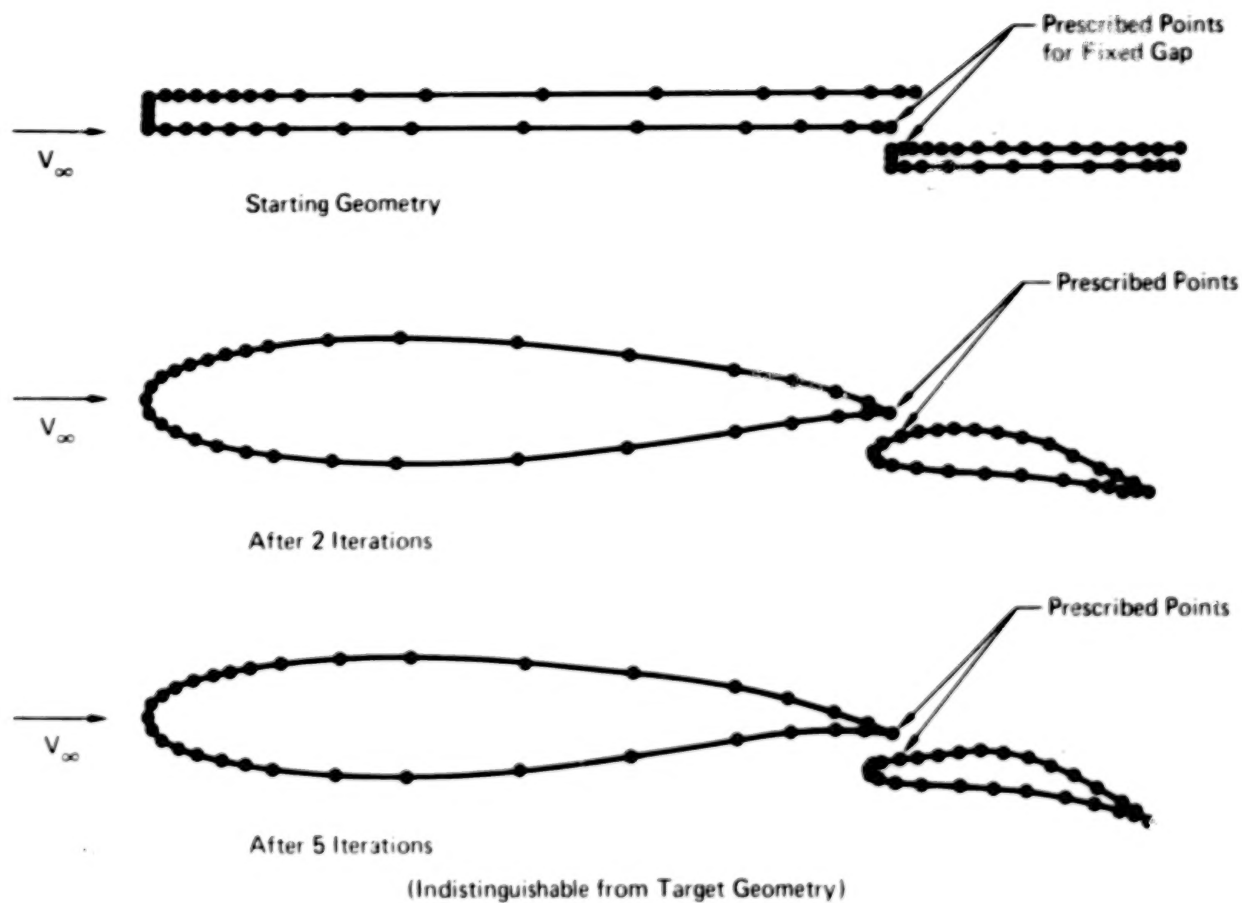


**Figure 33. Two-Element Airfoil Inverse Solution**

### Selected Formulation

Overall, the research into two-dimensional panel method formulations indicates that only through the application of the combined source-doublet distribution of Green's identity will one consistently obtain numerically stable calculations in both analysis and design modes without any significant increase in computational expense compared to either a source or doublet only formulation. With higher order corrections, flow tangency boundary conditions consistently provide accurate predictions. Competitive accuracy can be obtained for a wide range of shapes without such corrections if internal potential boundary conditions are applied.

For initial development of a 3-D Douglas Neumann Program modification, the internal potential boundary condition formulation has the advantage of using the low-order source panel singularities already in the program, while the flow tangency boundary condition approach would require the additional effort of incorporating the high-order, curved panel singularities still under development by Douglas Aircraft Company. The internal potential method is also a consistent analysis method for extending the 2-D inverse method to a 3-D capability. Therefore, the internal potential formulation was selected for the 3-D program modification.

## NUMERICAL SOLUTION FORMULATION

The formulation is presented as a modification to the existing Douglas Neumann Program (reference 2) to improve the efficiency and reliability of predicting component interference and high lift characteristics of wing-body configurations. The primary modification is the substitution of the mild combined source-doublet distribution of Green's identity for the fundamental source-only distribution of the existing program. The advantages associated with combined source-doublets were explained in terms of classical theory in the section on Potential Flow Theory and were demonstrated for two-dimensional flow in the examples of the section Research on Green's Identity Formulation.

The objective is to couple contemporary numerical techniques with the classical theory in order to provide a reliable prediction tool. It is assumed that one or more bodies are immersed in a steady, incompressible, inviscid stream of velocity  $\vec{V}_\infty$ . The bodies can be either lifting or nonlifting, which means that wakes can be either included or omitted. Consistent with the existing program, the present formulation assumes solid body tangency boundary conditions. In accordance with the classical theory, it would be a simple matter to extend the formulation to allow either arbitrary normal velocity boundary conditions or Dirichlet prescribed potential distribution. The aim is to calculate flow properties at the solid body surfaces, particularly the pressure, which is integrated to provide force and moment.

The selection of the modeling is dictated by the following guidelines:

1. If the body geometry approaches the shape of an infinite aspect ratio wing with uniform cross-section, then the numerical doublet model should reflect the piecewise linear vortex representation employed by the two-dimensional Green's identity panel method of the preceding section.

Experience in solving two-dimensional problems demonstrates that such a vortex model provides good accuracy and numerical stability, and it would be unfortunate to

sacrifice such characteristics in the three-dimensional formulation.

2. The doublet distribution model should be as nearly continuous as possible. Discontinuities in doublet density correspond to concentrated vortex filaments which counteract the mild velocity gradients associated with distributed surface singularity methods.
3. The entire doublet distribution should be described by a set of scalar parameters with approximately the same number of members as there are panels. These parameters are the basic unknowns to be determined. Determination of additional parameters could lead to excessively large computational expense, since computing time varies as the third power of the number of unknowns.

There are four basic steps in the solution process, (1) geometry definition, (2) influence function calculation, (3) solution to linear simultaneous boundary condition equations for the unknown singularity density distribution, and (4) calculation of surface flow properties. These steps correspond to a direct application of the theory, except that the continuous integral theoretical relationships are discretized to allow numerical solutions to arbitrarily complex problems. Prediction error is defined as the difference between the exact analytical solution and the numerical calculations. Because no small disturbance assumptions are employed, prediction errors result from the discretization process only. Therefore, one could generate arbitrarily accurate numerical predictions at the expense of the increased computing time commensurate with the introduction of additional unknowns.

The geometry definition involves replacing the actual continuous boundaries by a set of trapezoidal panels. In the existing program of Ref 2, each panel is identified by one of four categories, (1) nonlifting, (2) lifting, (3) internal lifting, and (4) wake. Nonlifting source only panels are typically distributed on fuselage-type surfaces while the lifting panels model wings and aerodynamic control surfaces. The internal lifting panels are

designed to pass through fuselages and connect the exposed wing roots in order to provide fuselage lift-carryover. In the present formulation, the combined source-doublet distribution panels allow a natural carryover of flow properties from wing to fuselage surfaces. Therefore, the first three panel categories of the existing program are replaced by the single category "body panels". In the same sense that the theory recognizes no fundamental distinction between fuselages, wings, and tails, the body panels are used to represent any solid flow boundary. As in the existing program, wake panels are used to model lifting configurations.

The continuous surface source and doublet distributions of the theory are respectively modeled by piecewise constant and piecewise quadratic distributions on the trapezoidal panels. Seven parameters describe the complete singularity density distribution on each panel. One parameter is the uniform source density. The remaining six are the coefficients of the six terms in the expression for quadratic doublet density. The potential and velocity induced at any field point by the panel singularity distribution can be expressed as the product of each of the seven parameters with its appropriate influence function. Each influence function depends solely on panel geometry and field point location and is written in closed analytical form. One influence function describes the effect of a unit strength uniform doublet distribution, another describes the effect of a unit linear doublet distribution, etc.

Of the six parameters that describe the doublet distribution on a panel, only one can be considered an independent variable reserved for boundary condition satisfaction. The remaining five are fall-outs whose values are dictated by a least squares surface fit through neighboring control points.

There is approximately one boundary condition control point allocated per panel. Because Green's identity is employed, the source density for each panel is a function of local geometry only (eq. 16). It remains to determine the doublet density. Rather than prescribing Neumann boundary conditions directly,



the theoretically equivalent zero internal perturbation potential boundary conditions are applied. In two-dimensional flow, such potential boundary conditions consistently produce very good prediction accuracy even though panel curvature and source gradient effects are neglected. Furthermore, the two-dimensional design boundary conditions for inverse problems were easy to derive when coupled with internal potential conditions and led to exceptionally rapid, stable convergence. Based on the experience that three-dimensional numerical characteristics should reflect those of two-dimensional flow, the selection of internal potential boundary conditions was made.

With the aid of the influence functions and doublet continuity considerations at panel edges, the internal potential boundary conditions are established as a system of linear equations with the doublet strength parameters as unknowns. There is essentially one unknown per panel. Solution to the system renders the complete singularity distribution known, and it is then a simple matter to calculate the net induced velocity or potential at any field point. Pressure coefficients at body control points are determined from Bernoulli's equation (6), and the resultant force and moment is determined by integration under the assumption that the pressure on each panel is uniform.

The formulation is presented in detail below.

#### Geometry Panel Modeling

All boundary surfaces are divided into continuous regions designated sections, as illustrated in figure 34. Each solid body in the flow can be described by one or more sections, and the division is at the prerogative of the user. For example, a section could be the upper surface of a wing, a fuselage, or both the fuselage and wing simultaneously. The only restriction is that a single section must contain either body regions or wake regions exclusively and not both simultaneously. This deviates from the original program but provides a more consistent formulation. It is assumed that all body slopes within a section are continuous; therefore, section edges should be aligned with



any slope discontinuities such as wing trailing edges and wing-fuselage junctures.

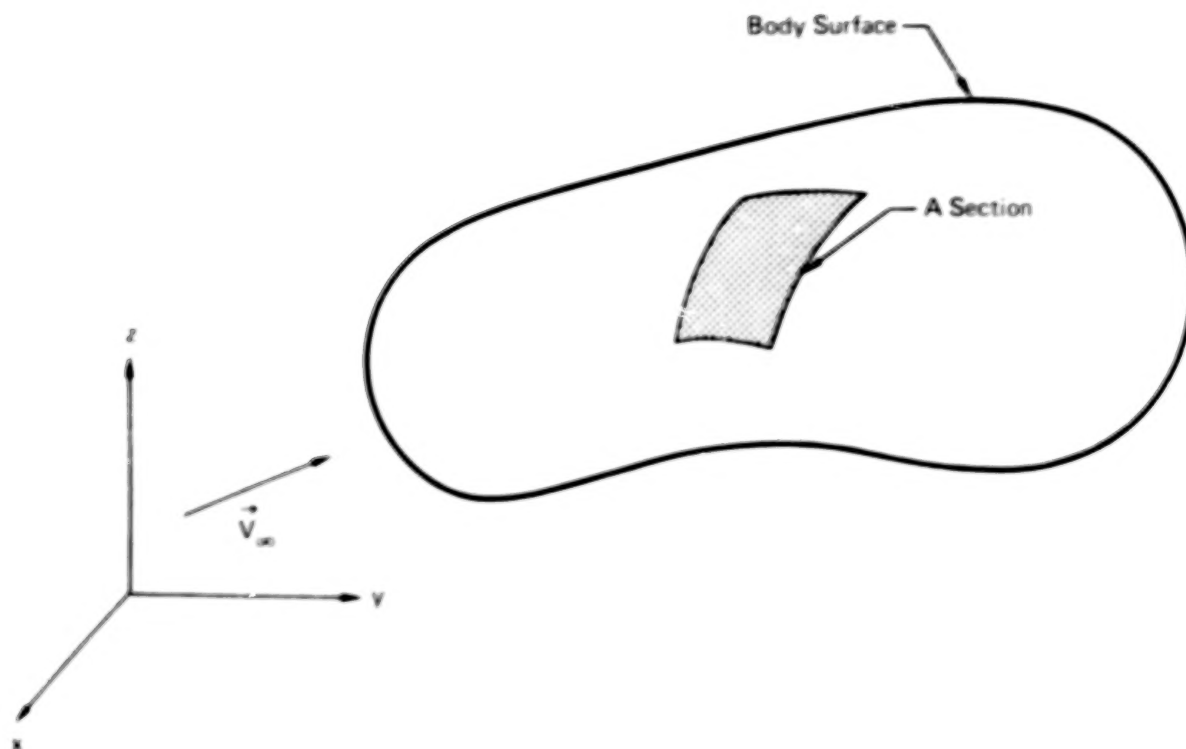


**Figure 34. A Section of a Body Surface**

Each section is subdivided into panels in the same manner employed by the existing Douglas Neumann Program. The section is described by a total of  $N \times M$  points, where each point is identified by the pair of indices  $i$  and  $j$  ( $1 \leq i \leq N$ ,  $1 \leq j \leq M$ ). See figure 35. The points describe a set of  $(N - 1) \times (M - 1)$  panels, where each panel is identified by the pair of indices  $i_p$  and  $j_p$  ( $1 \leq i_p \leq N-1$ ;  $1 \leq j_p \leq M-1$ ). See figure 36. Panel  $(i_p, j_p)$  is defined by the four corner points  $(i_p, j_p)$ ,  $(i_p, j_p+1)$ ,  $(i_p+1, j_p+1)$ , and  $(i_p+1, j_p)$ . The order of sequencing is such that the positive normal direction (pointing into the fluid) is out of the plane of the paper. In other words, the positive normal direction is in the sense of the increasing  $i$ -direction crossed with the increasing  $j$ -direction. Any inertial  $(x, y, z)$  Cartesian coordinate system is satisfactory for describing the geometry. The free stream velocity  $\vec{V}_\infty$  is assumed to have unit magnitude and to be described by the following components:

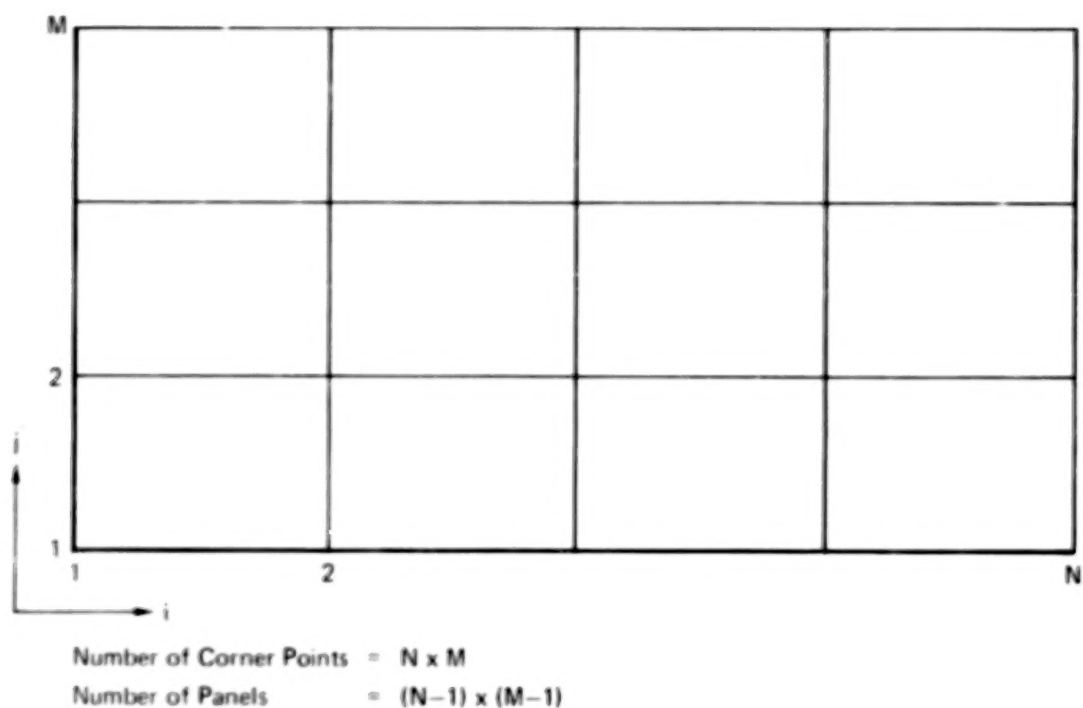


**Figure 35. Corner Point Indexing Convention for a Section**

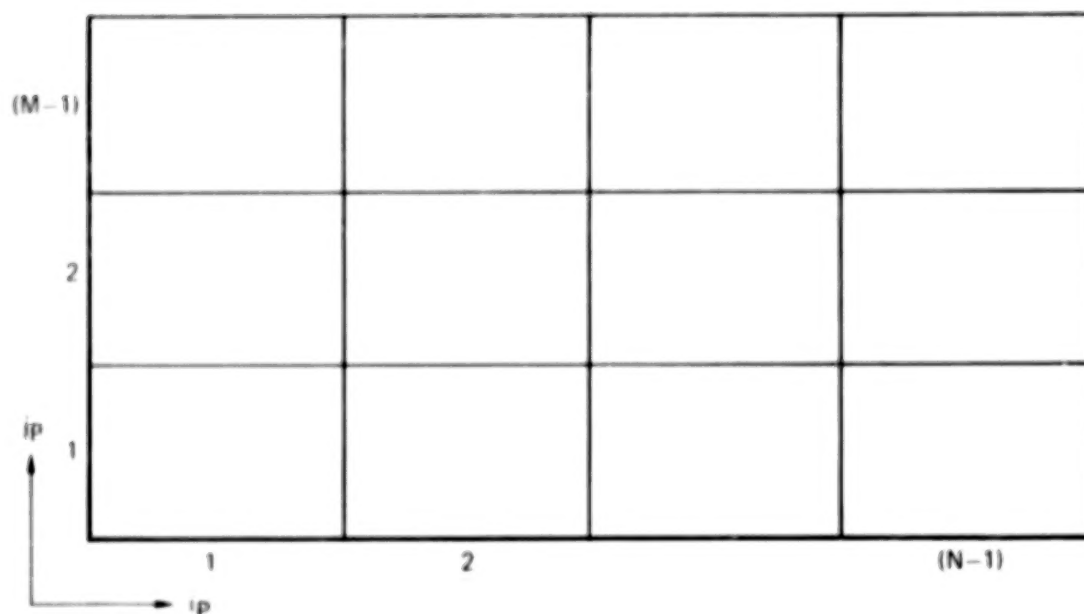


**Figure 36. Panel Indexing Convention for a Section**

$$\vec{V} = a_x \vec{e}_x + a_y \vec{e}_y + a_z \vec{e}_z \quad (25)$$

where  $\vec{e}_x$ ,  $\vec{e}_y$ ,  $\vec{e}_z$  are unit vectors in the x, y, and z - directions, respectively.

The four corner points of a panel in general describe a nonplanar quadrilateral. For compatibility with existing influence functions, adjustments to the corner points are made in order to generate the trapezoid that is most nearly described by the original four points. The procedure is identical to that of the existing program (reference 2).

Consider the arbitrary panel of figure 37. For clarity, the four corner points are identified by indices  $k = 1, 2, 3, 4$ . The adjustments to determine the trapezoidal panel involve making the line between points 1 and 2 parallel to the line between points 3 and 4. If the unadjusted coordinates of corner point  $k$  are  $(x_k, y_k, z_k)$ , then define vector  $\vec{P}_k$  as

$$\vec{P}_k = x_k \vec{e}_x + y_k \vec{e}_y + z_k \vec{e}_z \quad (1 \leq k \leq 4) \quad (26)$$

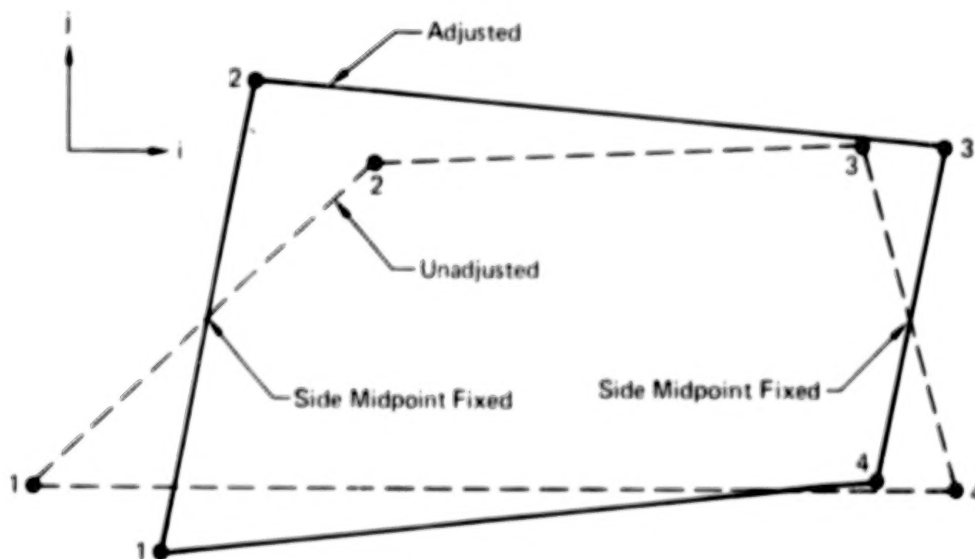


Figure 37. Adjustment of the Input Points to Form a Plane Trapezoidal Panel

and, using subscripts "F" and "S" to designate first and second, define

$$\left. \begin{aligned} \vec{P}_F &= \vec{P}_2 - \vec{P}_1 \\ \vec{P}_S &= \vec{P}_3 - \vec{P}_4 \end{aligned} \right\} (27)$$

The weighted average of  $\vec{P}_F$  and  $\vec{P}_S$  is used to define the direction of the parallel sides of the trapezoid, which is also selected as the  $\xi$ -direction of the trapezoidal panel coordinate system

$$\vec{e}_\xi = \frac{\vec{P}_F + \vec{P}_S}{|\vec{P}_F + \vec{P}_S|} \quad (28)$$

If the adjusted corner points are identified by an asterisk \*, then the following definitions are applied:

$$\left. \begin{aligned} \vec{P}_1^* &= \frac{1}{2}(\vec{P}_1 + \vec{P}_2) - \frac{1}{2}|\vec{P}_F|\vec{e}_\xi \\ \vec{P}_2^* &= \frac{1}{2}(\vec{P}_1 + \vec{P}_2) + \frac{1}{2}|\vec{P}_F|\vec{e}_\xi \\ \vec{P}_3^* &= \frac{1}{2}(\vec{P}_3 + \vec{P}_4) + \frac{1}{2}|\vec{P}_S|\vec{e}_\xi \\ \vec{P}_4^* &= \frac{1}{2}(\vec{P}_3 + \vec{P}_4) - \frac{1}{2}|\vec{P}_S|\vec{e}_\xi \end{aligned} \right\} (29)$$

It is noteworthy that the midpoints and lengths of line segments 1-2 and 3-4 remain unchanged after the adjustment.

The normal direction is defined as the direction of the  $\zeta$ -axis of the panel coordinate system

$$\vec{e}_\zeta = \frac{(\vec{P}_4^* - \vec{P}_2^*) \times (\vec{P}_3^* - \vec{P}_1^*)}{|(\vec{P}_4^* - \vec{P}_2^*) \times (\vec{P}_3^* - \vec{P}_1^*)|} \quad (30)$$

The third Cartesian coordinate of the panel system is designated  $\eta$  and is assigned the unit vector  $\vec{e}_\eta$  where

$$\vec{e}_\eta = \vec{e}_\zeta \times \vec{e}_\xi \quad (31)$$

A 3 x 3 transformation matrix  $a_{ij}$  is generated from the above definitions such that

$$(\vec{e}_\xi, \vec{e}_\eta, \vec{e}_\zeta) = [a_{ij}] \begin{pmatrix} \vec{e}_x \\ \vec{e}_y \\ \vec{e}_z \end{pmatrix} \quad (32)$$

The centroid of the trapezoid is taken as the origin of the panel coordinate system  $(\xi, \eta, \zeta)$ . See figure 38.

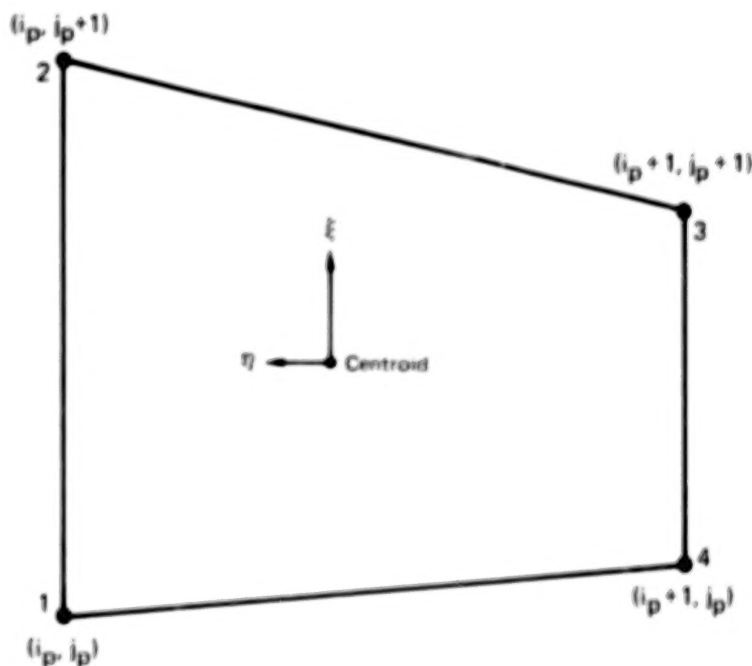


Figure 38. Panel Coordinate System  $(\xi, \eta)$

Several important geometric parameters associated with each trapezoidal panel such as area, maximum diagonal, etc., are calculated for future reference. These are described in detail in reference 2 and are not repeated here.

### Panel Singularity Distribution

The theoretical singularity distribution on the actual boundary surface is modeled by a uniform source density and quadratically varying doublet density on each trapezoidal panel. As part of this contractual effort, John Hess of Douglas Aircraft Company furnished a computer program code to calculate both the velocity and potential induced at any specified field point by a uniform source density and arbitrary quadratic doublet density distribution on an arbitrary trapezoidal panel. In order to generate reasonable doublet continuity modeling at panel edges, an approach developed by Boeing (reference 16) has been applied. This approach establishes linear relationships between the coefficients of the quadratic doublet distribution on each panel with the coefficients on the adjacent eight panels. An alternate approach which is believed to provide better continuity properties at the expense of slightly increased computing effort has been formulated as part of the contractual study, but has not yet been coded for a computer. These developments are discussed below.

Influence Function Formulas - Consider a trapezoidal panel with the geometry of figure 38. The uniform source density is  $\sigma$  and the quadratic doublet distribution  $\mu(\xi, \eta)$  on the panel is described as follows:

$$\mu = \mu_{00} + \mu_{10}\xi + \mu_{01}\eta + \mu_{20}\xi^2 + \mu_{11}\xi\eta + \mu_{02}\eta^2 \quad (33)$$

where the coefficients  $\mu_{00}, \dots, \mu_{02}$  are arbitrary. The formulas furnished by Hess provide the induced potential and velocity at an arbitrary field point  $(\xi_0, \eta_0, \zeta_0)$ . In Hess' formulas, the coordinates  $(\xi_0, \eta_0, \zeta_0)$  are designated  $(x, y, z)$ . It is important to interpret the coordinates as being in the panel system,  $(\xi, \eta, \zeta)$ . The term  $\phi_s$  is defined as the potential induced by a uniform source density of unit strength, while  $\phi_{mn}$  refers to the potential induced by the doublet density distribution  $\mu(\xi, \eta) = \xi^m \eta^n$ . Then the potential  $\phi$  induced by all the singularities on the panel is expressed as follows:

$$\phi = \sigma \phi_S + \mu_{00} \phi_{00} + \mu_{10} \phi_{10} + \mu_{01} \phi_{01} + \mu_{20} \phi_{20} + \mu_{11} \phi_{11} + \mu_{02} \phi_{02} \quad (34)$$

The velocity is generated by taking the gradient of  $\phi$  with respect to  $(\xi_0, \eta_0, \zeta_0)$ , i.e., with respect to  $(x, y, z)$  in Hess' formulas.

$$\begin{aligned} \vec{V} &= \frac{\partial \phi}{\partial \xi_0} \vec{e}_\xi + \frac{\partial \phi}{\partial \eta_0} \vec{e}_\eta + \frac{\partial \phi}{\partial \zeta_0} \vec{e}_\zeta \\ \frac{\partial \phi}{\partial \xi_0} &\equiv \frac{\partial \phi}{\partial x} = \sigma \frac{\partial \phi_S}{\partial x} + \mu_{00} \frac{\partial \phi_{00}}{\partial x} + \mu_{10} \frac{\partial \phi_{10}}{\partial x} + \mu_{01} \frac{\partial \phi_{01}}{\partial x} \\ &\quad + \mu_{20} \frac{\partial \phi_{20}}{\partial x} + \mu_{11} \frac{\partial \phi_{11}}{\partial x} + \mu_{02} \frac{\partial \phi_{02}}{\partial x} \end{aligned} \quad (35)$$

Analogous expressions exist for  $\frac{\partial \phi}{\partial \eta_0}$  and  $\frac{\partial \phi}{\partial \zeta_0}$ .

The required influence functions are  $\phi_S, \phi_{00}, \dots, \phi_{02}$ ,

$\frac{\partial \phi_S}{\partial x}, \frac{\partial \phi_{00}}{\partial x}, \dots, \frac{\partial \phi_{02}}{\partial z}$ . Each of these twenty-eight functions

depend solely on the coordinates of the field point and the four corner point coordinates of the trapezoidal panel  $(\xi_1, \eta_1), (\xi_2, \eta_2), (\xi_3, \eta_3), (\xi_4, \eta_4)$ . Some of the functions are provided in reference (2), along with intermediary functions of the four corner points. Using the same definitions from pages 77-84 of reference (2), the remaining influence functions are presented below. It is important to realize that Hess' definitions of potential and velocity influence functions differ from those of this report by the factors  $-4\pi$  and  $+4\pi$ , respectively. To avoid confusion, Hess' formulas will be designated by an asterisk, where

$$\phi^* \equiv -4\pi \phi$$

$$V^* \equiv +4\pi V$$

$$\begin{aligned}
\phi_S^* &= -z V_z^* \text{ (source)} \\
&+ (y - \eta_1) L^{(12)} + \frac{(x - \xi_2) - m_{32}(y - \eta_2)}{\sqrt{1 + m_{32}^2}} L^{(23)} \\
&- (y - \eta_3) L^{(34)} - \frac{(x - \xi_4) - m_{41}(y - \eta_4)}{\sqrt{1 + m_{41}^2}} L^{(41)}
\end{aligned} \tag{36}$$

$$\begin{aligned}
\frac{\partial \phi_S^*}{\partial x} &= \frac{1}{\sqrt{1 + m_{32}^2}} L^{(23)} - \frac{1}{\sqrt{1 + m_{41}^2}} L^{(41)} \\
&= -V_x^* \text{ (source)} \\
\frac{\partial \phi_S^*}{\partial y} &= L^{(12)} - L^{(34)} - \frac{m_{32}}{\sqrt{1 + m_{32}^2}} L^{(23)} + \frac{m_{41}}{\sqrt{1 + m_{41}^2}} L^{(41)} \\
&= -V_y^* \text{ (source)} \\
\frac{\partial \phi_S^*}{\partial z} &= T_2^{(32)} - T_3^{(32)} - T_1^{(41)} + T_4^{(41)} \\
&= -V_z^* \text{ (source)}
\end{aligned} \tag{37}$$

$$\begin{aligned}
\phi_{00}^* &= V_z^* \text{ (source)} \\
\phi_{01}^* &= -zV_y^* \text{ (source)} + yV_z^* \text{ (source)} \\
\phi_{10}^* &= -zV_x^* \text{ (source)} + xV_z^* \text{ (source)} \\
\phi_{02}^* &= zJ_{02} + 2y\phi_{01}^* - y^2\phi_{00}^* \\
\phi_{11}^* &= zJ_{11} + x\phi_{01}^* + y\phi_{10}^* - xy\phi_{00}^* \\
\phi_{20}^* &= zJ_{20} + 2x\phi_{10}^* - x^2\phi_{00}^*
\end{aligned} \tag{38}$$



$$J_{20} = \phi_s^* - H_{02} \quad (39)$$

$$\left. \begin{aligned} \frac{\partial J_{20}}{\partial x} &= -v_x^* \text{ (source)} - \frac{\partial H_{02}}{\partial x} \\ \frac{\partial J_{20}}{\partial y} &= -v_y^* \text{ (source)} - \frac{\partial H_{02}}{\partial y} \\ \frac{\partial J_{20}}{\partial z} &= -v_z^* \text{ (source)} - \frac{\partial H_{02}}{\partial z} \end{aligned} \right\} \quad (40)$$

$$\left. \begin{aligned} \frac{\partial \phi_{20}^*}{\partial x} &= z \frac{\partial J_{20}}{\partial x} + 2x \frac{\partial \phi_{10}^*}{\partial x} - x^2 \frac{\partial \phi_{00}^*}{\partial x} - 2zv_x^* \text{ (source)} \\ \frac{\partial \phi_{20}^*}{\partial y} &= z \frac{\partial J_{20}}{\partial y} + 2x \frac{\partial \phi_{10}^*}{\partial y} - x^2 \frac{\partial \phi_{00}^*}{\partial y} \\ \frac{\partial \phi_{20}^*}{\partial z} &= z \frac{\partial J_{20}}{\partial z} + 2x \frac{\partial \phi_{10}^*}{\partial z} - x^2 \frac{\partial \phi_{00}^*}{\partial z} + J_{20} \end{aligned} \right\} \quad (41)$$

To convert velocities from the panel coordinate system to the body system of figure 34, the transformation matrix  $[a_{ij}]$  is employed.

It is to be noted that the influence functions are exact for any field point location. Approximate intermediate-field and far-field formulas were not furnished by Hess and have not yet been incorporated. The advantage of such approximations would be a significantly reduced computing effort at no appreciable loss of accuracy for points not in the immediate vicinity of the panel. For example, in the far field representation the effect of the uniform source density  $\sigma$  on the trapezoidal panel of area  $A$  is represented by a point source of strength  $\sigma A$  positioned at the panel centroid. The formulas for a point source are, of course, far simpler than those for a distributed surface singularity.

Doublet Distribution Surface Fit Approaches - On each panel the doublet distribution is described by the six quadratic coefficients  $\mu_{00}, \dots, \mu_{02}$ . Several approaches were considered for matching the distributions on neighboring panels in order to accurately model the analytic doublet distribution and to minimize doublet discontinuities at panel edges. An approach developed by Boeing (Reference 16) was selected for implementation in the Douglas Neumann Program modifications. The essence of this approach involves passing a least squares quadratic through the boundary condition control point of a panel and through the control points of the adjacent eight panels. An alternate Boeing approach for generating improved doublet continuity characteristics was also coded and tested, but proved to be numerically unstable if the panel network is not composed of nearly straight generator lines. A new approach that improves both the continuity and accuracy of the quadratic doublet representations without introducing numerical instabilities was developed under this study but has not yet been coded for the computer. A discussion on the various formulations is presented below.

The numerical requirements for achieving continuity can be illustrated by considering a broken line segment model of a continuous function  $y = f(x)$ . See figure 39. Over each interval  $i$ , the model is described by  $y = a_i x + b_i$ , where the coefficients  $a_i$  and  $b_i$  are analogous to the six quadratic coefficients  $\mu_{00}, \dots, \mu_{02}$  of a panel in the surface doublet distribution. Consistent with the continuity of function  $f(x)$ , the broken line segment model is required to be continuous at interval endpoints. If  $x_i$  is the endpoint between intervals  $i$  and  $i+1$ , continuity is imposed by the condition:

$$a_i x_i + b_i = a_{i+1} x_i + b_{i+1}$$

which can be re-expressed as:

$$a_{i+1} = a_i - \frac{(b_{i+1} - b_i)}{x_i} \quad (42)$$

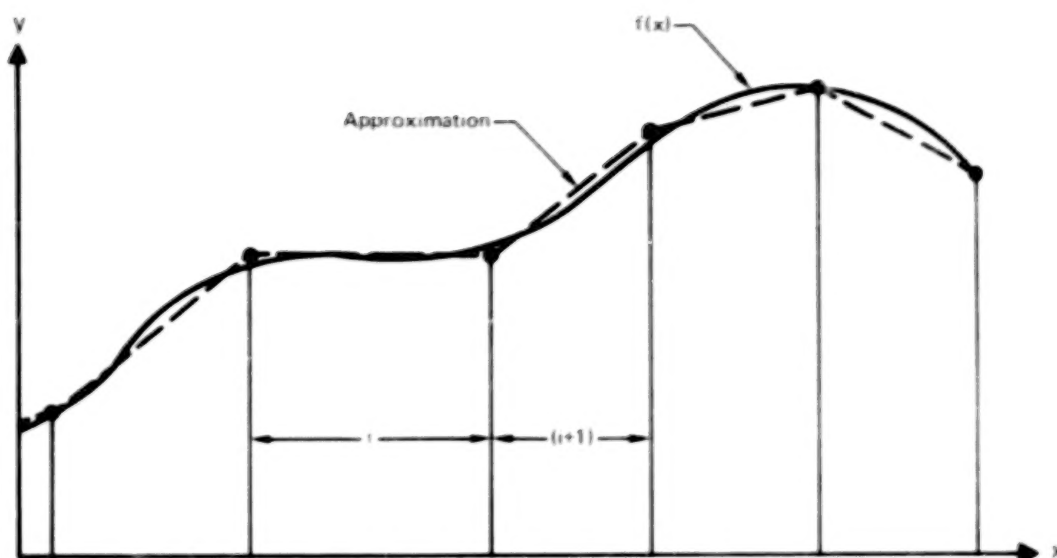


Figure 39. Broken Line Segment Approximation to Function  $f(x)$

Regardless of the function  $f(x)$ , equation (42) expresses the continuity constraint that  $a_{i+1}$  is a linear function solely of  $a_i$ ,  $b_i$ , and  $b_{i+1}$ . In other words, there is approximately one free parameter per interval for adjusting the broken line segment model to most nearly match the curve  $f(x)$ . The remaining coefficients are entirely dictated by continuity.

The necessity for minimizing doublet discontinuities is apparent upon examination of a simple numerical example. Consider a two-dimensional doublet distribution described by the equation

$$\mu = s^3$$

where  $\mu$  is doublet density and  $s$  is surface distance. A cubic has been selected because it cannot be modelled exactly by quadratic curves. Now suppose piecewise quadratic interpolating curve fits are made to the doublet distribution between integral values of  $s$ . That is, the endpoints are at  $s = \dots, -2, -1, 0, +1, +2, \dots$ . Of the many possible types of quadratic fit, two are illustrated in figure 40 over the range  $0 \leq s \leq 2$ . The first curve fit (A) is continuous with continuous slopes at panel

endpoints, equivalent to the piecewise linear vortex distribution employed in the method of references (19-21). In this case, the quadratic fit was determined such that the exact slope is attained at all panel endpoints and such that the curve fit passes through the exact value of doublet density at  $s = 1$ . The second quadratic curve fit (B) was established at each interval by passing a parabola through the exact doublet density at the interval midpoint and at the midpoints of the two adjacent intervals. At this stage it is difficult to predict which type curve fit would be most accurate for use in a numerical surface singularity method. Whereas the discontinuity in curve fit B at  $s = 1$  is obviously nonexistent in the exact distribution, such discontinuities do allow quadratic fit B to attain a more accurate average doublet density in each interval than curve fit A. The analytic gradient of the doublet distributions provides the equivalent vortex density curve fits (figure 41). For curve fit B, the doublet discontinuity at  $s = 1$  is reflected by a delta function in the vortex distribution.

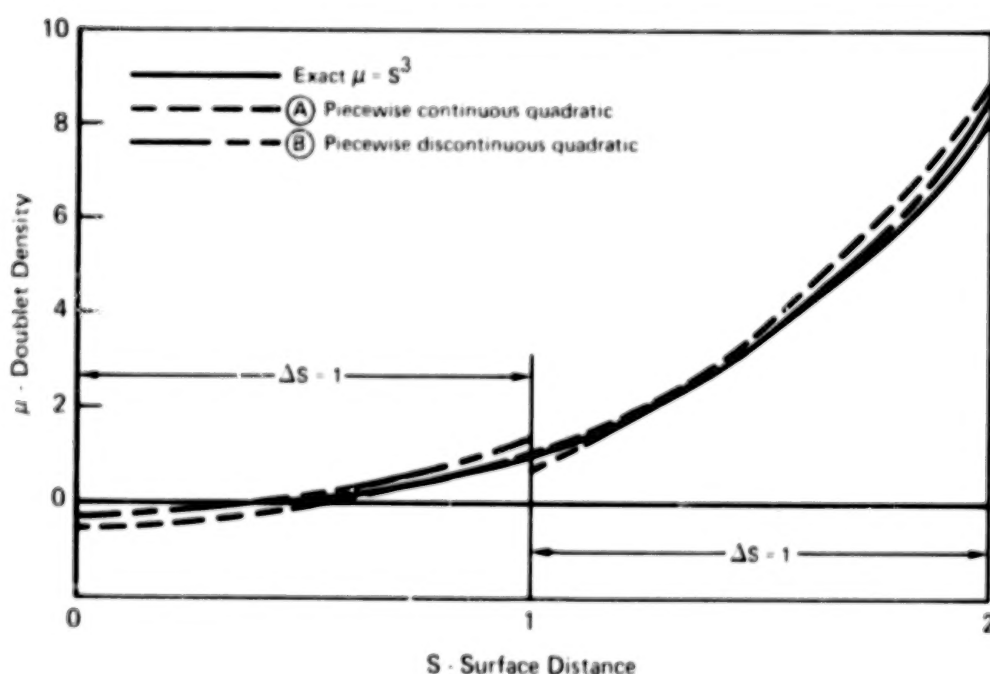
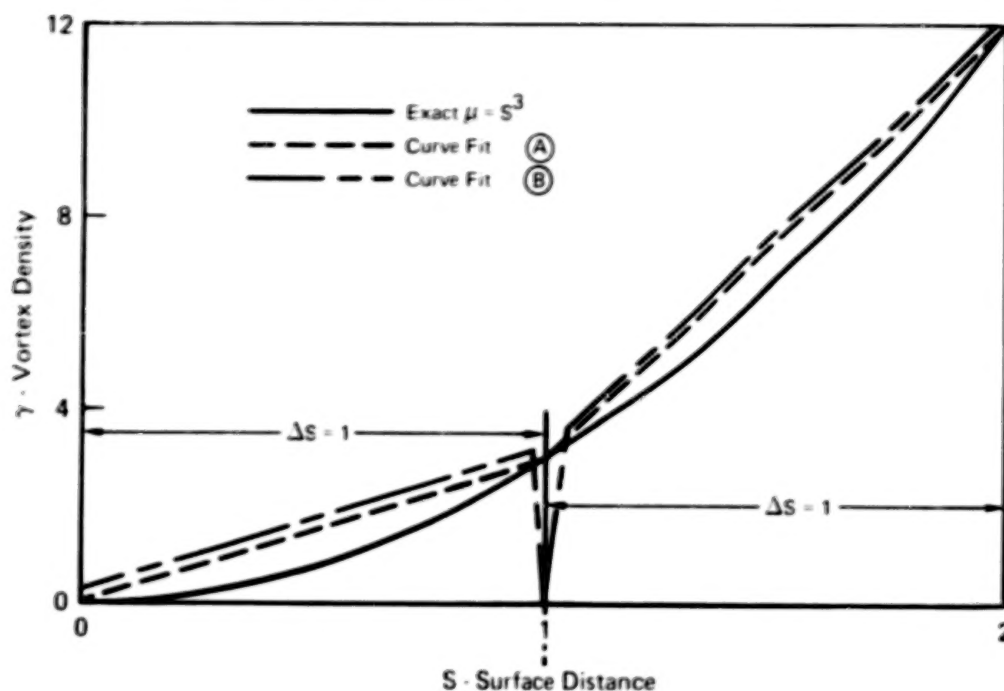


Figure 40. Two Curve Fits to a Doublet Distribution



**Figure 41. Vortex Distribution - Corresponds to Figure 40**

Neither the doublet nor vortex distributions reveal the significant numerical consequences of the type of curve fit. However, the corresponding normal velocity distribution is highly informative. For both curve fits and for the exact doublet distribution, the normal velocity induced by the section of doublet distribution between  $s = 0$  and  $s = 2$  was calculated analytically. A finite vortex filament was included in each case at  $s = 2$  to counteract the doublet discontinuity magnitude  $\mu = 8$ .

Plotted as a function of surface distance  $s$  in figure 42, the normal velocity distribution corresponding to curve fit B is seen to be the more accurate in the vicinity of  $s = 1/2$  and  $s = 3/2$ , which would correspond to control point locations in a panel method. However, the effect of the concentrated vortex at  $s = 1$  leads to numerical instabilities for curve fit B. The consequences are quite clear. No matter what type panel spacing is used or how close a control point is to a panel edge, curve fit A will provide a reasonable approximation to the actual exact normal velocity curve. On the other hand, curve fit B is obviously in error unless the control point is very close to the

panel midpoint. Therefore, erroneous calculations could result if prescribed normal velocity boundary conditions were used with curve fit B. Although it is less obvious, the application of internal potential boundary conditions would not eliminate the problem. In fact, for a thin wing with upper and lower surface panels sharing a common chord plane projection, the use of internal potential boundary conditions approaches equivalency to lifting surface theory as wing thickness vanishes. It is concluded that minimizing doublet discontinuity is highly beneficial to the modelling of a doublet distribution.

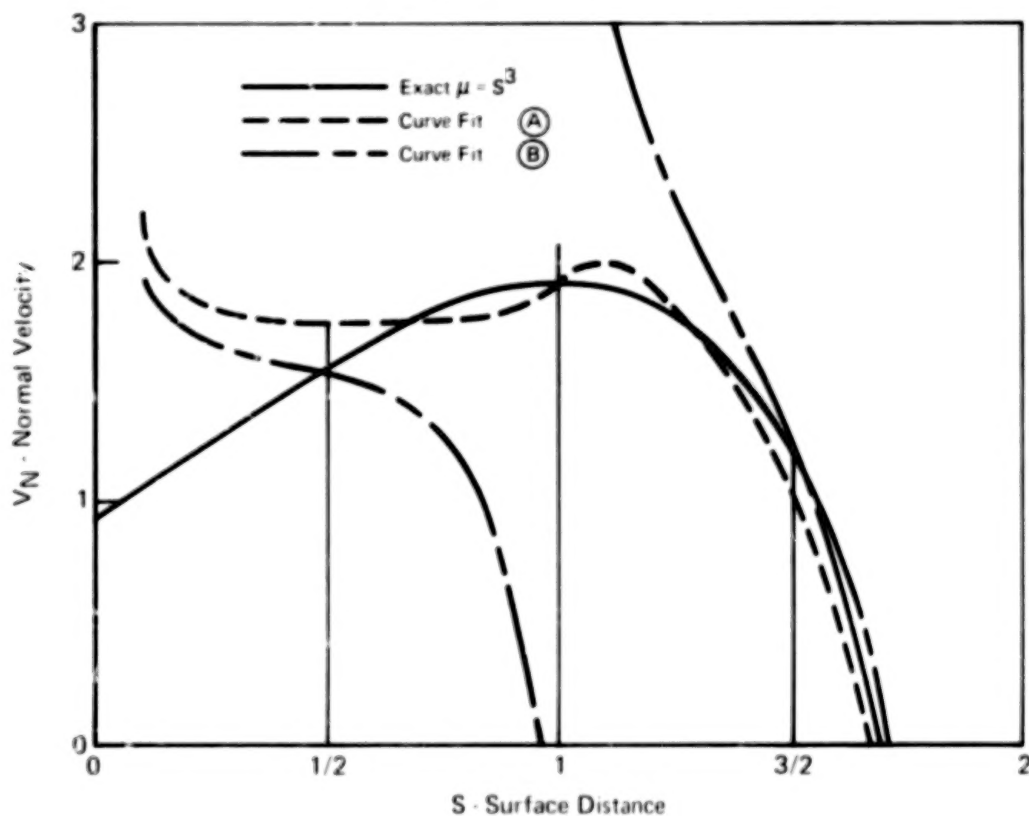


**Figure 42. Normal Velocity Distribution - Corresponds to Figure 40**

If a three-dimensional doublet representation is to satisfy the three guidelines presented in the introduction to this section, it is necessary that the doublet density on each panel vary as a second order polynomial in terms of coordinates in the plane of the panel. The objective is to adjust the coefficients such that boundary conditions are satisfied at approximately one control point per panel with as smooth a doublet distribution on the panel network as possible.

A schematic of the selected control point locations is furnished in Figure 43. For each trapezoidal panel there is one control point at the centroid. Additional control points are placed along the edges of a section at the trapezoidal panel side midpoints and at section corners. The purpose of the additional points is to generate doublet continuity at adjacent section edges without requiring two-sided surface fits to the doublet distribution across the edges.

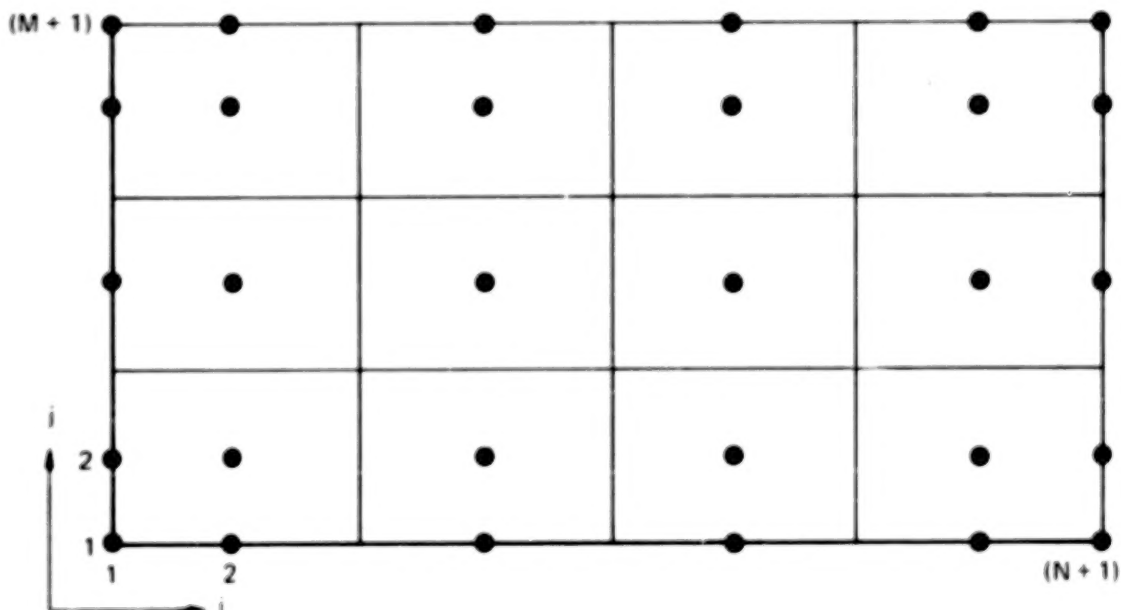
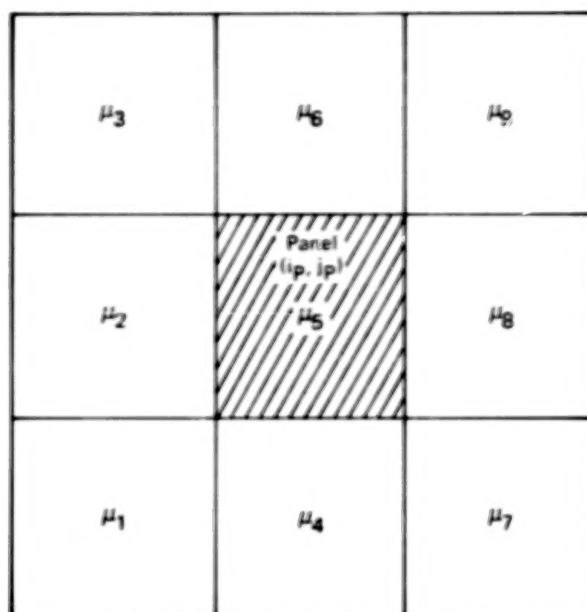


Figure 43. Schematic of Panel Control Point Locations on a Section

The entire doublet distribution on a section is uniquely determined by the set of doublet densities at the control point locations. On each panel the distribution which has been selected for use in this study is generated by a least squares quadratic fit through nine neighboring control points. For example, consider any panel  $(i_p, j_p)$ , which is schematically illustrated in Figure 44. The doublet density at the panel centroid control point and at the eight adjacent control points is identified by subscript  $k$  ( $1 \leq k \leq 9$ ). If panel  $(i_p, j_p)$  is on the edge of a section then some of the adjacent control points will be on panel edges. The following table provides the conversion between control point index  $k$  of Figure 44 and indices  $(i, j)$  of Figure 43.





**Figure 44. Indexing Convention for  $\mu$  in Vicinity of Panel  $(i_p, j_p)$**

**TABLE II - CONTROL POINT INDEX  $(i, j)$   
[Panel Index  $(i_p, j_p)$ ]**

$k$	$i$	$j$
1	$i_p$	$j_p$
2	$i_p$	$j_p + 1$
3	$i_p$	$j_p + 2$
4	$i_p + 1$	$j_p$
5	$i_p + 1$	$j_p + 1$
6	$i_p + 1$	$j_p + 2$
7	$i_p + 2$	$j_p$
8	$i_p + 2$	$j_p + 1$
9	$i_p + 2$	$j_p + 2$

The second order polynomial  $\mu(\xi, \eta)$  of Equation (33) is the doublet distribution on panel  $(i_p, j_p)$ . The six coefficients  $\mu_{00}, \dots, \mu_{02}$  are determined by minimizing the following error function  $E$



$$E \equiv \sum_{k=1}^9 \{W_k [\mu(\xi_k, \eta_k) - \mu_k]^2\} \quad (43)$$

$(\xi_k, \eta_k)$  are the coordinates  $(\xi, \eta)$  of the  $k$ th control point. For control points  $k$  that are either at the centroid or on the edge of panel  $(i_p, j_p)$ , a very large weight factor  $W_k \gg 1$  is selected. Otherwise,  $W_k$  is chosen as unity. This weighting matches the function  $\mu(\xi, \eta)$  to the values  $\mu_k$  at control points on the panel and provides approximate matching at the remaining control points.

Equation (43) is minimized with respect to each coefficient  $\mu_{00}, \dots, \mu_{02}$ . This leads to a system of six linear equations. If the six coefficients  $\mu_{00}, \mu_{10}, \mu_{01}, \mu_{20}, \mu_{11}, \mu_{02}$  are respectively identified by  $\beta_1, \beta_2, \dots, \beta_6$ , then the solution to the system of equations can be expressed in the following form:

$$\beta_\ell = \sum_{k=1}^9 B_{\ell k} \mu_k \quad (1 \leq \ell \leq 6) \quad (44)$$

The array  $B_{\ell k}$  is determined by matrix inversion and depends solely on the panel geometry, not on the values  $\mu_k$ . Therefore array  $B_{\ell k}$  can be determined before solving for the doublet strength.

The above surface fitting approach for establishing the doublet distribution is equivalent to method "B" in the two-dimensional example of Figures 40-42. Admittedly, the resultant doublet continuity properties at panel edges are not ideal. An alternate approach developed by Boeing in an unpublished report reduces to method "A" for the special case of two-dimensional flow. This alternate approach was coded under the present study and is available in the modified Douglas Neumann Program. For cases in which the paneled geometry of a section is defined by (nearly) straight generator lines, the alternate approach is accurate and has good continuity properties. Otherwise, however, the calculated array analogous to  $B_{\ell k}$  tends to be numerically

unstable. Therefore, the former approach was selected and was used in all the three-dimensional examples of this report.

A third approach, previously investigated by Boeing, involves reducing the discontinuities at panel edges after the doublet distribution has been determined. The computed doublet densities at panel edges from the initial doublet distribution are averaged to generate a new, nearly continuous distribution. Then a least squares second order fit is passed through the new edge values. The drawback is that the discontinuities should be eliminated prior to satisfying boundary conditions, not after. The significant numerical instability associated with doublet discontinuities is that boundary conditions become unrealistically sensitive to panel geometry and control point location.

An improvement to the third approach has been developed under this study, but has not been coded at this time. The essence of the present improved approach involves minimizing doublet discontinuities at eight peripheral points on each panel prior to solving for the unknowns. This is possible because the doublet distribution on each panel is a linear function of the unknowns, where the unknowns are the doublet density at the adjacent control points of Figure 43. Four of the eight peripheral points on a panel are the corners and four are the side midpoints (Figure 45). In order to assure that adjacent panels in a section will share identical peripheral point locations at a corner or edge, the eight point locations of Figure 45 are to be interpreted as lying on the sides of the non-planar quadrilateral panel which was defined prior to the trapezoidal approximation. Doublet discontinuities at panel edges are minimized by attempting to match the doublet distributions of adjacent panels to a common desired value at each of the peripheral points shared by the adjacent panels. Details of the present improved approach are discussed below.

A second order quadratic fit  $\mu(\xi, \eta)$  is to be established on each panel

$$\mu(\xi, \eta) = B_1 + B_2 \xi + B_3 \eta + B_4 \xi^2 + B_5 \xi \eta + B_6 \eta^2 \quad (45)$$

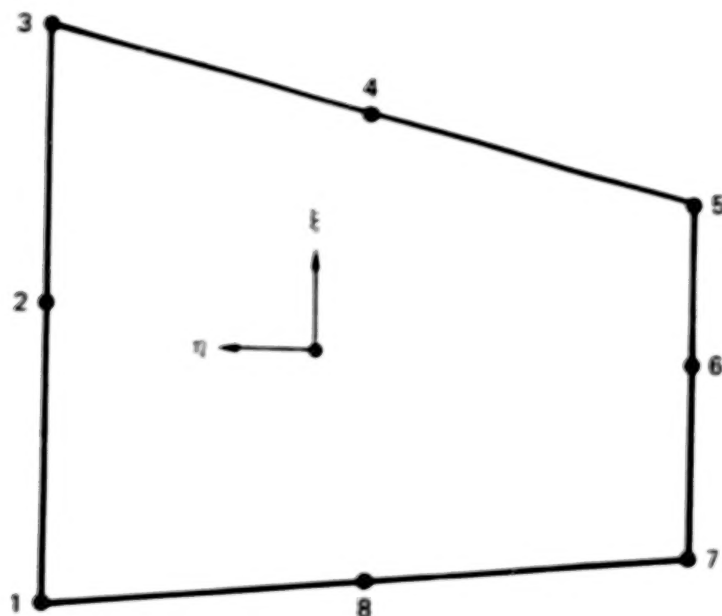


Figure 45. Panel Edge Locations for Doublet Matching

For each panel, the coefficients  $\beta_{\ell}$  ( $1 \leq \ell \leq 6$ ) are determined by an exact matching of  $\mu(\xi, \eta)$  to the unknown centroid value and a least square error matching to desired doublet values at the eight panel peripheral points. For any peripheral points that are on the edge of the section, the square error weighting is selected to make the matching exact. If  $\mu_c$  is the unknown centroid doublet density of the panel and  $\mu_{pk}$  ( $1 \leq k \leq 8$ ) identifies the desired doublet density at the eight peripheral points, then the method of least squares generates a relationship in the following form:

$$\beta_{\ell} = B_{c_{\ell}} \mu_c + \sum_{k=1}^8 B_{p_{\ell k}} \mu_{p_k} \quad (1 \leq \ell \leq 6) \quad (45)$$

The coefficients  $B_{c_{\ell}}$  and  $B_{p_{\ell k}}$  are functions of only the panel corner coordinates (prior to the trapezoidal approximation).

By expressing  $\mu_{p_k}$  ( $1 \leq k \leq 8$ ) as a linear combination of the unknown doublet densities at several neighboring control points and then substituting the expression into Equation (46), the coefficients  $\beta_{\ell}$  of a panel will be in the following form:

$$\beta_{\ell} = \sum_m B_{\ell m} \mu_m \quad (1 \leq \ell \leq 6) \quad (47)$$

where  $\mu_m$  refers to the unknown doublet densities at control points in the vicinity of the panel.

To determine  $\mu_{pk}$  as a linear combination of the unknowns, an interpolating least squares surface fit is passed through the control point doublet densities in the neighborhood of the panel peripheral point  $k$ . For best interpolation accuracy, the greatest least squares weighting should be assigned to control points closest to point  $k$ .

The array  $B_{lm}$  of Equation (47) is a function only of the corner point coordinates of neighboring panels and is determined prior to solving for the unknowns  $\mu_m$ . The limits of  $m$  in Equation (47) depend upon the number of neighboring control points used in the interpolation for  $\mu_{pk}$ . The limits  $1 \leq m \leq 25$  are expected to be adequate.

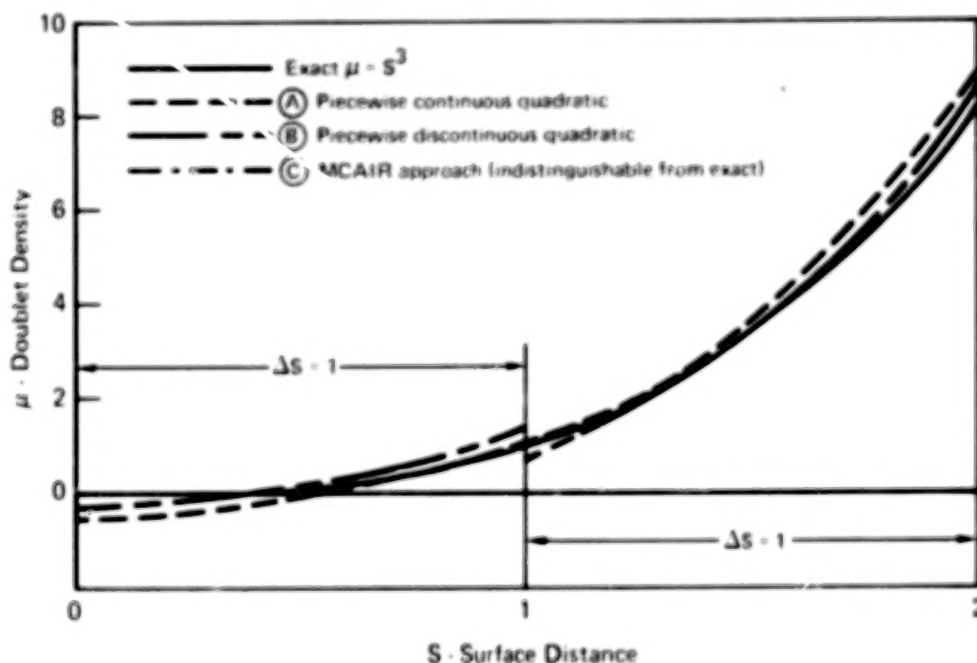


Figure 46 Three Quadratic Curve Fits to a Doublet Distribution

The present approach is expected to improve both the accuracy of the doublet distribution and the continuity properties, at the expense of slightly greater computational effort. However, it is expected that the increased effort will be insignificant compared to what is required in establishing influence coefficients and solving the system of linear boundary condition equations.

The numerical characteristics are aptly illustrated by re-examining the simple two-dimensional example of Figures 40-42 with the inclusion of the present approach (curve C). It is noted that in terms of doublet density (Figure 46), vortex density or doublet gradient (Figure 47), and induced normal velocity (Figure 48), the present method most nearly matches the analytic curve. The significance is revealed in the normal velocity distribution of Figure 48. Regardless of where one might select a boundary condition control point, the boundary value is sufficiently close to exact to suppress unwarranted numerical instabilities. Therefore, panel geometry and control point location can be expected to have only a minor effect on computed results, which is compatible with simplified user requirements.

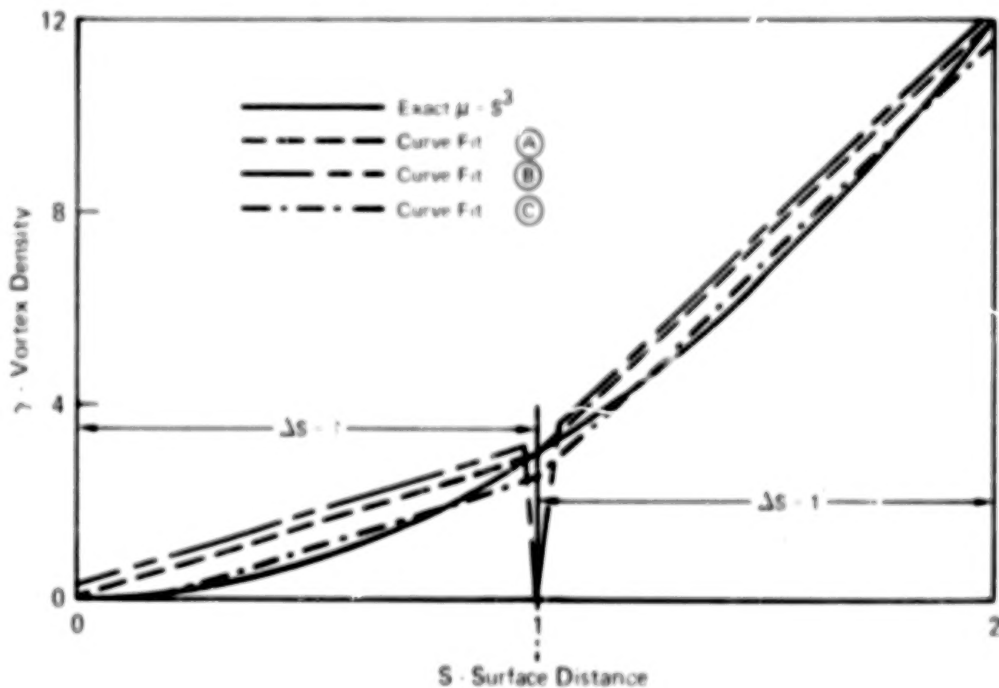


Figure 47. Vortex Distribution - Corresponds to Figure 46

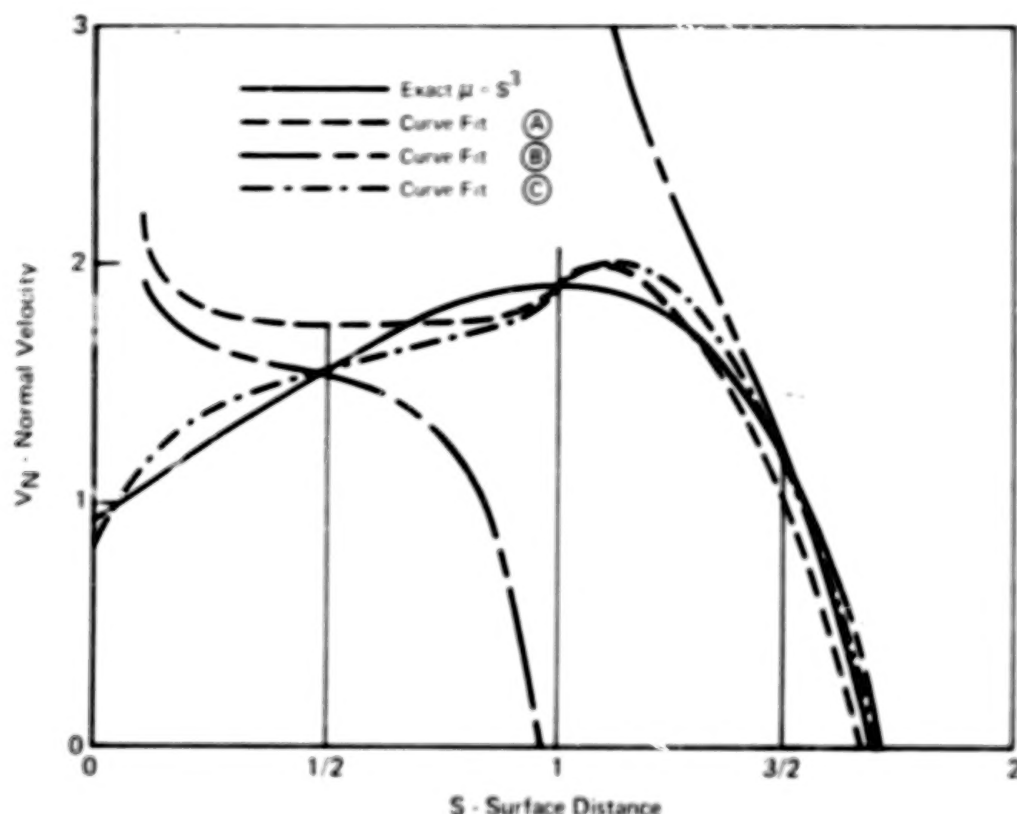


Figure 48. Normal Velocity Distribution - Corresponds to Figure 46

#### Boundary Conditions

The indirect approach of applying internal potential boundary conditions is applied in view of the good accuracy and stability exhibited in the two-dimensional examples presented earlier. The two steps to satisfaction of the boundary condition are to set the source density on each panel equal to the negative of the local free stream normal velocity component and subsequently to determine the doublet distribution corresponding to zero internal perturbation potential at selected control point locations. As explained in the section Potential Flow Theory, such an approach is theoretically equivalent to prescribing solid body flow tangency conditions.

Several other approaches for applying boundary conditions are conceivable. For example, the net velocity flux through a control surface bounded by four neighboring panel centroids could be prescribed as zero. This would require analytical integration to formulate velocity flux influence coefficients

# TABLE OF CONTENTS

<u>Section</u>	<u>Page</u>	
SUMMARY . . . . .	1	1/A13
INTRODUCTION. . . . .	3	1/B1
POTENTIAL FLOW THEORY . . . . .	5	1/B3
Laplace Equation . . . . .	5	1/B3
Singular Solutions . . . . .	8	1/B6
Boundary Conditions. . . . .	13	1/B11
Wakes. . . . .	22	1/C6
RESEARCH ON GREEN'S IDENTITY FORMULATION. . . . .	26	1/C10
Comparison of Surface Paneling Methods . . . . .	27	1/C11
Internal Potential Boundary Condition Formulation. . . . .	33	1/D3
Comparison of Green's Identity Formulations. . . . .	38	1/D8
Accuracy of Concave Corner Solutions . . . . .	49	1/E5
Inverse (Design) Capability. . . . .	55	1/E11
Selected Formulation . . . . .	60	1/F2
NUMERICAL SOLUTION FORMULATION. . . . .	61	1/F3
Geometry Panel Modeling. . . . .	64	1/F6
Panel Singularity Distribution . . . . .	70	1/F12
Influence Function Formulas . . . . .	70	1/F12
Doublet Distribution Surface Fit Approaches . . . . .	74	1/G2
Boundary Conditions. . . . .	86	1/G14
Calculation of Flow Properties . . . . .	90	2/A5
CALCULATED RESULTS. . . . .	92	2/A7
CONCLUSIONS AND RECOMMENDATIONS . . . . .	110	2/B11
REFERENCES. . . . .	112	2/B13



for three-dimensional geometries, but would reduce to the successful stream function approach of Oellers (Ref 10) for two-dimensional flow. However, the present internal potential boundary condition approach is believed to provide the best compromise with respect to accuracy, numerical stability, computational efficiency, and availability of influence functions.

The source density on each body panel is calculated from the dot product of the free stream velocity  $\vec{V}_\infty$  with the local normal direction  $\vec{e}_\zeta$ , in accordance with equation (16).

$$\begin{aligned}\sigma &= - \vec{V}_\infty \cdot \vec{e}_\zeta \\ &= - (\alpha_x a_{31} + \alpha_y a_{32} + \alpha_z a_{33})\end{aligned}\quad (48)$$

For wake panels the source strength is prescribed to be zero, corresponding to the assumption of negligible viscous displacement effects.

A schematic of the control point locations was presented earlier in Figure 43. The edge control points do not lie precisely on the trapezoidal panel edges, but are instead moved a few percent of local panel dimensions toward the centroid. This repositioning prevents contact with the concentrated vortex filament that bounds the edges of a doublet sheet.

At each control point on a section of body panels, the boundary condition is imposed that the internal perturbation potential induced by the simultaneous action of all singularities is zero. The internal potential is evaluated at  $\zeta = 0^-$ , i.e., on the non-fluid surface of the panel. At the control points along one edge of each section of wake panels (Figure 49), the imposed boundary condition is that the total velocity component normal to the panel is zero. By aligning this section edge with the trailing edge of a lifting body, the Kutta condition of wake tangency is satisfied. Zero doublet gradient is prescribed along the  $j$ -direction of the wake panels, corresponding to the absence of wake loading. This eliminates the need to prescribe boundary conditions at the other wake control points.



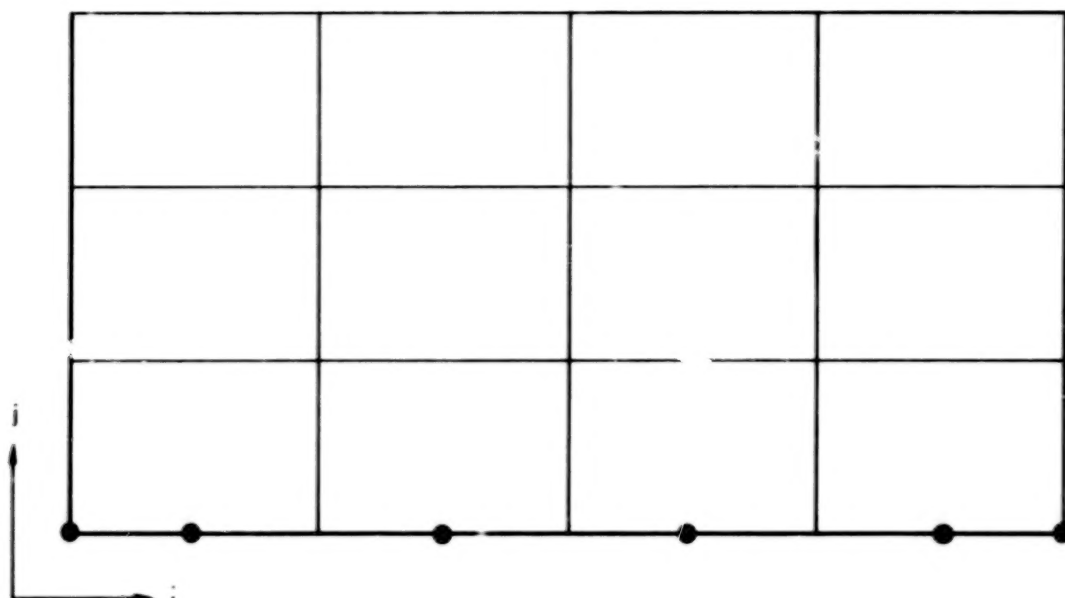


**Figure 49. Schematic of Wake Boundary Condition Control Points**

The present approach of prescribing zero internal perturbation potential at edge control points provides for a continuous carryover of doublet density from one section to another. On each side of the intersection between two sections, the edge control point will have the same value of internal perturbation potential, zero. Because the difference in potential across the intersection is dominated by the magnitude of the local doublet discontinuity, the absence of any difference assures doublet continuity. The discontinuity in doublet gradient (vortex density) is dictated by the change in potential between the edge and centroid control points of a panel. In fact, the present approach is equivalent to the formulation for predicting the vortex discontinuity at sharp corners which was described in the section "Research on Green's Identity Formulation." Therefore, the present method can be applied to sharp concave corners at wing-fuselage intersections. Whereas the absence of a sharp corner does not negate the applicability of the approach, it would probably be preferable to eliminate edge control points in cases in which the body is smooth at the section edge. This would require the introduction of special indexing to carry the

doublet distribution surface fit from one section to another. It is anticipated that such indexing will be established in the future.

The prescription of zero internal perturbation potential at edge control points is believed to be less sensitive to gaps and control point location than the Boeing approach of prescribing zero normal velocity at the same points (Reference 16). For example, consider a simple two-dimensional problem in which two adjacent parallel panels exhibit a slight gap (Figure 50). Assume that there is a unit strength doublet density on both panels. The corresponding potential and normal velocity component induced by the two doublet panels is plotted as a function of position in Figure 50. Whereas the normal velocity distribution is a singular function of both position and gap at the panel edges, the distribution of potential is well-behaved on both panels. Similar behavior is evident regardless of the angle between the two panels. Hence the present approach should be consistently reliable even without the introduction of special additional treatment at section edges.

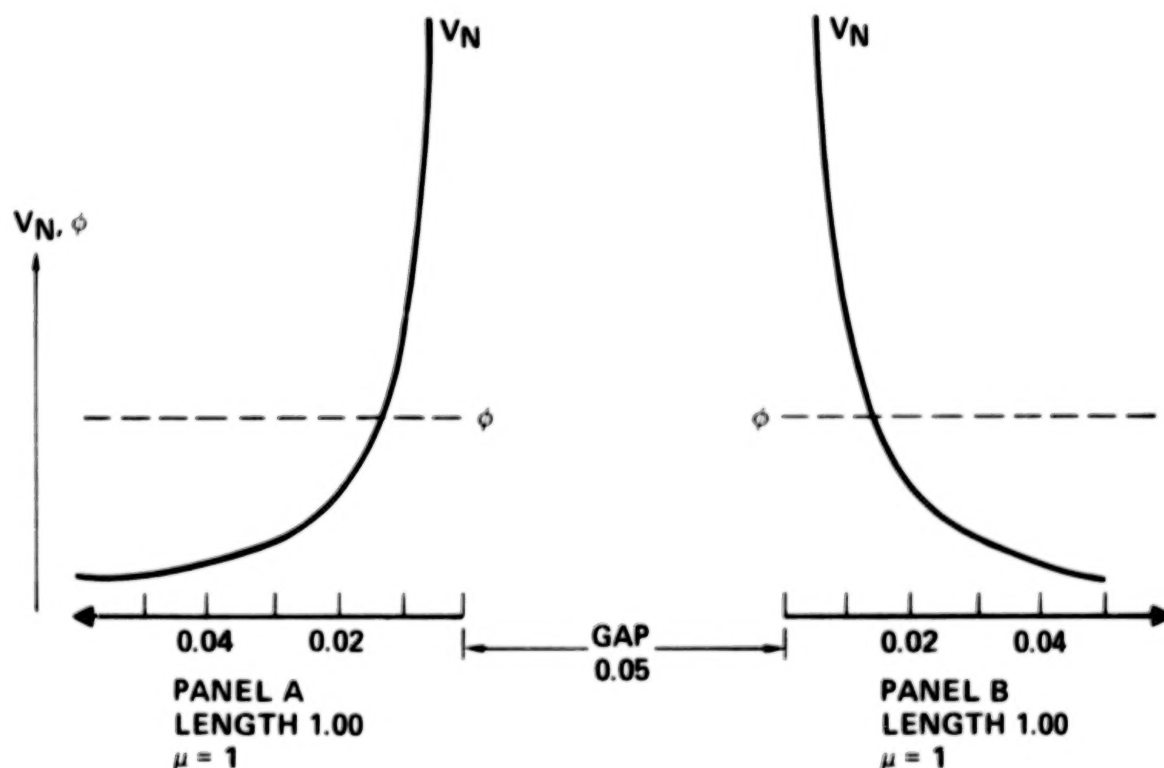


Figure 50. Potential and Normal Velocity in Vicinity of Adjacent Panel Edges

By combining the influence functions of equations (36)-(41) with equations (34), it is possible to establish a system of linear equations relating the unknown set of control point doublet densities to the imposed boundary conditions. The number of equations and unknowns are equal, and the solution renders the complete singularity distribution for all panels known.

In order to simplify the solution for more than one free stream vector  $\vec{V}_\infty$ , three right-hand-sides to the system of equations are solved simultaneously, with each right-hand-side denoted by a different subscript.

$$\left. \begin{aligned} \vec{V}_{\infty 1} &\equiv \vec{e}_x \\ \vec{V}_{\infty 2} &\equiv \vec{e}_y \\ \vec{V}_{\infty 3} &\equiv \vec{e}_z \end{aligned} \right\} \quad (49)$$

Then for any vector  $\vec{V}_\infty$ , the solution singularity strengths can be generated as a simple linear combination of the solutions for  $\vec{V}_{\infty 1}$ ,  $\vec{V}_{\infty 2}$ , and  $\vec{V}_{\infty 3}$ .

#### Calculation of Flow Properties

At each panel centroid the equality between tangential perturbation velocity component and doublet gradient is employed to calculate the total local flow velocity  $\vec{V}$ . In the panel coordinate system  $(\xi, \eta, \zeta)$ ,

$$\begin{aligned} \vec{V} &= (\vec{V}_\infty \cdot \vec{e}_\xi + \frac{\partial \mu}{\partial \xi}) \vec{e}_\xi + (\vec{V}_\infty \cdot \vec{e}_\eta + \frac{\partial \mu}{\partial \eta}) \vec{e}_\eta \\ &= (\vec{V}_\infty \cdot \vec{e}_\xi + \beta_2) \vec{e}_\xi + (\vec{V}_\infty \cdot \vec{e}_\eta + \beta_3) \vec{e}_\eta \end{aligned} \quad (50)$$

The components in system  $(x, y, z)$  are obtained with the aid of the rotation matrix  $[a_{ij}]$ .

Pressure coefficient is calculated by Bernoulli's equation.

$$c_p = 1 - \left( \frac{V}{V_\infty} \right)^2$$

Force and moment integration is performed under the assumption that the centroid pressure of each panel acts on the entire flat trapezoidal geometry. The resulting integration accuracy is consistent with the basic solution formulation.

## CALCULATED RESULTS

Surface pressure distributions were calculated for several three-dimensional geometries in order to assess the relative merits of the modified program developed under this study and the existing Douglas Neumann program. Hereinafter, the modified and existing programs are respectively designated "present method" and "Hess program." The authors are grateful to James Thomas of NASA, Langley Research Center, for his interest and effort in the selection and testing of the examples.

The geometry selection included shapes for which prediction accuracy by the Hess program is characteristically good as well as shapes for which the program tends to be unreliable. The former category includes isolated solid bodies of revolution, wings of conventional section geometry, and typical wing-fuselage combinations. The latter category includes wings with thin, highly loaded trailing edge regions and internal duct flow.

The first example is intended to reveal whether calculated pressure distributions for wings of high aspect ratio tend to reflect the 2-D numerical characteristics discussed earlier in the section "Research on Green's Identity Formulation." The supercritical geometry of Figure 51 was panelled as an unswept wing of rectangular planform with constant cross-section and aspect ratio 100. Ten equally spaced spanwise strips of panels were employed. Two chordwise panel spacing distributions were examined, each having a total of 40 panels per spanwise strip. Both the spacings, cosine and  $\cos/\sinh$ , are dense in the trailing edge region, with the former being the denser of the two. The calculated chordwise pressure distributions near the root are presented in Figure 51 for the two programs and for the virtually exact 2-D conformal mapping solution of Cathal-Sells (Reference 5). The present method solution is nearly independent of the panel spacing, whereas the Hess program solution is highly unstable. It is important to consider that in the Hess program a uniform chordwise surface vortex distribution is applied. Hess reports that his latest 3-D program has a parabolic vorticity option (analogous to that of Reference 22) and that for the

supercritical geometry the parabolic option would have substantially reduced the numerical instability. Nonetheless, the present example does support the conclusion that combined source-doublet methods are significantly more reliable than source methods for thin geometries subjected to strong pressure loading.

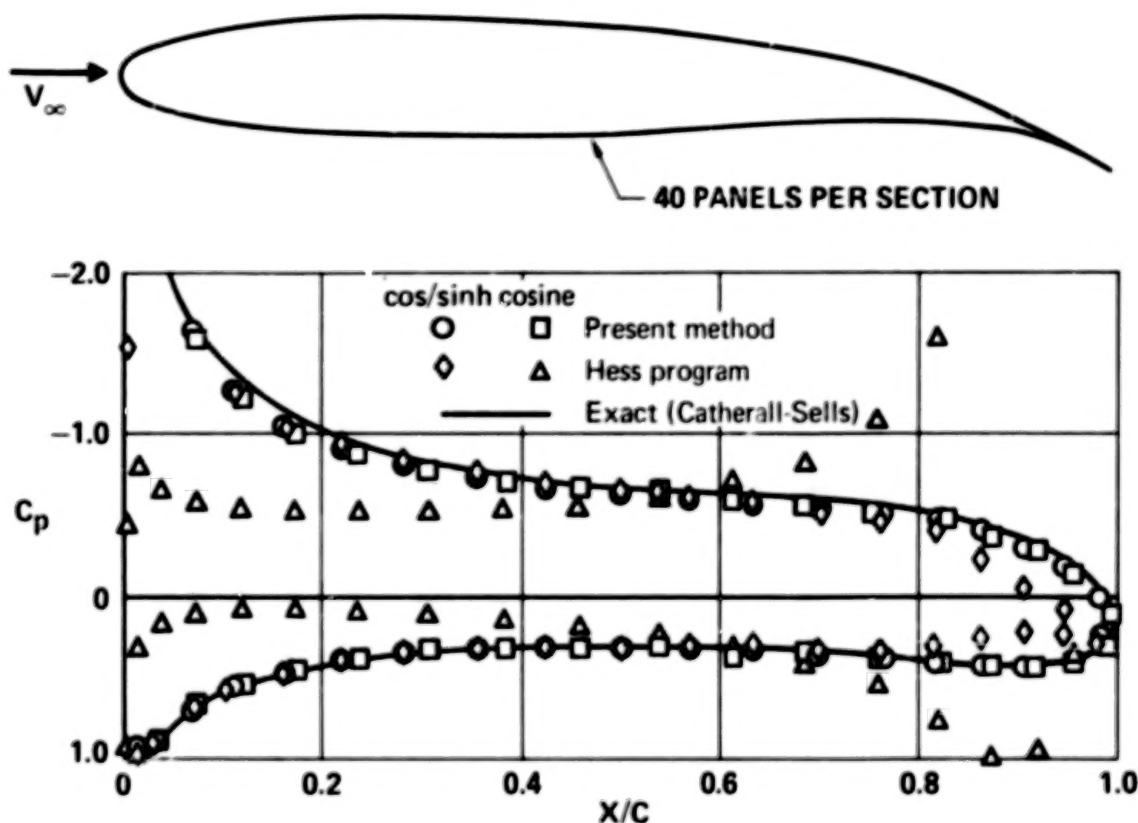


**Figure 51. Supercritical Wing**  
Effect of Panel Spacing, Rectangular Planform, AR = 100

The second example also involves modelling a 2-D airfoil as a high aspect ratio wing. The Williams two-element airfoil of Figure 16 was selected in order to determine whether the wake from the forward element disturbs the rear element pressure distribution. In viscous flow, the geometry of the forward element wake is significant; however, for purely inviscid flow with weak spanwise gradients, the pressure distribution is anticipated to be nearly independent of wake shape. The reasonable but crude wake geometry of Figure 52 was selected, and the wake was allowed to trail several dozen chords downstream. The planform and spanwise panel spacing definition are similar to those of the preceding example.

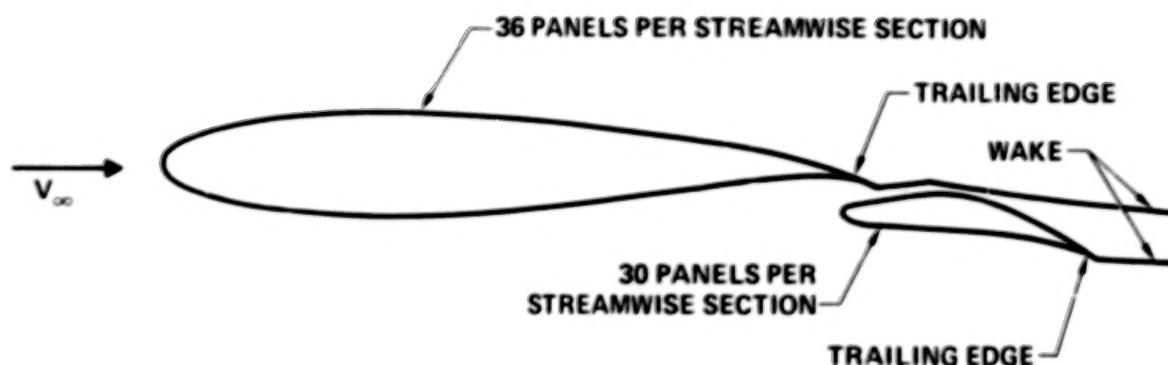


**Figure 52. Williams Two-Element Wing Geometry**  
 Rectangular Planform  $AR = 100$

For the present method, the chordwise spacing of Figure 16 was applied. For the Hess program, it was necessary to adjust the spacing of the rear element trailing edge panels such that the upper and lower surface control points nearly aligned. Without this adjustment, the calculated lift coefficient based on the Hess program equal pressure Kutta condition is approximately 25% too low in comparison with the exact value. The calculated chordwise pressure distributions near the root presented in Figure 53 show that the present method and exact solutions compare well. Even with the adjusted trailing edge panels, the Hess program significantly underpredicts lift. The probable explanation is that the trailing edge Kutta condition is sensitive to the locally strong source strengths.



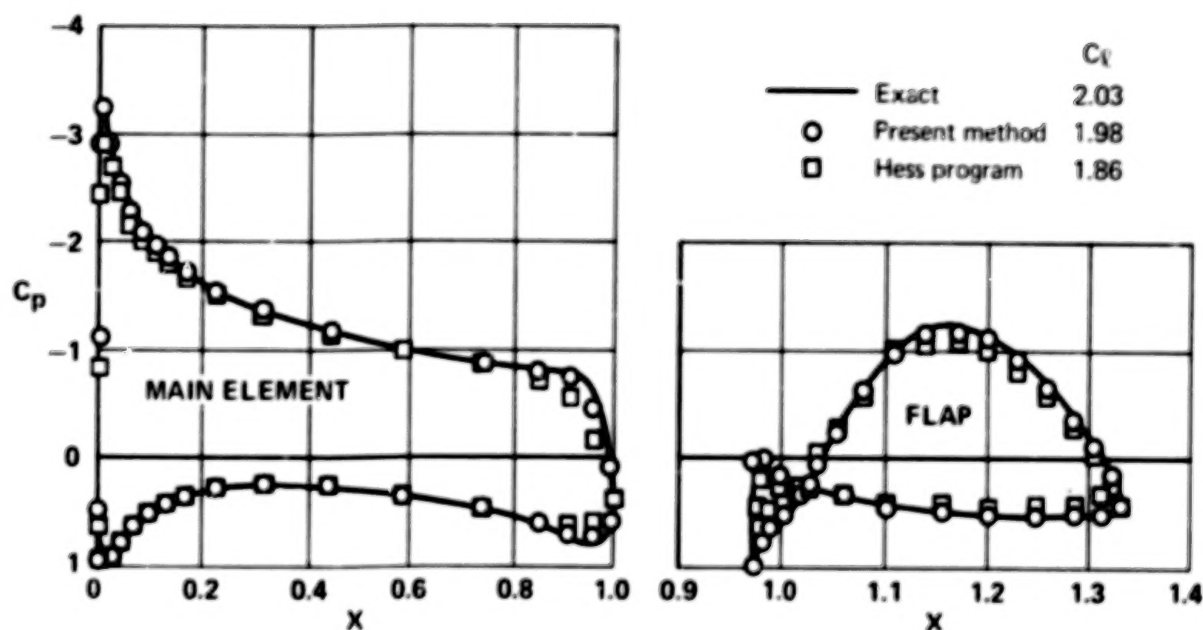


Figure 53. Williams 2-Element Wing Pressure Distribution

In each of the first two examples, the present method generates a slightly lower lift coefficient than the exact 2-D solution. This is characteristic of the effects of spanwise gradients on a finite wing. For a rectangular wing of aspect ratio 100, downwash reduces the root section lift coefficient one to two percent below the two-dimensional level.



Figures 54-56 present the calculated chordwise pressure distributions for an unswept wing of rectangular planform, aspect ratio six, and NACA 0012 cross section. Using the symmetry plane option, the wing semi-span was panelled, with 8 equal size strips spanwise and 40 panels per strip streamwise. Both the Hess and present methods show good agreement with experimental data at  $6.75^\circ$  angle of attack (Reference 24). No viscous corrections have been incorporated. It is noteworthy that in the tip region the Hess program results are superior to the present method. In particular, the upper and lower surface pressure distribution of the present method intersect at approximately 70% chord. It is believed that this behavior is associated with the quadratic surface fit to the doublet distribution. At the tip strip of panels the spanwise distance to the adjacent strip control points is twice the distance to the tip edge control points. This non-equal spacing, coupled with the large doublet spanwise gradients at the tip, generates significant errors in the surface fitting algorithm. Future implementation of the improved doublet fit approach described in the section "Numerical Solution Formulation" is expected to eliminate the difficulty. Of course, the less efficient approach of increasing the panel spanwise density near the tip would also improve the results.

The flow around the panelled sphere of Figure 57 was calculated by the present method. Only one-half of the sphere was panelled, and the symmetry plane option was employed. A hole approximately one percent of local panel dimensions was left at the north and south poles to prevent the exact coincidence of two edge control points of triangular panels. The flow was solved for two free stream directions, one parallel to the x-axis and one to the z-axis. The latter solution (Figure 58) is of greater interest because non-axisymmetric panelling is used to model an axisymmetric flow. For both free stream directions there is good agreement with the exact analytical solution. It is noteworthy that there is a slight scatter in the calculated results for panels at the edge of a section, although the magnitude of the scatter is smaller than the symbol size in Figure 58.

Apparently the edge control points do not generate surface continuity properties as well as the direct imposition of the quadratic surface fit between adjacent panels. The pressure distribution for the Hess program was also calculated and agrees well with the exact solution, but is not shown here.

Figure 59 illustrates an isolated axisymmetric fuselage with an open base. Identical panelling was used for both the present and Hess methods, and the calculated pressure distribution was compared to the solution generated by Hess' higher order axisymmetric surface singularity program (Reference 25). The higher order solution, considered to be virtually exact, is nearly matched by both the present and Hess program solutions.

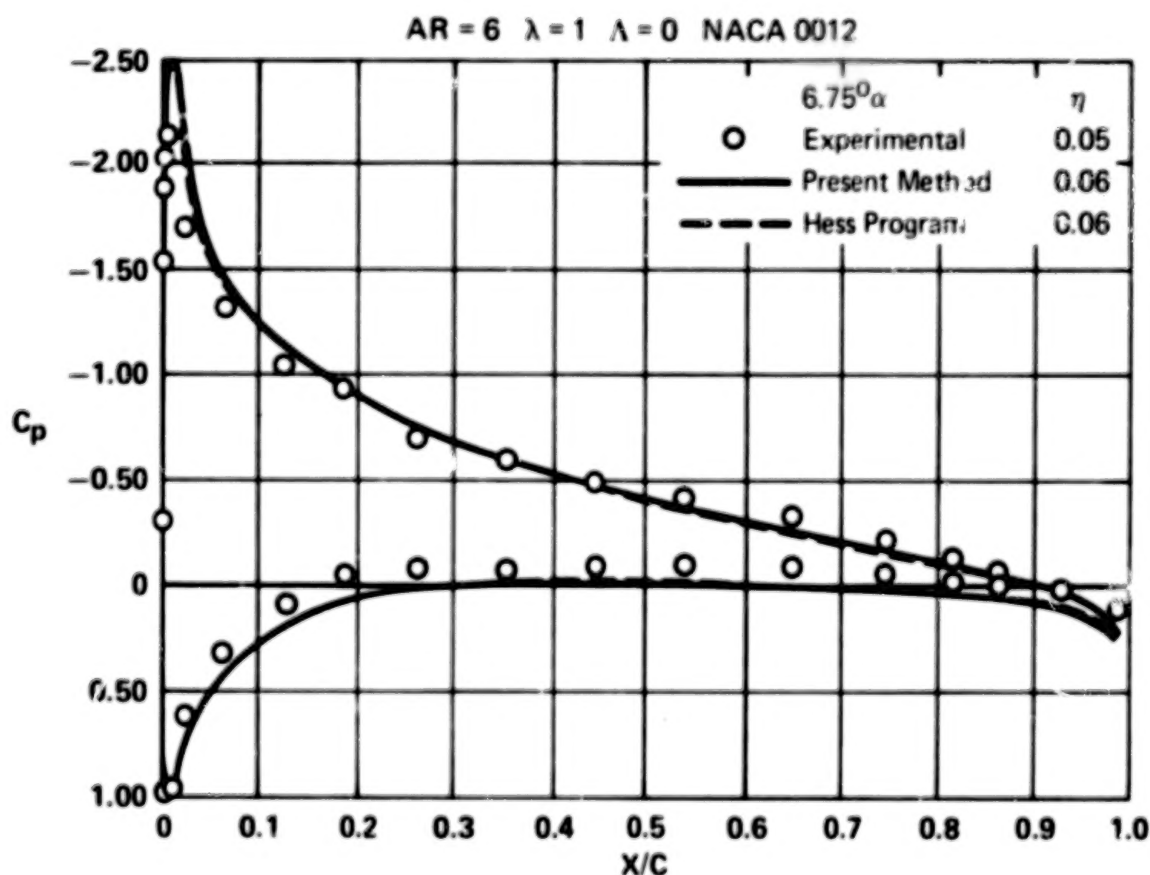
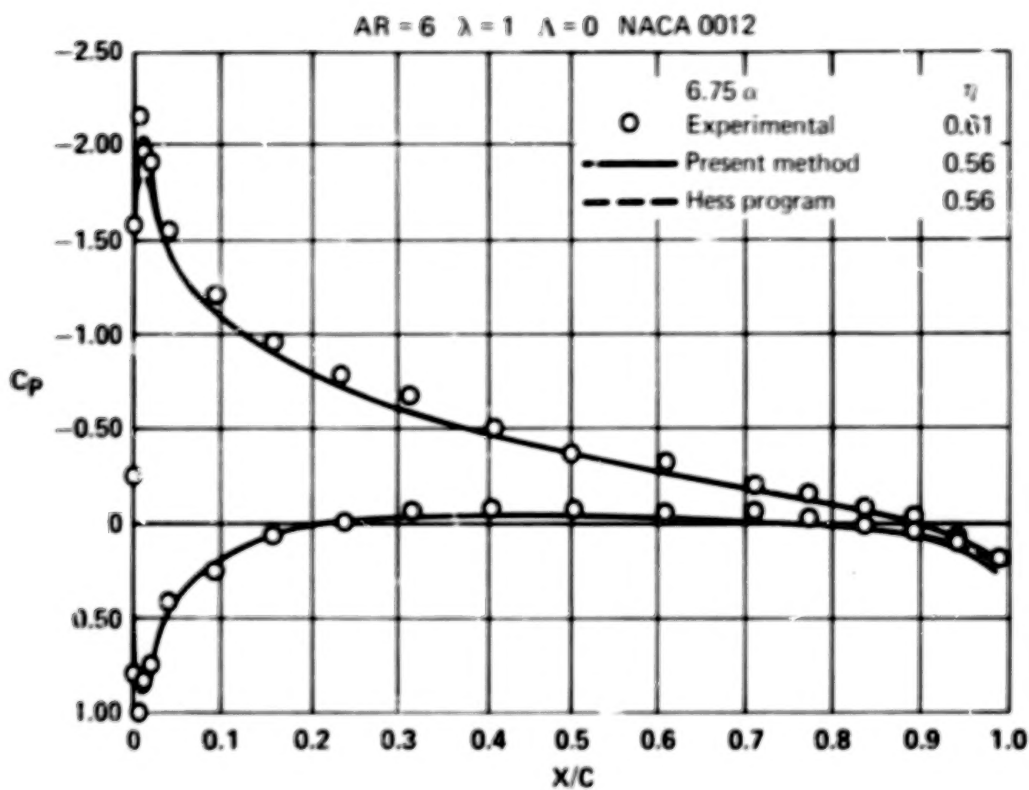
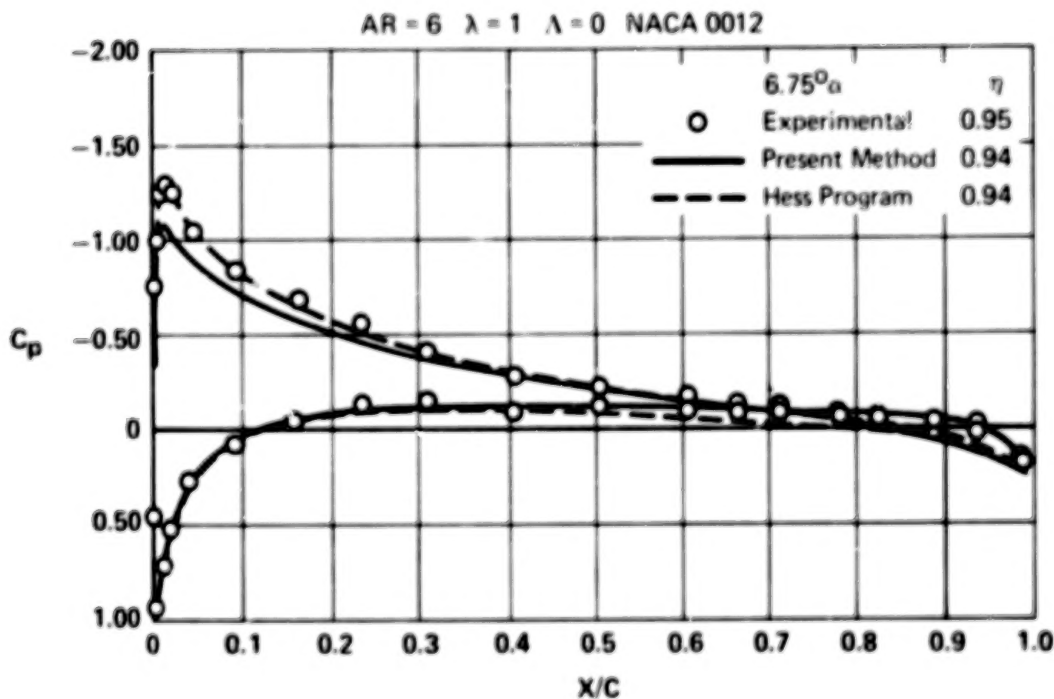


Figure 54. Rectangular Wing Pressure Distribution  
Root



**Figure 55. Rectangular Wing Pressure Distribution  
Midspan**



**Figure 56. Rectangular Wing Pressure Distribution  
Tip**

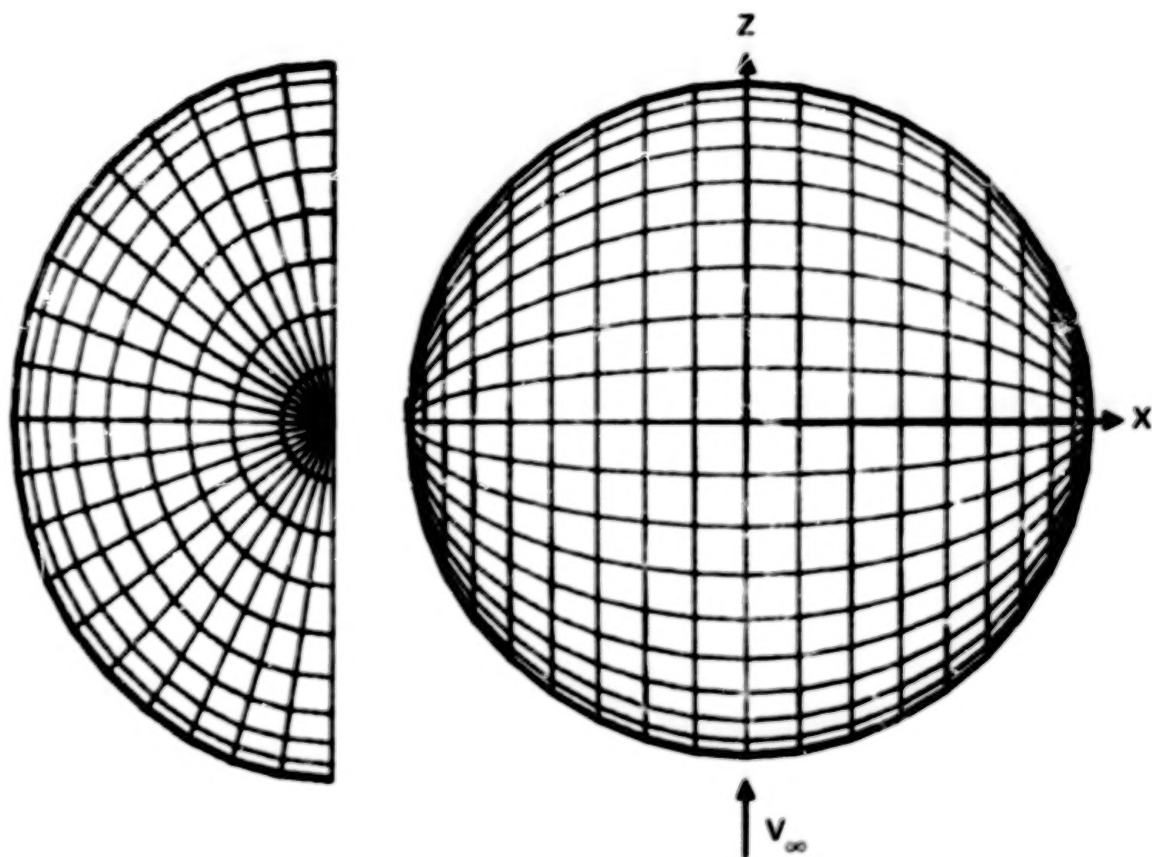


Figure 57. Sphere Paneling  
400 Panels per Semisphere

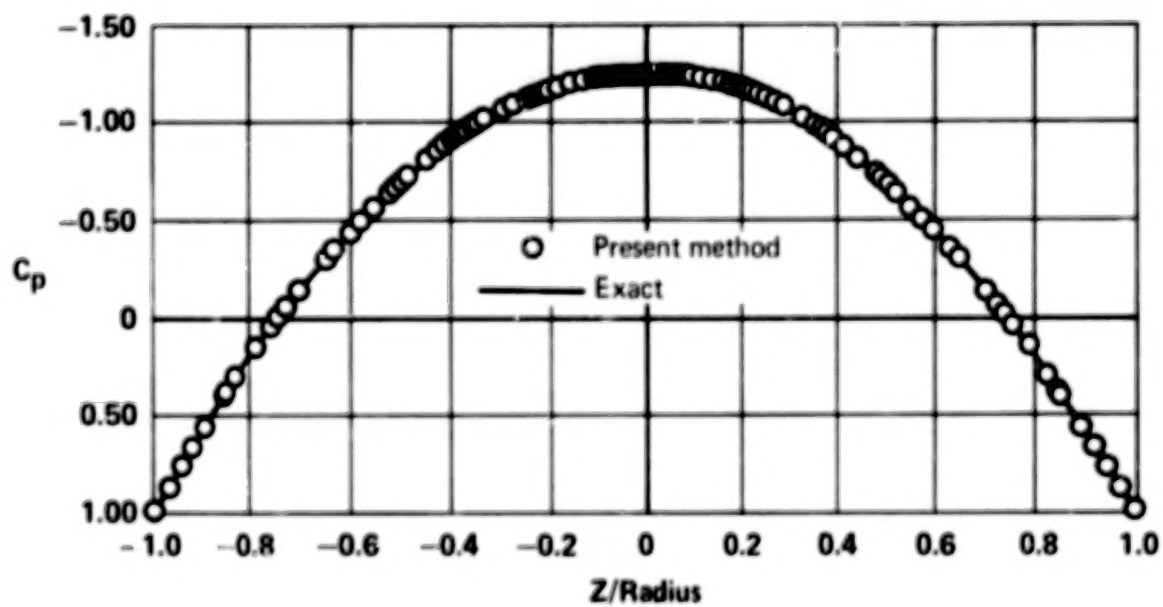


Figure 58. Pressure Distribution for a Sphere

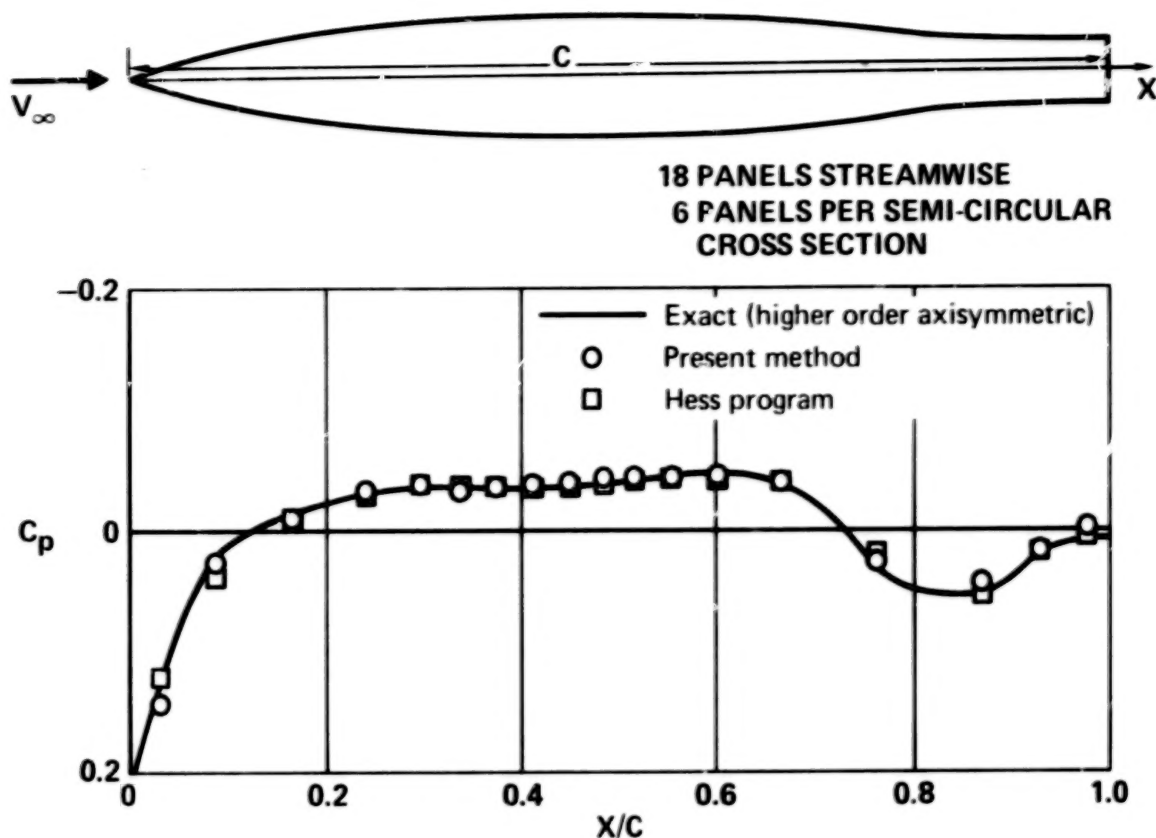


Figure 59. RML51F07 Body Alone

The capability to predict internal flow properties was assessed by testing the panelled duct of Figure 60. The geometry represents the body of revolution generated by wrapping a NACA 0010 airfoil around a circular cylinder where the cylinder length-to-radius ratio is ten. The minimum internal cross-sectional area is a factor of four smaller than the corresponding inlet and exit areas. The panel dimensions were chosen to be unusually large in comparison to the internal diameter in order to amplify numerical difficulties, thereby simplifying the assessment of the methods. A cylindrical wake extending approximately ten duct lengths downstream was panelled to allow Kutta condition satisfaction at the exit.

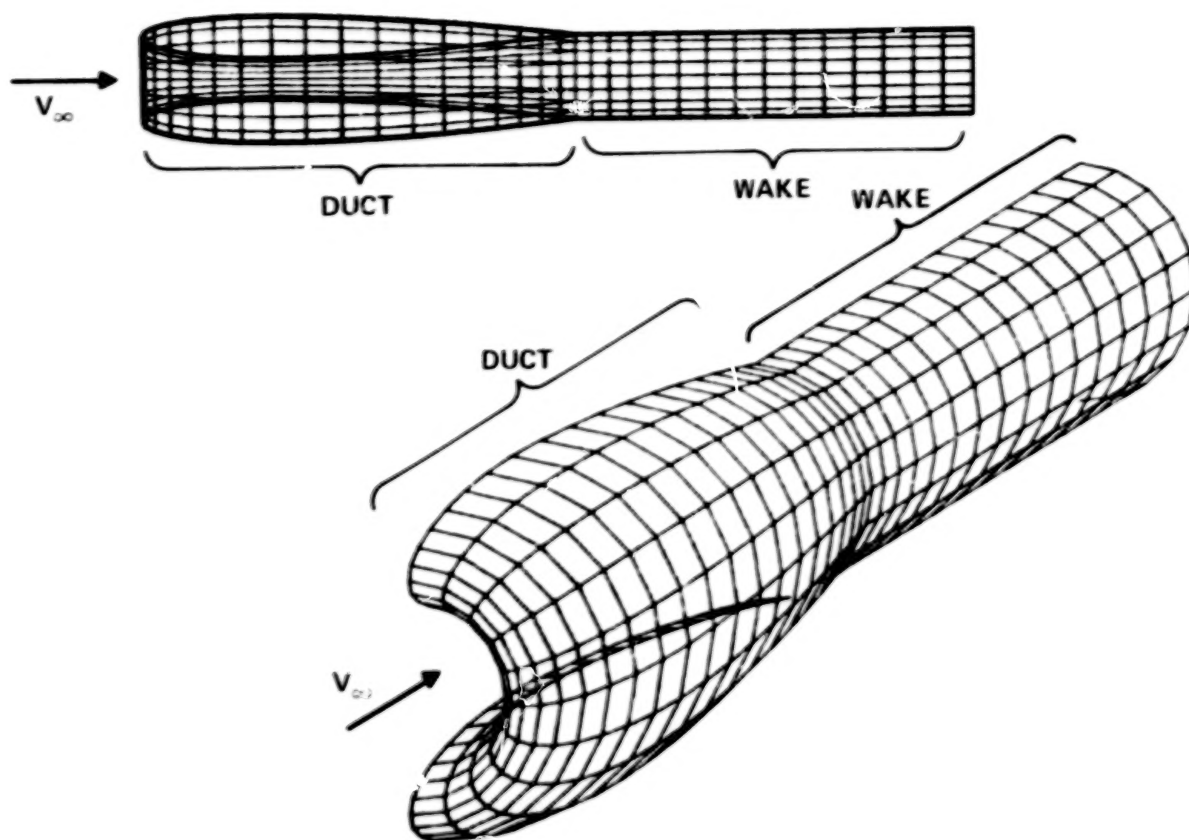
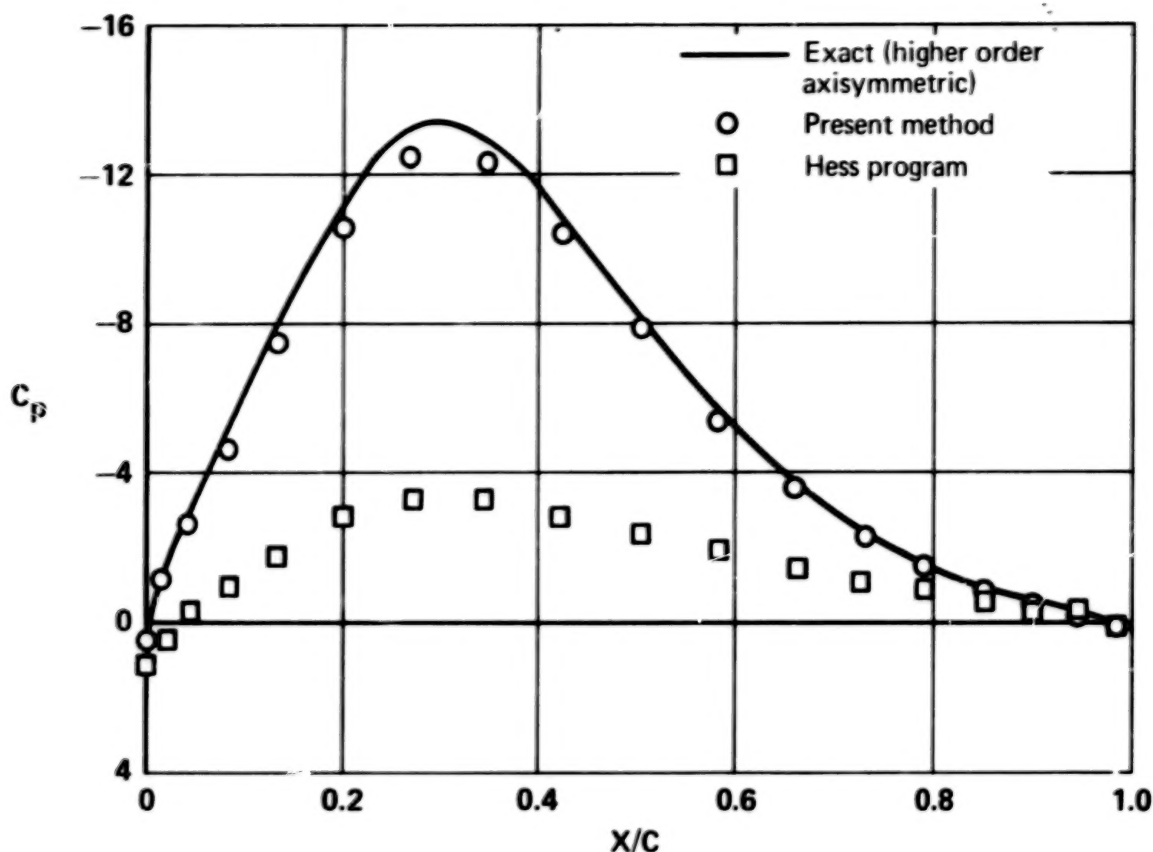


Figure 60. Duct Paneling  
Two Views

The internal pressure distribution is shown in Figure 61 for the present and Hess programs. To verify that the solution from the Hess higher order axisymmetric program is sufficiently close to exact to be so designated, both the axial panel distribution of Figure 60 and a distribution of double density were tested. The present method calculations agree quite well with the exact solution. It is noteworthy that the minimum pressure coefficient is  $C_p \approx -13$ , which compares to the value  $C_p = -15$  corresponding to one-dimensional flow theory applied to a constriction ratio of four. The Hess program vastly underpredicts the magnitude of the internal pressures. This is characteristic of low order source methods, which exhibit significant leakage between control points for internal flow.





**Figure 61. Duct Internal Pressure Distribution**  
Exit Kutta Condition Applied

Because it is conceivable that inaccuracies associated with exit Kutta condition satisfaction could have affected the duct solution of Figure 61, the example was repeated with no wake panelling and no Kutta condition (Figure 62). Although the resulting magnitude of internal flow velocity is significantly reduced, the relative prediction accuracy of the different methods is not substantially changed.

Hess has demonstrated that the inclusion of higher order terms significantly improves source method internal flow prediction accuracy (Reference 26). Of course, increasing panel density also increases the accuracy. For the Hess program, doubling the number of panels per unit length (quadrupling the total number) reduces the leakage by an approximate factor of two. It is interesting that even without higher order corrections, the present method provides satisfactory internal flow solutions for low panel density.

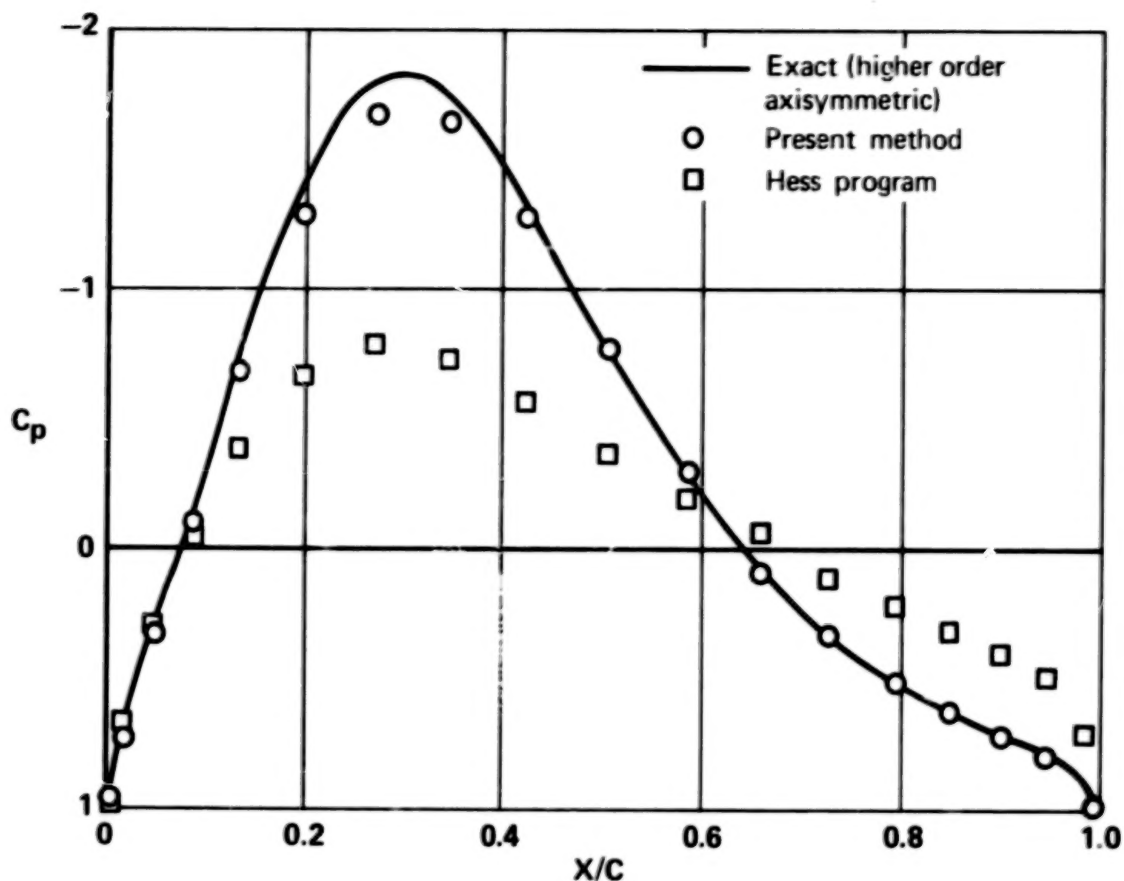


Figure 62. Duct Internal Pressure Distribution  
Zero Circulation

The objective of the final example is to determine whether the interference effect of a wing on a fuselage pressure distribution can be predicted without extending the wing panelling through the fuselage interior. Whereas the Hess program uses internal fuselage panelling, the present method relies entirely on surface panels to generate the fuselage lift. A disadvantage of the internal panelling approach is that it is not clear how various high or low wing configurations should be modelled.

Figure 63 illustrates the wing-body geometry selected for this example. The conventional mid-wing configuration is characteristic of geometries for which the Hess program predictions are very accurate, thereby providing a standard of comparison for the present method. Furthermore, experimental pressure data are available (Reference 27), which provide a second standard.



**Wing Details**

Airfoil Section

NACA 65A006

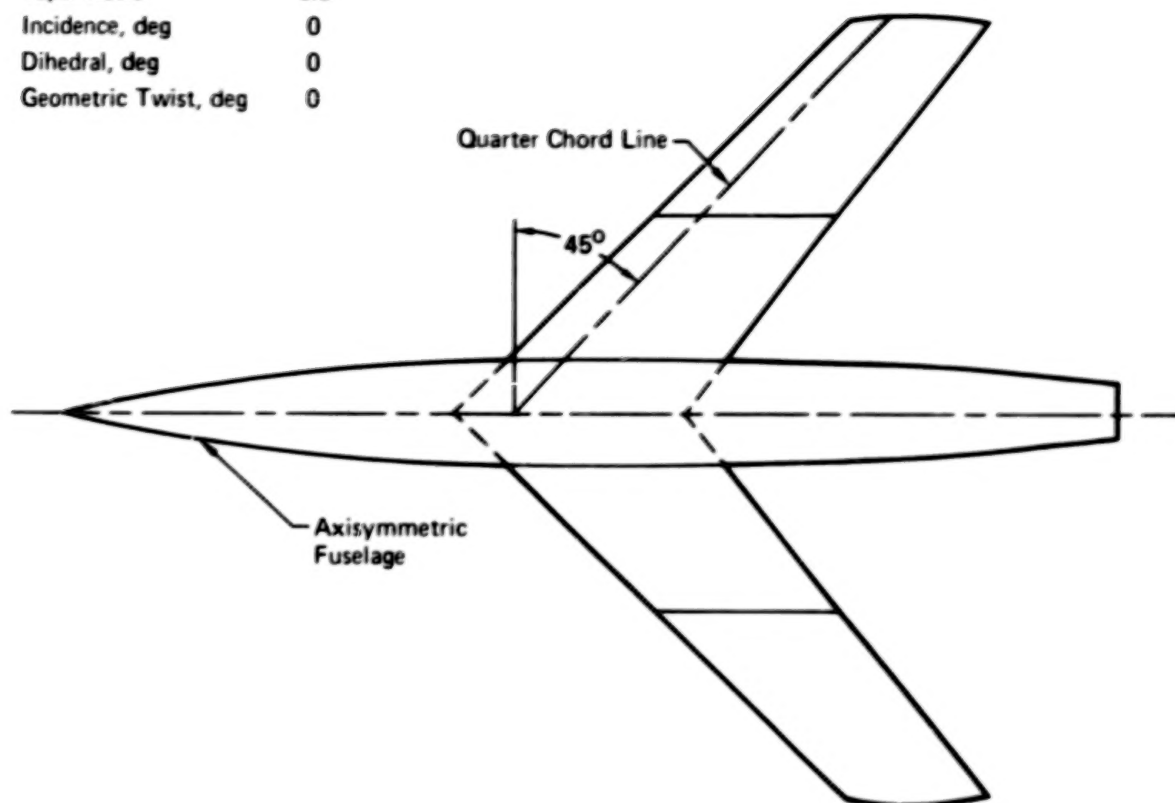
Aspect Ratio 4

Taper Ratio 0.6

Incidence, deg 0

Dihedral, deg 0

Geometric Twist, deg 0

**Figure 63. Wing-Body Geometry**

The geometry is symmetric with respect to both the wing chord plane and the zero butt line plane. Panelling was established on only one side of the latter plane of symmetry, and an appropriate symmetry option was used in program computations. Outboard of the fuselage, the wing was modelled by nine streamwise strips of approximately uniform width. Each strip contained twenty upper and twenty lower surface panels. The fuselage cross section panelling was equally spaced, with each panel subtending an arc of  $30^\circ$ . Nineteen fuselage station locations were used to define the fuselage panelling. For the present method only, the fuselage panel density in the region of

the wing intersection was increased and the panel distributions modified such that the wing and fuselage panel edges aligned. Whether this precaution is beneficial was not determined prior to the publication of this report.

In order to compensate for a deficiency in the present program, it was necessary to model the fuselage afterbody as a cylinder. For consistency, the modelling was also used in the Hess program. The deficiency is that if the centroids of a streamwise strip of wake panels are not colinear, the trailing vortex filaments will not be streamwise. In most cases it is possible to panel the wake by parallelograms, which eliminates the difficulty. Nonetheless, the deficiency in the present program should be eliminated.

The flow around the wing-body was calculated at  $4^\circ$  angle of attack. Neither compressibility nor viscous corrections were made to the calculated pressures. The test data corresponds to free stream Mach number 0.60.

The calculated and experimental fuselage pressure distributions are presented in Figure 64. In spite of significantly different approaches used to generate fuselage lift carryover, the predictions by the two programs are in close agreement. In fact, the total configuration lift coefficients agree to three significant figures ( $0.256 C_L$  at  $4^\circ \alpha$ ). For the Hess program, the slightly milder gradients at the wing root leading edge are probably due to the less dense fuselage panelling. The fact that the present method pressure distribution is of slightly lower magnitude immediately above and below the wing root is believed to be attributable to excursions from the nominal azimuthal angles  $\theta$  of Figure 64 ( $\theta \approx 45^\circ, 75^\circ, 105^\circ, 135^\circ$ ). For the present method, the panelling at the wing-fuselage intersection is such that the actual values of  $\theta$  are approximately  $70^\circ$  and  $110^\circ$  instead of the nominal values  $75^\circ$  and  $105^\circ$ , respectively. Both the present and Hess methods agree reasonably well with the experimental data, in spite of the fact that neither viscous nor compressibility corrections were applied.

By running the Hess program with and without the fuselage afterbody curvature, it was established that more than half of the difference between calculated and experimental pressures is attributable to modelling the afterbody as a cylinder.

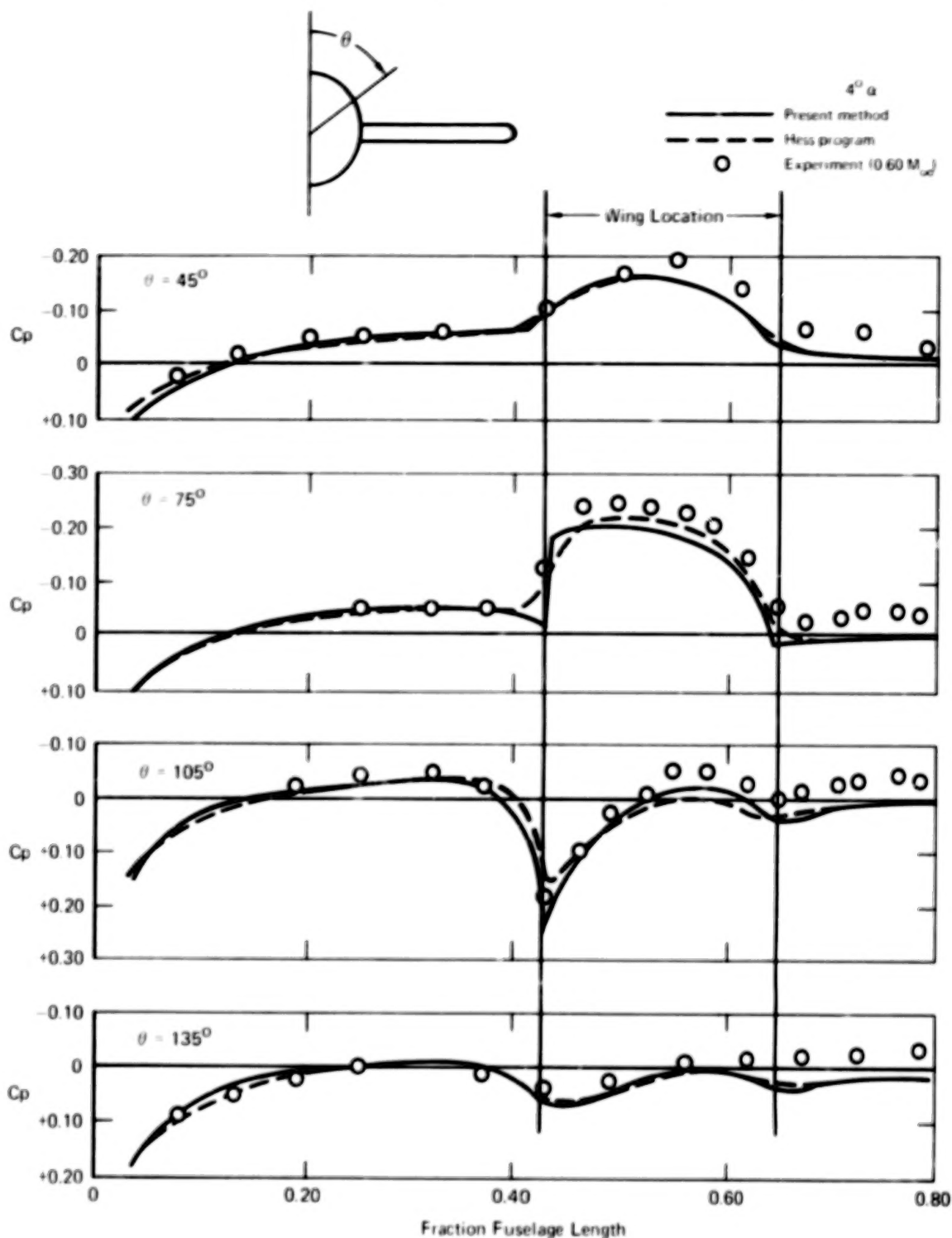


Figure 64. Fuselage Pressure Distribution in Presence of Wing

The wing section pressure distributions at three spanwise stations are presented in Figure 65-67. The two methods agree well with one another, except near the wing tip. As discussed earlier, a more sophisticated doublet surface fitting procedure is needed to improve the reliability of the present method at wing tips. Over the remainder of the wing, the greater part of the differences between calculated and experimental pressures is attributable to neglecting the fuselage afterbody curvature.

The wing-body example demonstrates that the panel edge boundary condition control points can provide the proper fuselage lift carryover without the extension of wing panelling through the fuselage.

Based on the above examples, some deficiencies of the present method which can and should be eliminated have been uncovered. The only one not discussed above pertains to the calculation of the influence coefficients. Only near field formulae are currently used. It is believed that this increases the time spent computing influence coefficients by an order of magnitude over what would be required if both far and intermediate formulae were used. As a result, the total computing time for a wing-body configuration is approximately five times greater than what would be required. This is reflected by comparing the computing times of the Hess and present programs. For example, on the CDC CYBER 175, the duct solution required 100 seconds computing time in the Hess program versus nearly 400 seconds for the present method. In each program, 360 body panels were used on each half of the symmetry plane. Clearly, far field formulae need to be introduced.

In general, the above examples confirm that the combined source-doublet distribution of Green's identity coupled with internal perturbation potential boundary conditions provides accurate and stable numerical flow field predictions for a wide variety of body shapes, including thin wings and duct interiors.

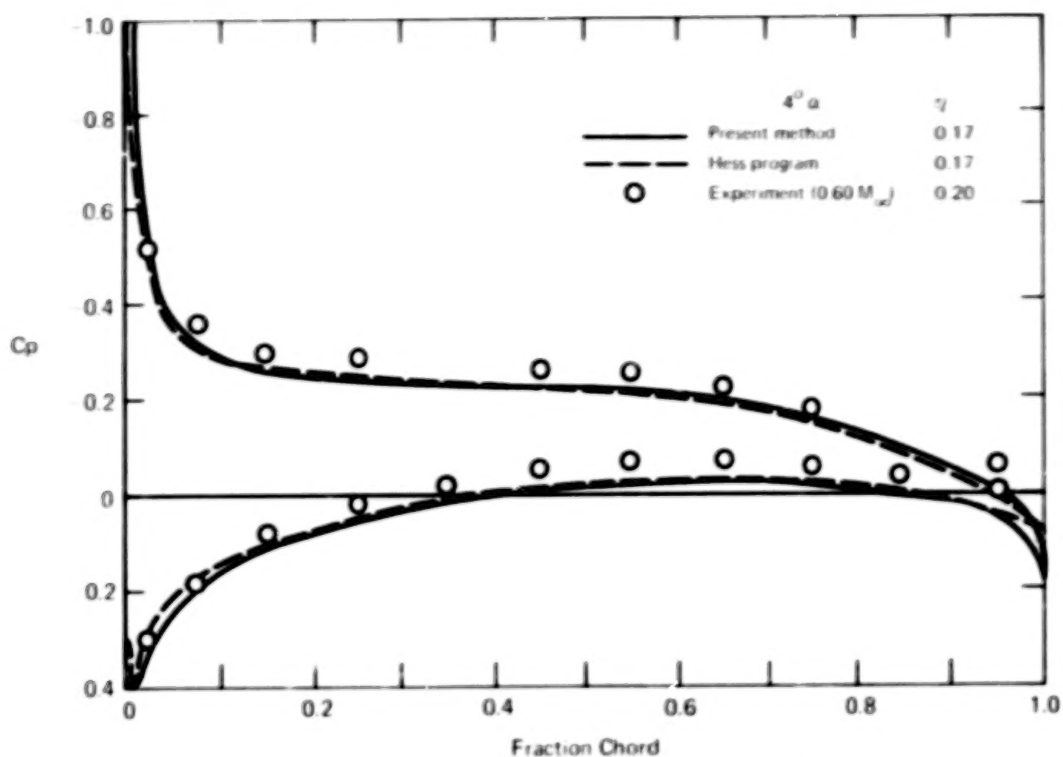


Figure 65. Wing-Body Chordwise Pressure Distribution - Exposed Root

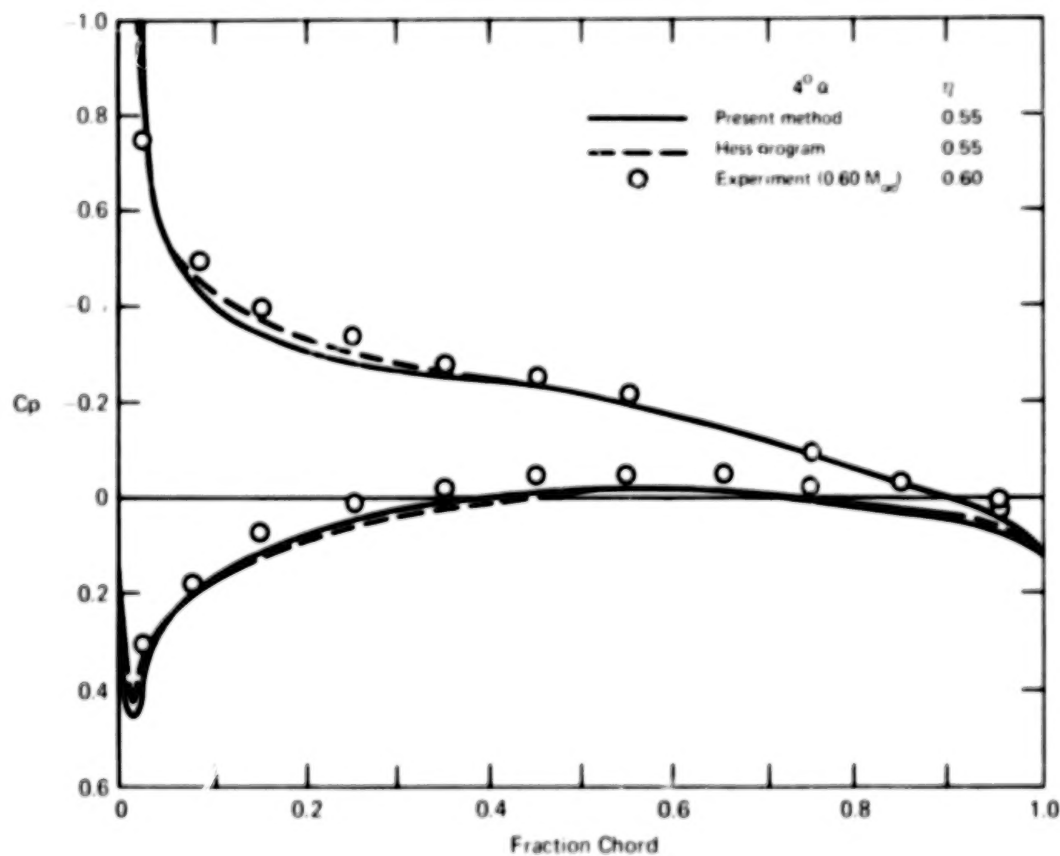


Figure 66. Wing-Body Chordwise Pressure Distribution - Midspan

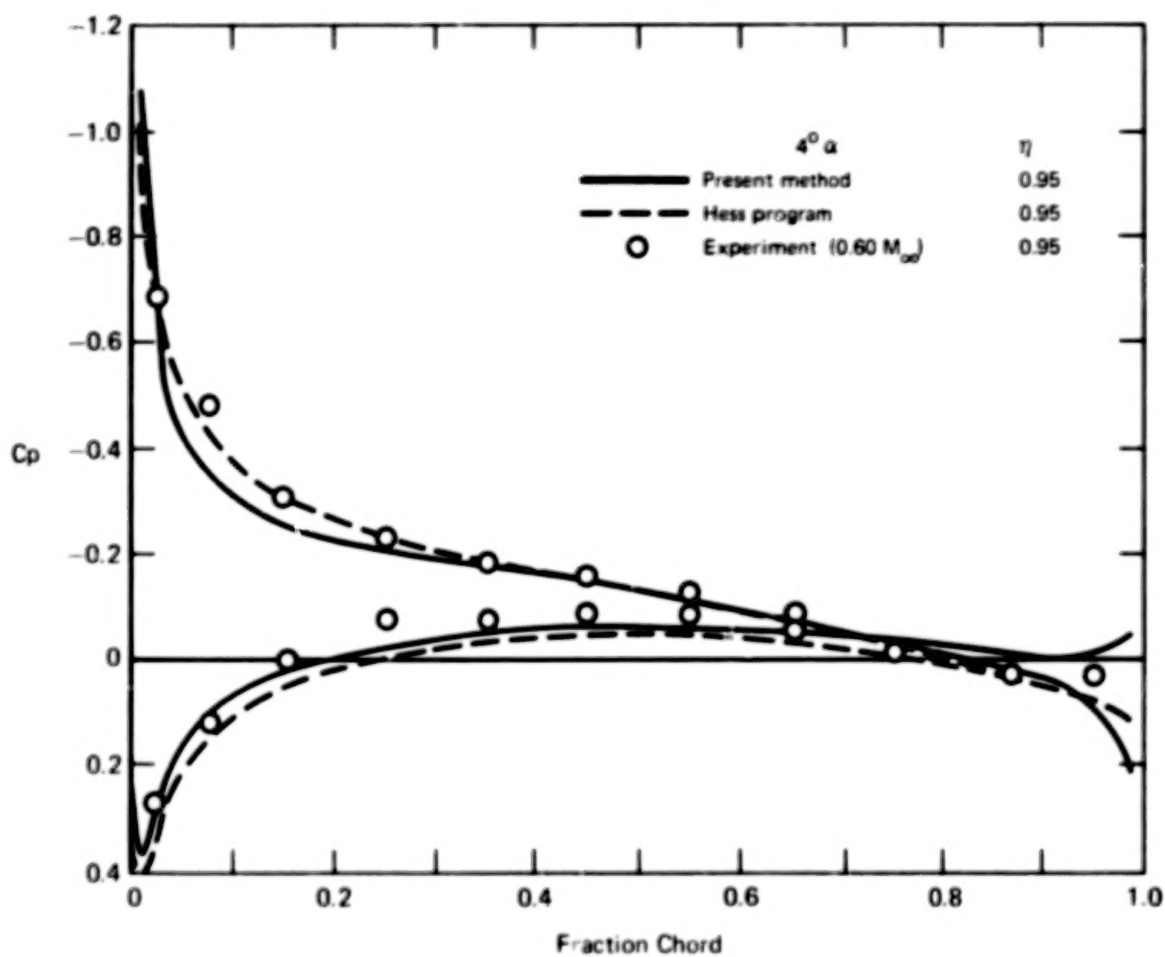


Figure 67. Wing-Body Chordwise Pressure Distribution - Tip

## CONCLUSIONS AND RECOMMENDATIONS

The use of mild combined source-doublet surface singularity distributions eliminates the numerical instabilities associated with the excessively strong singularity magnitude of source only solutions for highly loaded thin geometries. Also, significantly improved prediction accuracy is achieved at sharp concave corners. Even without higher order corrections, the use of internal potential boundary conditions produces surprisingly good accuracy for a wide variety of body geometries. The implementation of Green's identity offers several other benefits. Nonlifting configurations are made lifting by the simple introduction of a wake. The configuration doublet distribution automatically readjusts to generate lift, thereby eliminating the requirement for separate lifting and nonlifting formulations. Internal potential boundary conditions can be applied, which tend to improve numerical stability further and, as demonstrated in two dimensions, lead to a simplified reliable solution method for design problems in which the pressure distribution is prescribed. All boundary flow properties can be evaluated directly from the local singularity strengths, which saves the effort of summing the individual influences of the singularities on all panels. This feature also simplifies the implementation of mixed Neumann-Dirichlet boundary conditions.

Two areas of further study are recommended, specifically, the improvement of doublet continuity properties and the implementation of a design formulation for arbitrary bodies.

It is expected that doublet continuity properties can be improved significantly by using common values at adjacent panel edges prior to boundary condition satisfaction. At the expense of slightly greater computing time, this technique should both increase prediction accuracy and reduce the sensitivity to the panel distribution. Elimination of the trapezoidal panel restriction by implementing more comprehensive influence functions should also improve continuity characteristics.

For inverse design problems in which the geometry most nearly corresponding to a prescribed pressure distribution is to be determined, it is expected that the characteristics of

efficiency and stability demonstrated by the two-dimensional method will carry over in an application to three-dimensional geometries. The two-dimensional method exhibits unusual insensitivity to starting geometry and good convergence characteristics even in the difficult leading edge regions.

McDonnell Aircraft Company  
McDonnell Douglas Corporation  
St. Louis, Missouri 63166  
January 13, 1978



# REFERENCES

1. Lamb, Sir Horace: Hydrodynamics. Sixth Edition. Cambridge University Press, 1932.
2. Hess, J. L.: Calculation of Potential Flow About Arbitrary Three-Dimensional Lifting Bodies. MDC J5679-01, McDonnell Douglas, October 1972.
3. Kellogg, O. D.: Foundations of Potential Theory. Dover Publications, Inc., 1953.
4. Morino, Luigi; and Kuo, Ching-Chiang: Subsonic Potential Aerodynamics for Complex Configurations: A General Theory. AIAA J., Vol. 12, No. 2, February 1974, pp. 191-197.
5. Catherall, D.; Foster, D. N.; and Sells, C. C. L.: Two Dimensional Incompressible Flow Past a Lifting Aerofoil. R. A. E. TR-69118, 1969.
6. Williams, B. R.: An Exact Test Case for the Plane Potential Flow About Two Adjacent Lifting Aerofoils. Aeronautical Research Council R. & M. No. 3717, September 1971.
7. Hess, J. L.; and Smith, A. M. O.: Calculation of Potential Flow About Arbitrary Bodies. Progress in Aeronautical Sciences, Vol. 8. Pergamon Press, 1966.
8. Hess, J. L.: Higher-Order Numerical Solution of the Integral Equation for the Two-Dimensional Neumann Problem. Computer Methods in Applied Mechanics and Engineering, Vol. 2, No. 1, February 1973, pp. 1-15.
9. Martensen, E.: Berechnung der Druckverteilung an Gitterprofilen in ebener Potentialströmung mit einer Fredholmschen Integralgleichung (Calculation of Pressure Distribution on Cascade Sections in Planar Potential Flow by a Fredholm Integral Equation). Archive for Rational Mechanics and Analysis, Vol. 3, No. 3, 1959.
10. Oellers, H. J.: Die Inkompressible Potentialströmung in der Ebene Gitterstufe (The Incompressible Potential Flow in Planar Cascades). Jahrbuch 1962 der Wissenschaftlichen Gesellschaft für Luft-und Raumfahrt, pp. 349-353.
11. Dvorak, F. A.; and Woodward, F. A.: A Viscous/Potential Flow Interaction Analysis Method for Multi-Element Infinite Swept Wing. NASA CR-2476, November 1974.

# REFERENCES (Continued)

12. Stevens, W. A.; Goradia, S. H.; and Braden, J. A.: Mathematical Model for Two-Dimensional Multi-Component Airfoils in Viscous Flow. NASA CR-1643, July 1971.
13. Halsey, N. D.: Methods for the Design and Analysis of Jet-Flapped Airfoils. J. of Aircraft, Vol. 11, Sept. 1974 pp. 540-546.
14. Maskew, B.: A Subvortex Technique for the Close Approach to A Discretized Vortex Sheet. Vortex-Lattice Utilization Workshop. NASA SP-405, May 1976.
15. Tulinius, J. R.: Theoretical Prediction of Thick Wing and Pylon-Fuselage-Fanpod-Nacelle Aerodynamic Characteristics at Subcritical Speeds. NASA CR-137578, July 1974.
16. Johnson, F. T.; and Rubbert, P. E.: Advanced Panel-Type Influence Coefficient Methods Applied to Subsonic Flows. AIAA Paper 75-50, January 1975.
17. Bristow, D. R.: A New Surface Singularity Method for Multi-Element Airfoil Analysis and Design. AIAA Paper 76-20, January 1976.
18. Maskew, B.; and Woodward, F. A.: Symmetrical Singularity Model for Lifting Potential Flow Analysis. AIAA J. of Aircraft, Vol. 13, No. 9, September 1976, pp. 733-734.
19. Bristow, D. R.: Incompressible Potential Flow: Numerical Characteristics of Three Classical Surface Singularity Representations. MDC A4407, McDonnell Douglas, September 1976.
20. Bristow, D. R.: Recent Improvements in Surface Singularity Methods for the Flow Field Analysis about Two-Dimensional Airfoils. AIAA Paper 77-641, June 1977.
21. Bristow, D. R.: Improvements in Surface Singularity Analysis and Design Methods. NASA Advanced Technology Airfoil Research Conference, Langley Research Center, 7-9 March 1978.
22. Hess, J. L.: The Use of Higher-Order Surface Singularity Distributions to Obtain Improved Potential Flow Solutions for Two-Dimensional Lifting Airfoils. Computer Methods in Applied Mechanics and Engineering, Vol. 5, 1975, pp. 11-35.

#### REFERENCES (Concluded)

23. Hess, J. L.: Review of Integral-Equation Techniques for Solving Potential-Flow Problems with Emphasis on the Surface-Source Method. Computer Methods in Applied Mechanics and Engineering, Vol. 5, 1975, pp. 145-196.
24. Yip, L. P.; and Shubert, G. L.: Pressure Distributions on a 1- by 3-Meter Semispan Wing at Sweep Angles from  $0^\circ$  to  $40^\circ$  in Subsonic Flow. NASA TN D-8307, December 1976.
25. Hess, J. L.; and Martin Jr., R. P.: Improved Solution for Potential Flow about Arbitrary Axisymmetric Bodies by the Use of a Higher-Order Surface Source Method. NASA CR 134694, July 1974.
26. Hess, J. L.: Status of a Higher-Order Panel Method for Nonlifting Three-Dimensional Potential Flow. Report No. NADC-76118-30, 31 August 1977.
27. Loving, D. L.; and Estabrooks, B. B.: Transonic-Wing Investigation in the Langley 8-Foot High-Speed Tunnel at High Subsonic Mach Numbers and at a Mach Number of 1.2. NACA RM L51F07, 6 September 1951.

1. Report No. NASA CR-3020		2. Government Accession No.		3. Recipient's Catalog No.	
4. Title and Subtitle MODIFICATION OF THE DOUGLAS NEUMANN PROGRAM TO IMPROVE THE EFFICIENCY OF PREDICTING COMPONENT INTERFERENCE AND HIGH LIFT CHARACTERISTICS				5. Report Date August, 1978	
				6. Performing Organization Code	
7. Author(s) D. R. Bristow and G. G. Grose				8. Performing Organization Report No.	
				10. Work Unit No.	
9. Performing Organization Name and Address McDonnell Aircraft Company McDonnell Douglas Corporation St. Louis, Missouri 63166				11. Contract or Grant No. NAS1-14756	
				13. Type of Report and Period Covered Contractor Report	
12. Sponsoring Agency Name and Address National Aeronautics and Space Administration Washington, D.C. 20546				14. Sponsoring Agency Code	
15. Supplementary Notes  Langley Technical Monitor: Harry L. Morgan, Jr. Final Report					
16. Abstract  The Douglas Neumann method for low-speed potential flow on arbitrary three-dimensional lifting bodies was modified by substituting the combined source and doublet surface paneling based on Green's identity for the original source panels. Numerical studies show improved accuracy and stability for thin lifting surfaces, permitting reduced panel number for high-lift devices and supercritical airfoil sections. The accuracy of flow in concave corners is improved. A method of airfoil section design for a given pressure distribution, based on Green's identity, was demonstrated. The program uses panels on the body surface with constant source strength and parabolic distribution of doublet strength, and a doublet sheet on the wake. The program is written for the CDC CYBER 175 computer. Results of calculations are presented for isolated bodies, wings, wing-body combinations, and internal flow.					
17. Key Words (Suggested by Author(s)) Low speed flow Potential flow Wing-body configurations Lifting bodies Green's identity Surface paneling method				18. Distribution Statement  Unclassified - Unlimited	
				Subject Category 02	
19. Security Classif (of this report) Unclassified		20. Security Classif (of this page) Unclassified		21. No. of Pages 124	
				22. Price \$6.50	

\* For sale by the National Technical Information Service, Springfield, Virginia 22161

NASA-Langley, 1978

115

90

50

**END**

**DEC 4 1978**